UNIVERSITA' DEGLI STUDI DI NAPOLI "FEDERICO II"

SCUOLA POLITECNICA DELLE SCIENZE DI BASE

Dipartimento Di Ingegneria Chimica, Dei Materiali e Della Produzione Industriale

Ph.D. course in

Industrial Product and Process Engineering

Ph.D. thesis

Biopolymer nanostructures for precision imaging: basic principles and applications to nanomedicine

Coordinator:

Prof. Andrea D'Anna

Candidate:

Alessio Smeraldo

Supervisors:

Prof. Paolo Antonio Netti

Prof. Enza Torino

TABLE OF CONTENT

INTRODUCTION: BACKGROUND AND AIM OF THE WORK

Nowadays, an accurate and reliable diagnosis allows to choose the most appropriate therapy for the patient, in order to address him to the right therapeutic and helpful way. Different imaging modalities can be used by the clinician to get useful anatomical and functional information depending on the investigated body district: Computed Tomography (CT), Ultrasound (US), Magnetic Resonance Imaging (MRI), Positron Emission Tomography (PET), etc [1].

Among the above-mentioned diagnostic techniques, MRI is a regularly applied diagnostic imaging modality since it provides three-dimensional information with high spatial resolution, in particular of soft tissues, through the use of not invasive magnetic fields and gradients [2-4]. In fact, the signal generated by hydrogen protons, that are abundantly present in the human body, particularly in water and fat, allows to get different contrast in tissues based on their longitudinal (T_1) and transverse (T_2) characteristic relaxation times [5]. However, to enhance further the signal intensity and improve the contrast between distinct tissues, substances called contrast agents (CAs) are intravenously injected before MRI scans. The extensive use of contrast agents is based on their property to induce additional contrast to MRI image making visible anatomical details otherwise not appreciable. At molecular level, this enhancement is explained by the presence of unpaired electrons nearby water molecule that, having a magnetic moment many times higher than hydrogen proton, shorten the relaxation times [6,7]. Gadolinium-based contrast agents (Gd-CAs) are the most widespread used in the clinical practice due to their ability to positively influence relaxation leading to brighter images. In particular, to indicate the potency of a CA to enhance image contrast, the concept of relaxivity is introduced [7]. The relaxivity (longitudinal r_1 ; transverse r_2) is defined as the change in the relaxation rate (ΔT) per unit of CA concentration ($[M]$]) after its introduction in the body. Water molecules into proximity of the CA are involved in specific chemical interactions, which play an important role in the transmission of the relaxation effect to the bulk water. In particular, the physical properties of paramagnetic CAs in the inner sphere, where water-CAs interaction is stronger, have been well described by the Solomon-Bloembergen-Morgan (SBM) equation that is used to foresee the relaxation rate [8,9]. To achieve a higher relaxivity some characteristic parameters can be finely handled: the rotational correlation time of the metal ion – water proton vector τ_R, the longitudinal and transverse electron spin relaxation times of the metal ion T_{1e} and T_{2e} , and the lifetime of water molecules in the inner sphere τ_m.

Despite Gd-CAs extensive use, only in the last few years, FDA has highlighted many risks related to their use such as nephrotoxicity, heavy allergic effects and, recently, about the deposition within the brain [5,10-18]. These alerts opened a debate about the opportunity to formulate Gd-CAs in a different way but also to the use of alternative and safer compounds to be administered such as Manganese (Mn). It represents, potentially, an alternative to Gd, able to overcome some of the previously described drawbacks [19-22]. In fact, manganese is an element already present in the human body, involved in many cellular processes and so the presence of an endogenous elimination pathway might be a great advantage. As in the case of Gd, some side effects are present for Mn too. An overexposure to free Mn ions could lead to neurodegenerative disorder known as "manganism" due to the similarity between Mn and Ca and Mg [21,23]. Transport mechanisms for calcium can be used by Mn ions to enter the nervous system influencing the normal synaptic transmission, in particular in the brain.

Although MRI has the advantage to avoid the use of ionizing radiations, CT still remains the widest used imaging technique for its ability to provide anatomic details of hard tissues with high resolution at low cost [24,25]. CT is based on the interaction of X-rays with the body and in particular on the attenuation phenomena that take place along their travel as a result of absorption and/or scattering effects. The ability of matter to attenuate X-rays is measured in Hounsfield units (HU). In order to distinguish tissues with similar HU numbers, contrast agents are used to highlight the region of interest increasing the X-rays attenuation in that area. Taking in consideration that the attenuation is proportional to the third power of the atomic number of the material, the choice is limited to elements with high atomic number. For this reason, iodine represents a good compromise between high atomic number (Z=53), biocompatibility and cost compared to metals [24,25]. In fact, iodine is used by thyroid glands to produce hormones, triiodothyronine (T_3) and thyroxine (T_4), involved in metabolic, cardiovascular and developmental processes [26,27]. Since a high iodine concentration is needed for successful imaging, more precisely in the millimolar range, a high ratio of iodine atoms per molecule is needed. A common strategy is the chemical modification of organic molecules that leads to different physical properties and influence the ionicity, osmolality and viscosity of the CA.

However, even in this case, several side effects have been reported. In fact, among different adverse reactions following iodinated CAs administration such as allergic or cutaneous ones, kidney failure remains the main side effect that can lead to severe consequences [28-32]. Another organ that can be affected by the injection of the iodinated CAs is the thyroid where iodine accumulates to produce

hormones. The overexposure to CA could lead to hyperthyroidism or hypothyroidism due to the effect of free iodine, released as a result of a photolytic degradation in some cases, in a quantity that is hundred times higher than the needed daily intake [33,34].

Therefore, the use of contrast agents in the medical imaging is strongly limited by their side effects. In fact, although different ligands are used to improve their performances and *in vivo* stability, CAs can undergo *in vivo* dissociation and deposition in vital organs such as brain, thyroid, and kidneys. Moreover, CAs suffer from additional limitations such as absence of specificity toward the target site and a rapid clearance from the bloodstream that allows short image acquisition times. This results in an image contrast that is not homogenously localized in the region of interest leading to a signal that is much lower than the theoretical one. For this reason, a particular attention has been recently drawn to molecular imaging, interpreted as the characterization of biological and physiological processes at the cellular and/or molecular level [1,35-38]. In addition to the possibility to drastically reduce the CA dose, this methodology allows a dynamic and noninvasive monitoring of various diseases, before their clear macroscopic manifestation, leading to an early diagnosis. Moreover, this higher selectivity allows the combined use of more CAs heading toward the increasing use of multimodal imaging modalities such as PET/MRI and PET/CT that are able to provide anatomical details and functional information simultaneously. To achieve this goal, a contrast agent with high sensitivity and specificity to target a specific tissue or cell type is required for successful imaging.

Among all the possible probes, polymer nanoparticles (NPs) have recently proven to be a useful tool in the biomedicine field for several applications. Thanks to their unique properties, these nanosystems are suitable for drug delivery, cancer therapy, diagnostics, sensing, optoelectronics, tissue engineering and molecular biology. For this reason, they can represent an optimal tool to overcome CAs drawbacks thanks to their small size and functionalizable surface as well as their biocompatibility [39-44]. In fact, a sufficiently high size prevents glomerular filtration and/or their diffusion through the vascular endothelium while surface modifications allow to delay the recognition and the subsequent opsonization leading to long-circulation properties and increase the specificity of the CAs towards the target site. Another advantage is the ability of nanovectors to entrap CAs reducing their *in vivo* interactions and consequently both related side effects and possible dechelation. Therefore, the encapsulation of CAs in polymer nanostructures, even more than one simultaneously, without the need of chemical modifications, allows to face the above-mentioned limitations. Consequently, the design of the nanovector, through a suitable choice of polymers, is

essential to define the physicochemical properties of the nanostructured CA. Moreover, the interaction of the contrast agents with the surrounding polymer matrix, whether in nanostructured form or not, has to be taken in consideration. In fact, the presence of the nanovector could influence the performance of the CAs acting on the fundamental parameters behind the generation of the imaging signal [5]. For example, recent works have proved that the characteristic correlation times, as described by the SBM theory, can be strongly modified when a Gd-CAs is encapsulated inside a polymer matrix [5,7,45-57]. In particular, hydrogel matrices made up of hydrophilic polymers are able to accumulate a large amount of water within their network, increasing interactions between water molecules and gadolinium and, consequently, promoting a relaxivity boosting. The effect has been very well described by Russo et al. that synthesized crosslinked Hyaluronic Acid NPs (cHANPs) loaded with Gd-DTPA through a microfluidic flow focusing process, demonstrating the possibility to improve relaxivity through the tunability of crosslink density, mesh size, hydrophilicity and loading capability by handling the process parameters [51,54]. Indeed, the proper control of the structural properties of polymer-based nanohydrogels affects the water molecules' dynamics resulting, at specific conditions, in a relaxivity boost. This effect, named *Hydrodenticity*, arises when a complex equilibrium between elastodymanic forces of the polymer chains, water osmotic pressure and hydration degree of Gd-CAs is reached acting, consequently, on SBM correlation times [51,55,57]. In particular, the improved relaxation rate is the result of an increased residence lifetime of water molecules within the crosslinked polymer matrix, a restricted molecular tumbling and a resulting faster exchange rate with gadolinium. Therefore, an in-depth study of the interactions between CAs and polymer matrix could lead to get improved performances of clinically used imaging agents by simply acting on the physicochemical properties of the nanovectors.

To fine tune nanoparticles features and consequently their imaging ability, conventional batch process does not represent the best way forward due to the uncontrollable mixing and intrinsic variability that affect not only nanoparticles size but also their morphology. Microfluidics, instead, has proved to be suitable to control finely and efficiently the mixing thanks to the accurate control of process parameters [54,58,59]. In fact, the manipulation of small amounts of fluid reagent, combined with the laminar flow conditions ($Re < 10$) within microfluidic channels, ensures a mixing that is only due to diffusion of molecules across the interface of the two flowing in parallel fluids. Consequently, microfluidic processes show many advantages in terms of control of nanoparticles properties such as size and polydispersity. In our recent work recently published on Biomedicines *"Tuning of hydrogel architectures by ionotropic gelation in Microfluidics: beyond batch processing to*

multimodal diagnostics", we demonstrate the ability of microfluidics to tune the morphology of CS-HA NPs by controlling the flow rates[60]. Moreover, preliminary results on the co-encapsulation of a dye for Optical Imaging and a Gd-CAs for MRI demonstrate the dual capability of enhancing relaxometric properties of gadolinium as explained by the *Hydrodenticity* concept and of serving as a promising nanovector for multimodal imaging applications.

Despite the advantage of process parameters control offered by microfluidics, it is often difficult to achieve a nanoformulation with the desired morphological, structural, and functional characteristics due to the complex fluid- and thermo-dynamic phenomena involved in the mixing. In recent years, artificial neural networks (ANNs) have emerged as a powerful tool to model and analyse complex multivariate processes. The architecture of ANN is based on the linkage structure of biological neurons to simulate the way in which the human brain processes information [61]. The network is made up of different layers in which each neuron generates an output based on the weightings of each input. The last layer gives back the predicted results. In particular, in the supervised learning approach, the ANN is built and optimized through a trial-and-error approach starting from experimental data in order to find the more accurate input-output relationship. Therefore, thanks to the ANN, it is possible to estimate the properties of the final nanovector by simply giving in input a set of process parameters values in order to understand which of them mostly influence the outcome [62-66]. In this way, it is possible to directly tune the right variable to obtain the more suitable morphological, structural, and functional properties of the nanovector avoiding waste of materials and time expensive experimental campaign.

In conclusion, the goal of this work is to get a clear understanding of the interaction mechanisms between polymer and clinically used contrast agents in order to improve the performances of these latter by tuning the physicochemical properties of the surrounding nanovector. In particular, taking advantage of the tunability of the microfluidic production process and the use of machine learning methods, we aim to finely handle the imaging properties of the nanovectors increasing their specificity and sensitivity towards the molecular target.

References

1. James, M.L.; Gambhir, S.S. A Molecular Imaging Primer: Modalities, Imaging Agents, and Applications. *Physiol. Rev.* **2012**, *92*, 897-965.
2. McGowan, J.C. Basic Principles of Magnetic Resonance Imaging. *Neuroimaging Clin. N. Am.* **2008**, *18*, 623-636.

3. van Geuns, R.J.; Wielopolski, P.A.; de Bruin, H.G.; Rensing, B.J.; van Ooijen, P.M.; Hulshoff, M.; Oudkerk, M.; de Feyter, P.J. Basic principles of magnetic resonance imaging. *Prog. Cardiovasc. Dis.* **1999**, *42*, 149-156.
4. Plewes, D.B.; Kucharczyk, W. Physics of MRI: A primer. *J. Magn. Reson. Imaging* **2012**, *35*, 1038-1054.
5. Smeraldo, A.; Netti, P.A.; Torino, E. New Strategies in the Design of Paramagnetic CAs. *Contrast Media Mol. Imaging* **2020**, *2020*, 4327479.
6. Caravan, P.; Ellison, J.J.; McMurry, T.J.; Lauffer, R.B. Gadolinium(III) Chelates as MRI Contrast Agents: Structure, Dynamics, and Applications. *Chem. Rev.* **1999**, *99*, 2293-2352.
7. Caravan, P. Strategies for increasing the sensitivity of gadolinium based MRI contrast agents. *Chem. Soc. Rev.* **2006**, *35*, 512-523.
8. Solomon, I. Relaxation Processes in a System of Two Spins. *Phys. Rev.* **1955**, *99*, 559-565.
9. Lauffer, R.B. Paramagnetic Metal Complexes as Water Proton Relaxation Agents for NMR Imaging: Theory and Design. *Chem. Rev.* **1987**, *87*, 901-927.
10. Thakral, C.; Alhariri, J.; Abraham, J.L. Long-term retention of gadolinium in tissues from nephrogenic systemic fibrosis patient after multiple gadolinium-enhanced MRI scans: case report and implications. *Contrast Media Mol. Imaging* **2007**, *2*, 199-205.
11. Barbieri, S.; Schroeder, C.; Froehlich, J.M.; Pasch, A.; Thoeny, H.C. High signal intensity in dentate nucleus and globus pallidus on unenhanced T1-weighted MR images in three patients with impaired renal function and vascular calcification. *Contrast Media Mol. Imaging* **2016**, *11*, 245-250.
12. Moser, F.G.; Watterson, C.T.; Weiss, S.; Austin, M.; Mirocha, J.; Prasad, R.; Wang, J. High Signal Intensity in the Dentate Nucleus and Globus Pallidus on Unenhanced T1-Weighted MR Images: Comparison between Gadobutrol and Linear Gadolinium-Based Contrast Agents. *AJNR Am. J. Neuroradiol.* **2018**, *39*, 421-426.
13. Kanda, T.; Ishii, K.; Kawaguchi, H.; Kitajima, K.; Takenaka, D. High Signal Intensity in the Dentate Nucleus and Globus Pallidus on Unenhanced T1-weighted MR Images: Relationship with Increasing Cumulative Dose of a Gadolinium-based Contrast Material. *Radiology* **2013**, *270*, 834-841.
14. Radbruch, A.; Weberling, L.D.; Kieslich, P.J.; Hepp, J.; Kickingereder, P.; Wick, W.; Schlemmer, H.P.; Bendszus, M. High-Signal Intensity in the Dentate Nucleus and Globus Pallidus on Unenhanced T1-Weighted Images: Evaluation of the Macrocyclic Gadolinium-Based Contrast Agent Gadobutrol. *Invest Radiol .* **2015**, *50*, 805-810.
15. McDonald, R.J.; McDonald, J.S.; Kallmes, D.F.; Jentoft, M.E.; Murray, D.L.; Thielen, K.R.; Williamson, E.E.; Eckel, L.J. Intracranial Gadolinium Deposition after Contrast-enhanced MR Imaging. *Radiology* **2015**, *275*, 772-782.
16. Ramalho, J.; Semelka, R.C.; Ramalho, M.; Nunes, R.H.; AlObaidy, M.; Castillo, M. Gadolinium-Based Contrast Agent Accumulation and Toxicity: An Update. *AJNR Am. J. Neuroradiol.* **2016**, *37*, 1192-1198.
17. Grobner, T. Gadolinium--a specific trigger for the development of nephrogenic fibrosing dermopathy and nephrogenic systemic fibrosis? *Nephrol. Dial. Transplant.* **2006**, *21*, 1104-1108.
18. Abraham, J.L.; Thakral, C.; Skov, L.; Rossen, K.; Marckmann, P. Dermal inorganic gadolinium concentrations: evidence for in vivo transmetallation and long-term persistence in nephrogenic systemic fibrosis. *Br. J. Dermatol .* **2008**, *158*, 273-280.
19. Gale, E.M.; Atanasova, I.P.; Blasi, F.; Ay, I.; Caravan, P. A Manganese Alternative to Gadolinium for MRI Contrast. *J. Am. Chem. Soc.* **2015**, *137*, 15548-15557.
20. Gale, E.M.; Wey, H.Y.; Ramsay, I.; Yen, Y.F.; Sosnovik, D.E.; Caravan, P. A Manganese-based Alternative to Gadolinium: Contrast-enhanced MR Angiography, Excretion, Pharmacokinetics, and Metabolism. *Radiology* **2018**, *286*, 865-872.

21. Pan, D.; Schmieder, A.H.; Wickline, S.A.; Lanza, G.M. Manganese-based MRI contrast agents: past, present and future. *Tetrahedron* **2011**, *67*, 8431-8444.
22. Garcia-Hevia, L.; Banobre-Lopez, M.; Gallo, J. Recent Progress on Manganese-Based Nanostructures as Responsive MRI Contrast Agents. *Chemistry* **2019**, *25*, 431-441, doi:10.1002/chem.201802851.
23. Mehdizadeh, P.; Fesharaki, S.S.H.; Nouri, M.; Ale-Ebrahim, M.; Akhtari, K.; Shahpasand, K.; Saboury, A.A.; Falahati, M. Tau folding and cytotoxicity of neuroblastoma cells in the presence of manganese oxide nanoparticles: Biophysical, molecular dynamics, cellular, and molecular studies. *Int. J. Biol. Macromol.* **2019**, *125*, 674-682.
24. Lusic, H.; Grinstaff, M.W. X-ray-computed tomography contrast agents. *Chem. Rev.* **2013**, *113*, 1641-1666.
25. Lee, N.; Choi, S.H.; Hyeon, T. Nano-Sized CT Contrast Agents. *Adv. Mater.* **2013**, *25*, 2641-2660.
26. Smith, J.W.; Evans, A.T.; Costall, B.; Smythe, J.W. Thyroid hormones, brain function and cognition: a brief review. *Neurosci. Biobehav. Rev.* **2002**, *26*, 45-60.
27. Spitzweg, C.; Heufelder, A.E.; Morris, J.C. Thyroid Iodine Transport. *Thyroid* **2000**, *10*, 321-330.
28. Seeliger, E.; Lenhard, D.C.; Persson, P.B. Contrast Media Viscosity versus Osmolality in Kidney Injury: Lessons from Animal Studies. *Biomed. Res. Int.* **2014**, *2014*, 358136.
29. Solomon, R. Contrast Media: Are There Differences in Nephrotoxicity among Contrast Media? *Biomed. Res. Int.* **2014**, *2014*, 934947.
30. Andreucci, M.; Faga, T.; Pisani, A.; Sabbatini, M.; Michael, A. Acute Kidney Injury by Radiographic Contrast Media: Pathogenesis and Prevention. *Biomed. Res. Int.* **2014**, *2014*, 362725.
31. Andreucci, M.; Faga, T.; Pisani, A.; Sabbatini, M.; Russo, D.; Michael, A. The Choice of the Iodinated Radiographic Contrast Media to Prevent Contrast-Induced Nephropathy. *Advances in Nephrology* **2014**, *2014*, 691623.
32. Andreucci, M.; Solomon, R.; Tasanarong, A. Side Effects of Radiographic Contrast Media: Pathogenesis, Risk Factors, and Prevention. *Biomed. Res. Int.* **2014**, *2014*, 741018.
33. World Health, O. Assessment of iodine deficiency disorders and monitoring their elimination : a guide for programme managers. **2007**.
34. Leung, A.M.; Braverman, L.E. Consequences of excess iodine. *Nat. Rev. Endocrinol .* **2014**, *10*, 136-142.
35. Jaffer, F.A.; Weissleder, R. Molecular imaging in the clinical arena. *JAMA* **2005**, *293*, 855-862.
36. Pysz, M.A.; S.S., G.; Willmann, J.K. Molecular imaging: current status and emerging strategies. *Clin. Radiol .* **2010**, *65*, 500-516.
37. Cai, W.; Chen, X. Nanoplatforms for targeted molecular imaging in living subjects. *Small* **2007**, *3*, 1840-1854.
38. Kim, J.; Lee, N.; Hyeon, T. Recent development of nanoparticles for molecular imaging. *Phil. Trans. R. Soc. A* **2017**, *375*, 20170022.
39. Subbiah, R.; Veerapandian, M.; Yun, K.S. Nanoparticles: functionalization and multifunctional applications in biomedical sciences. *Curr. Med. Chem.* **2010**, *17*, 4559-4577, doi:10.2174/092986710794183024.
40. Mout, R.; Moyano, D.F.; Rana, S.; Rotello, V.M. Surface functionalization of nanoparticles for nanomedicine. *Chem. Soc. Rev.* **2012**, *41*, 2539-2544.
41. Elsabahy, M.; Wooley, K.L. Design of polymeric nanoparticles for biomedical delivery applications. *Chem. Soc. Rev.* **2012**, *41*, 2545-2561.
42. Hoshyar, N.; Gray, S.; Han, H.; Bao, G. The effect of nanoparticle size on in vivo pharmacokinetics and cellular interaction. *Nanomedicine (Lond.)* **2016**, *11*, 673-692.

43. He, C.; Hu, Y.; Yin, L.; Tang, C.; Yin, C. Effects of particle size and surface charge on cellular uptake and biodistribution of polymeric nanoparticles. *Biomaterials* **2010**, *31*, 3657-3666.
44. Yin Win, K.; Feng, S. Effects of particle size and surface coating on cellular uptake of polymeric nanoparticles for oral delivery of anticancer drugs. *Biomaterials* **2005**, *26*, 2713-2722.
45. Courant, T.; Roullin, G.V.; Cadiou, C.; Callewaert, M.; Andry, M.C.; Portefaix, C.; Hoeffel, C.; de Goltstein, M.C.; Port, M.; Laurent, S.; et al. Biocompatible nanoparticles and gadolinium complexes for MRI applications. *C. R. Chimie* **2013**, *16*, 531-539.
46. Ananta, J.S.; Godin, B.; Sethi, R.; Moriggi, L.; Liu, X.; Serda, R.E.; Krishnamurthy, R.; Muthupillai, R.; Bolskar, R.D.; Helm, L.; et al. Geometrical confinement of gadolinium-based contrast agents in nanoporous particles enhances T1 contrast. *Nat. Nanotechnol.* **2010**, *5*, 815-821.
47. Gizzatov, A.; Stigliano, C.; Ananta, J.S.; Sethi, R.; Xu, R.; Guven, A.; Ramirez, M.; Shen, H.; Sood, A.; Ferrari, M.; et al. Geometrical confinement of Gd(DOTA) molecules within mesoporous silicon nanoconstructs for MR imaging of cancer. *Cancer Lett.* **2014**, *352*, 97-101.
48. Ponsiglione, A.M.; Russo, M.; Torino, E. Glycosaminoglycans and Contrast Agents: The Role of Hyaluronic Acid as MRI Contrast Enhancer. *Biomolecules* **2020**, *10*.
49. Zhang, L.; Liu, T.; Xiao, Y.; Yu, D.; Zhang, N. Hyaluronic Acid-Chitosan Nanoparticles to Deliver Gd-DTPA for MR Cancer Imaging. *Nanomaterials* **2015**, *5*, 1379-1396.
50. Vecchione, D.; Grimaldi, A.M.; Forte, E.; Bevilacqua, P.; Netti, P.A.; Torino, E. Hybrid Core-Shell (HyCoS) Nanoparticles produced by Complex Coacervation for Multimodal Applications. *Sci. Rep.* **2017**, *7*, 45121.
51. Russo, M.; Ponsiglione, A.M.; Forte, E.; Netti, P.A.; Torino, E. Hydrodenticity to enhance relaxivity of gadolinium-DTPA within crosslinked hyaluronic acid nanoparticles. *Nanomedicine (Lond.)* **2017**, *12*, 2199-2210.
52. Courant, T.; Roullin, V.G.; Cadiou, C.; Callewaert, M.; Andry, M.C.; Portefaix, C.; Hoeffel, C.; de Goltstein, M.C.; Port, M.; Laurent, S.; et al. Hydrogels incorporating GdDOTA: towards highly efficient dual T1/T2 MRI contrast agents. *Angew. Chem. Int. Ed. Engl.* **2012**, *51*, 9119-9122.
53. Ponsiglione, A.M.; Russo, M.; Netti, P.A.; Torino, E. Impact of biopolymer matrices on relaxometric properties of contrast agents. *Interface Focus* **2016**, *6*, 20160061.
54. Russo, M.; Bevilacqua, P.; Netti, P.A.; Torino, E. A Microfluidic Platform to design crosslinked Hyaluronic Acid Nanoparticles (cHANPs) for enhanced MRI. *Sci. Rep.* **2016**, *6*, 37906.
55. Tammaro, O.; Costagliola di Polidoro, A.; Romano, E.; Netti, P.A.; Torino, E. A Microfluidic Platform to design Multimodal PEG - crosslinked Hyaluronic Acid Nanoparticles (PEG-cHANPs) for diagnostic applications. *Sci. Rep.* **2020**, *10*, 6028.
56. Callewaert, M.; Roullin, V.G.; Cadiou, C.; Millart, E.; Van Gulik, L.; Andry, M.C.; Portefaix, C.; Hoeffel, C.; Laurent, S.; Elst, L.V.; et al. Tuning the composition of biocompatible Gd nanohydrogels to achieve hypersensitive dual T1/T2 MRI contrast agents. *J. Mater Chem. B* **2014**, *2*, 6397-6405.
57. De Sarno, F.; Ponsiglione, A.M.; Russo, M.; Grimaldi, A.M.; Forte, E.; Netti, P.A.; Torino, E. Water-Mediated Nanostructures for Enhanced MRI: Impact of Water Dynamics on Relaxometric Properties of Gd-DTPA. *Theranostics* **2019**, *9*, 1809-1824.
58. Capretto, L.; Carugo, D.; Mazzitelli, S.; Nastruzzi, C.; Zhang, X. Microfluidic and lab-on-a-chip preparation routes for organic nanoparticles and vesicular systems for nanomedicine applications. *Adv. Drug Deliv. Rev.* **2013**, *65*, 1496-1532.
59. Karnik, R.; Gu, F.; Basto, P.; Cannizzaro, C.; Dean, L.; Kyei-Manu, W.; Langer, R.; Farokhzad, O.C. Microfluidic Platform for Controlled Synthesis of Polymeric Nanoparticles. *Nano Lett.* **2008**, *8*, 2906-2912.

60. Smeraldo, A.; Ponsiglione, A.M.; Netti, P.A.; Torino, E. Tuning of Hydrogel Architectures by Ionotropic Gelation in Microfluidics: Beyond Batch Processing to Multimodal Diagnostics. *Biomedicines* **2021**, *9*.
61. Patel, J.L.; Goyal, R.K. Applications of artificial neural networks in medical science. *Curr. Clin. Pharmacol .* **2007**, *2*, 217-226.
62. Damiati, S.A.; Rossi, D.; Joensson, H.N.; Damiati, S. Artificial intelligence application for rapid fabrication of size-tunable PLGA microparticles in microfluidics. *Sci. Rep.* **2020**, *10*, 19517.
63. Youshia, J.; Ali, M.E.; Lamprecht, A. Artificial neural network based particle size prediction of polymeric nanoparticles. *Eur. J. Pharm. Biopharm.* **2017**, *119*, 333-342.
64. Aghajani, M.; Shahverdi, A.R.; Rezayat, S.M.; Amini, M.A.; Amani, A. Preparation and optimization of acetaminophen nanosuspension through nanoprecipitation using microfluidic devices: an artificial neural networks study. *Pharm. Dev. Technol.* **2013**, *18*, 609-618.
65. Aghajani, M.H.; Pashazadeh, A.M.; Mostafavi, S.H.; Abbasi, S.; Hajibagheri-Fard, M.; Assadi, M.; Aghajani, M. Size Control in the Nanoprecipitation Process of Stable Iodine (^{127}I) Using Microchannel Reactor-Optimization by Artificial Neural Networks. *AAPS PharmSciTech* **2015**, *16*, 1059-1068.
66. Aghajani, M.; Shahverdi, A.R.; Amani, A. The use of artificial neural networks for optimizing polydispersity index (PDI) in nanoprecipitation process of acetaminophen in microfluidic devices. *AAPS PharmSciTech* **2012**, *13*, 1293-1301.

CHAPTER I – A MICROFLUIDIC APPROACH TO TUNE CHITOSAN-HYALURONIC ACID HYDROGEL ARCHITECTURES FOR MULTIMODAL IMAGING PURPOSES

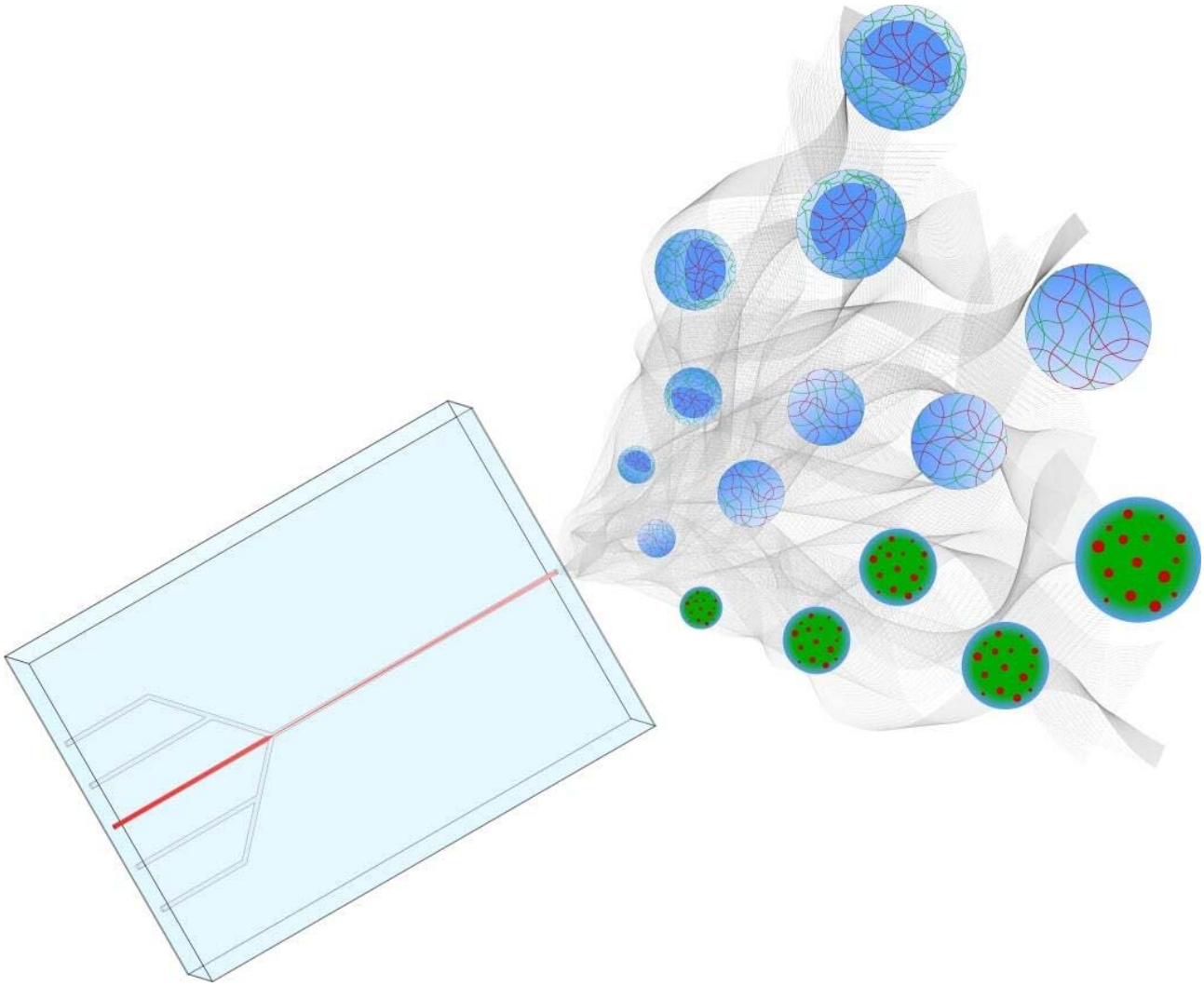

Abstract

Microfluidics is emerging as a promising tool to handle the physicochemical properties of nanoparticles. Indeed, microfluidic-based techniques offer more advantages over batch processes, allowing to finely tune the process parameters. In particular, the use of microfluidics to produce nanoparticles has led the way into the development of different nanostructures with the aim to improve the detection and treatment of several diseases. In this case, an ionotropic gelation via Chitosan - TPP crosslinking followed by Hyaluronic acid - Chitosan complex coacervation has been carried out in a custom-designed microfluidic chip to produce different nanoarchitectures. Results show that microfluidics allows to tune the morphological structures of nanoparticles by controlling

the flow rates. Besides the nanostructures, the encapsulation of a gadolinium contrast agent for Magnetic Resonance Imaging and a dye for Optical Imaging within the polymer nanostructure demonstrates the ability of this latter to enhance the relaxometric properties of gadolinium by attaining the *Hydrodenticity* and to be used as a promising nanocarrier for multimodal imaging applications.

1.1 Introduction

In the last few years, nanostructured materials have attracted considerable interest due to the opportunity to modulate their multifunctional properties depending on the particular application [1-4]. Among them, polymer nanoparticles (NPs) have proven to be very promising for improving imaging techniques and therapeutic treatments [5,6]. General advantages of nanovectors include specific targeting, controlled release, protection of active molecules, and the ability to carry one or more therapeutic and/or imaging agents, simultaneously, for theranostic purposes [7]. In addition, it has been proved that polymer NPs, in particular hydrogels, can be designed to improve the imaging performances, targeting ability, and potentially reduce the fast clearance of drugs and diagnostic agents from the bloodstream [8-12].

Natural polymers like polysaccharides (Hyaluronic Acid (HA), Chitosan (CS), Dextran, Alginate) and proteins (collagen, albumin) as well as synthetic polymers (polylactic acid (PLA), polyglycolic acid (PGA), polylactide-coglycolide acid (PLGA), polyethylene glycol (PEG)) are widely used due to their low immunogenicity and cytotoxicity also at high concentration, tunable biodegradation behaviour and versatile utilization in medical applications [13-17]. Among them, HA and its derivatives have been extensively studied for the development of several carrier systems for cancer diagnosis, staging and therapy [18-21]. HA has also been used in combination with several polymers, such as CS, and the usefulness of these combinations is well documented for different bio-applications, like drug delivery and diagnostics [19,22,23]. For example, Chen and co-workers [24] report a yolk-shell structure with a radioluminescent yolk based on Gd2O3: Eu nanospheres, an up-conversion luminescent in a silica shell, and a coating constituted by HA/CS combination for pH-triggered drug release. Particularly, remarkable results have been achieved by Courant et al. [9], who coprecipitate randomly HA and CS to obtain high-relaxivity gadolinium -based nanoparticles for Magnetic Resonance Imaging (MRI) applications.

Furthermore, recently, Vecchione et al. [10,25] have produced core-shell biopolymer particles for multimodal imaging purposes through a complex coacervation process driven by temperature and high-pressure homogenization. The architecture, shaped in a CS core and a HA shell, is designed to

co-encapsulate a clinically relevant contrast agent (CA) for MRI and a dye for Optical Imaging. Successively, the same nanostructure has been decorated with the peptide pA20-36 to selectively target B-cell lymphoma cells and successfully tested in a murine model for in vivo theranostic applications [26]. As showed in their previous works [11,27-31], these authors demonstrated that the relaxometric properties of a gadolinium-based CA entrapped in a polymer network can be influenced through a proper control of the structural properties of polymer-based nanohydrogel such as crosslinking density, mesh size and hydrophilicity leading to enhance its relaxivity. Indeed, as explained by Russo et al., the boosting in the relaxivity is achieved when a complex equilibrium between the water osmotic pressure, the elastodynamic forces of the polymer chains and the hydration degree of the CA is reached [11,31]. This equilibrium responsible for the relaxation enhancement, defined as the novel concept of *Hydrodenticity* [31], can be obtained, under specific conditions, by controlling the process parameters used to produce CA-loaded nanostructures.

As described above, the structural properties of the polymer network turn out to be fundamental to give multiple functionalities to the nanostructures: *Hydrodenticity*, multistage release, tunable degradation behaviour, stability to solvents and biological stimuli, stealth properties, etc. In this regard, the combined use of two or more different polymers allows a further tunable parameter of the structural properties [32-34]. In particular, it is worth highlighting that CS and HA have widely proven to have a huge potential in this field [35-39]. However, to combine CS and HA into multifunctional nanovectors to obtain desired physicochemical and morphological properties, many methodologies have been proposed such as ionotropic gelation, complex coacervation, self-assembly and nano- and micro-emulsion techniques [17,40-44]. Among these, the ionotropic gelation has proven to be a complex but promising way to synthesize CS-HA nanoparticles. It is based on the interaction of a cation (or an anion) with one or more ionic polymers to form a highly inter or intra crosslinked structure. Main advantages of the ionotropic gelation lie in the flexibility of the process due to the numerous parameters that can be modified for the proper success of the reaction such as pH, temperature, ionic strength, polyacid/polybase ratio, polymer concentration and molecular weight.

However , it has also been reported that fine control over the final product's features is difficult to achieve through the traditional batch protocols [45,46] , whose main drawbacks lies in the poor control of mixing and separation of particles, resulting in polydispersity and batch-to-batch variations [47]. Consequently, these technical issues are limiting the translation of CS-HA based architecture in preclinical and clinical practice. In this perspective, a microfluidic design of the

processes has already proven to be a way to overcome this issue, improving the synthesis of nanoparticles and accelerate their transition to clinical evaluation [48-54]. Reactions in microfluidic devices are carried out with a low amount of fluids within small channels [54-57]. It enables fine control and manipulation of fluids and their interfaces, rapid and uniform heat and mass transfer thanks to the established laminar flow [58-61].

In particular, microfluidics proved to be a promising and effective tool for the rational design of polymer NPs as imaging probes and drug delivery systems [62,63]. As showed in recent studies conducted by Russo et al. [64,65], the microfluidic hydrodynamic flow focusing (HFF) approach allows fine tuning of the structural characteristics of HA-based nanohydrogels by tuning process parameters such as flow rate ratio and compounds' concentration. In the presence of an MRI CA, this accurate control of the process permits the attainment of the above-mentioned *Hydrodenticity*, thereby enhancing the relaxometric properties of the CA within the nanostructure.

1.2 Aim of the Chapter I

In this Chapter, we aim to design and produce CS-HA NPs exploiting the ionotropic gelation by microfluidics. Taking advantage of the acquired expertise in microfluidic synthesis of polymer nanoparticles by hydrodynamic flow focusing, we intend to demonstrate how the combination of ionotropic gelation and microfluidics allows to tune the morphology of the complex architectures through the use of a custom-designed microfluidic chip with a specific geometry tailored to achieve the desired hydrodynamic flow focusing conditions and coupling of the compounds. Furthermore, we want to evaluate the *Hydrodenticity* behaviour and the co-encapsulation ability of the nanostructures for multimodal imaging applications.

1.3 Materials and Methods

1.3.1 Materials

Hyaluronic acid (HA) (M_W = 50 kDa) has been purchased from CreativePEGWorks (Chapel Hill, NC, USA). Chitosan (CS) (M_W = 50 kDa) and sodium tripolyphosphate (TPP) (M_W = 367.86 Da) have been purchased from Sigma-Aldrich (St. Louis, MO, USA). Acetone (Sigma-Aldrich, St. Louis, MO, USA) has been used for samples collection and dialysis, while ethanol (Carlo Erba, Milan, Italy) has been used in the successive step of dialysis to change sample collection from acetone to water. Commercially available Gd-DTPA (M_W = 547.57 Da, Sigma-Aldrich, St. Louis, MO, USA), a well-known low-risk CA for MRI, and ATTO488 (M_W = 804 Da; λ = 480-515 nm) have been purchased by Sigma-Aldrich (St. Louis, MO, USA). Milli-Q water (Milli-Q Plus, Q-POD®, Merck KGaA, Darmstadt, Germany) has been used to prepare polymer solutions and dialysis.

1.3.2 Microfluidic platform

The microfluidic platform is composed of a system of three syringes (5 mL PTFE PEEK tubing connector, GmbH, Ilmenau, Germany) that serve as reservoir for the reagents. Each syringe is controlled by a low-pressure syringe pump (Low Pressure Syringe Pump neMESYS 290N by CETONI, Korbußen, Germany) to precisely controls the volume of fluid pushed through the channels. Flow rates can be tuned using a PC software that acts on the pump motor. Syringes are connected to the microfluidic chip through PTFE tubing and connectors (Dolomite Microfluidics, Blacktrace Holdings Ltd., Royston, UK) and are equipped with 2-way in-line valves (Dolomite Microfluidics, Blacktrace Holdings Ltd., Royston, UK) to manually open and close the line for each syringe. Reactions take place in the main body of a custom-made quartz glass microfluidic chip, geometrically designed to obtain a hydrodynamic flow focusing at the channels junction. All channels of the microfluidic chip have the same cross-section of 160 x 150 μm. Fluid from the outlet is collected, through a PTFE tubing, in a glass Petri prefilled with water or acetone.

1.3.3 Production of CS-HA Nanoparticles

The initial step consists of the preparation of polycationic (CS) and polyanionic solutions (HA and TPP). Starting from previously prepared stocks at 0.2 % w/v, the first solution is obtained by mixing CS (concentration range from 0.00625 to 0.2 % w/v) in an acetic acid buffer (1% v/v) while the second one is obtained dissolving HA (concentration range from 0.002 to 0.008 % w/v) and TPP (concentration range from 0.003 to 0.012 % w/v) in water , both stirred at 300 rpm for 30 min. Polycationic solution (CS) is pushed in the middle channel while polyanionic solution (HA and TPP) in the two side channels as represented in Figure I-1a. Sample is collected in Petri dishes filled with acetone or water and covered with aluminum foil to limit solvent evaporation. After each usage, the chip is repeatedly washed with water and 1% v/v acetic acid aqueous solution. Moreover, to remove possible residuals of the precipitated materials within the channels, the chip is immerged overnight in a piranha solution composed of ¼ nitric acid and ¾ sulphuric acid.

1.3.4 Nanoparticles morphological characterization

Scanning electron microscope (SEM, Ultraplus Field Emission, Carl Zeiss, Oberkochen, Germany) has been used to analyze NPs morphological and structural surface features. In particular, samples are dropped on glass directly from microfluidic platform outlet or filtered, after collection and dialysis, on membrane of 50 nm pore size. Nanoparticles are coated with 5.5 nm Au prior observation. Instead, NPs internal features are examined with transmission electron microscope (TEM, Tecnai FEI®, Hillsboro, OR, USA) by collecting sample on Formvar/Carbon 200 mesh Cu

Agar® small net from microfluidic platform outlet or dropping off 20-50 μL of solution on it, before or after dialysis.

1.3.5 Gd-DTPA loading and evaluation of the Encapsulation Efficiency

Induced Coupled Plasma Mass Spectrometry (ICP-MS, NexION 350 Perkin Elmer Inc., Waltham, MA, USA) is used to assess the concentration of Gd-DTPA loaded within the NPs. A suspension of Gd-loaded CS-HA nanoparticles in deionized water at a concentration of 250,000 particles/mL without dissolution is injected in the instrument. Syngistix NanoApplication (Module PerkinElmer Inc., Waltham, MA, USA) software is used to collect and process data. Gd is measured at m/z 157 using a 100 μs dwell time with no settling time. Successively, results are compared to the known initially added amount of Gd-DPTA to obtain an estimate of the encapsulation efficiency.

1.3.6 *In vitro* MRI

Longitudinal relaxation time is evaluated by Minispec mq60 BRUKER benchtop relaxometer (Bruker Corporation,Billerica, MA, USA, magnetic field strength: 1.41 T) . A glass tube is loaded with 300 μL of the sample and then placed into the NMR probe for about 15 min for thermal equilibration. Firstly, the Free Induction Decay sequence (FID) is used to evaluate the best value of the Gain to control the saturation of the signal. Longitudinal relaxation times (T_1) are then determined by saturation recovery and inversion recovery pulse sequences. The relaxation time distribution is obtained by CONTIN Algorithm [66].

1.3.7 Spectrofluorimetric analysis

Spectrofluorimetric analysis (EnSpire Multimode Plate Reader, PerkinElmer Inc, Waltham, MA, USA) is performed to detect ATTO488 and provide information regarding its concentration within nanoparticles in a range of 0-250 pmol/mL.

1.3.8 Preliminary *in vitro* cell test

Cytotoxicity studies on Human brain Glioblastoma astrocytoma cells (U87-MG) are performed to preliminary assess NPs biocompatibility. U87 MG cells are seeded in 96-well plates (5 × 104 cells/well) and let adhere for 24h in free medium (DMEM, 1% penicillin/streptomycin and 1% L-glutamine). Adherent cells are then incubated with medium supplied with NPs (22 μg/mL) or free medium as negative control. Cells are checked for viability for 8 or 24 hours by means of MTT test.

1.4 Results

1.4.1 Ionotropic gelation controlled by Hydrodynamic Flow Focusing for production CS-HA nanostructures

As previously reported [11,67], the hydrodynamic flow focusing (HFF) is obtained when a middle stream is squeezed between two adjacent streams flowing at a higher flow rate within microfluidic channels. In particular, the Flow Rate Ratio (FR^2), defined as the ratio between the flow rate of the middle channel (μL/min) and the flow rate of only one of the side channels (μL/min), is calculated as follows [11]:

$$FR^2 = \frac{Flow\ Rate|_{middle\ channel}}{Flow\ Rate|_{side\ channel}}$$

HFF has been applied to different processes such as the flow focused nanoprecipitation, where the lower is the FR^2, the narrower is the hydrodynamic flow focusing. The width of this latter is strictly linked to mutual mixing and diffusion phenomena of the flows and responsible for the thermodynamic process [68]. Indeed, the relationship between FR^2 and the mixing time is derived from the equation below:

$$\tau_{mix} \sim \frac{w_f^2}{4D} \approx \frac{w^2}{9D} \frac{1}{(1 + 1/FR^2)^2}$$

where w_f is the width of the hydrodynamic flow focusing, w represents the channel width and D the diffusion coefficient of the solvent [55].

Several studies conducted on flow focused nanoprecipitation also demonstrated that the laminar flow condition is achieved within the microchannels due to the low Reynolds number that ensure a proper supersaturation condition and homogenous particle formation kinetics [55,69,70].

Therefore, the theoretical knowledge of HFF can be harnessed to induce ionotropic gelation within the microfluidic channel and tune the process parameters (flow rates, FR^2, concentration and ratio of the reagents) to control the morphology of the nanostructures.

Generally, in ionotropic gelation, TPP binds the charged amino groups of CS leading to the formation of a three-dimensional network of the ionic crosslinked moiety [10]. Usually, to get the cation during the ionic gelation process, chitosan is dissolved in an aqueous acidic solution. This latter is then added drop-wise under continuous stirring based on the capability of polyelectrolytes to traverse links in the presence of counter ions to form nanoparticles [71-73]. Here, HA and CS are chosen as oppositely charged polyelectrolytes. In particular, chitosan undergoes ionic gelation and

precipitates to form spherical particles due to the binding between oppositely charged species, further stabilized by the presence of TPP.

In our system, a HA and TPP water solution flows through the side channels, while a 1% v/v acetic acid aqueous solution of CS is pushed in the middle channel of the microfluidic chip. A schematic representation of the process is shown in Figure I-1.

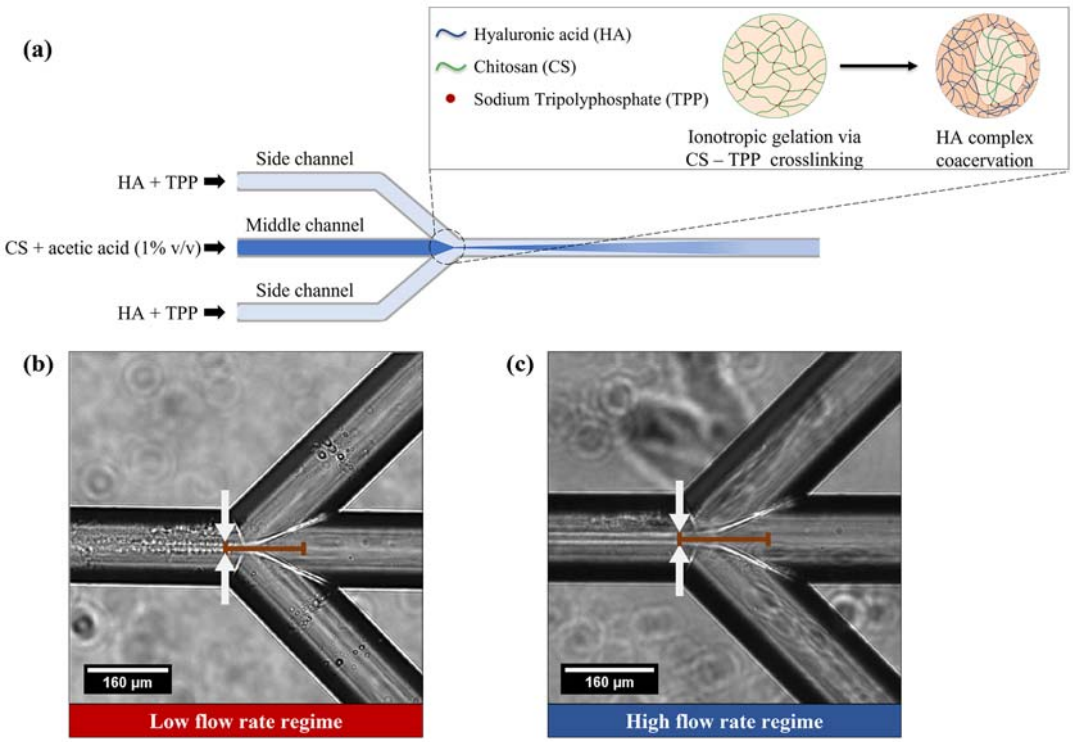

Figure I-1. (a) Graphic illustration of the hydrodynamic flow focusing within the microfluidic chip. Middle and side streams lead to NPs formation through ionotropic gelation via CS-TPP crosslinking followed by HA-CS complex coacervation; **(b,c)** Optical Image of the microfluidic device showing the hydrodynamic flow focusing at **(b)** *Low flow rate regime* (middle channel flow rate < 1 µL/min) and **(c)** *High flow rate regime* (middle channel flow rate ≥ 1 µL/min). In both images the width of the focusing stream is indicated by white arrows, while its elongation at the chip junction is represented by the brown line along the middle channel.

In the proposed set-up (Figure I-1a), the kinetic of the gelation is controlled by the hydrodynamic flow focusing through the lateral injection of HA and TPP at different flow rates. This fine control of the flow rate ratio tunes the mixing time and dosage among the reagents. NPs formation is achieved through the partial precipitation of the chitosan in water and ionotropic gelation via CS-TPP crosslinking followed by HA-CS complex coacervation along the middle stream.

A similar approach that takes advantage of the mutual diffusion and precipitation of the components has been already published by our group using an emulsion-based batch approach and

it is proposed here, for the first time, in a continuous mode using microfluidics to avoid polydispersity and improve purification and control of the structural properties[10,25,26].

In this microfluidic approach, different parameters have been tested with particular attention to the following: (i) FR^2 (ranging from 0.05 to 0.5); (ii) flow rates (ranging from 0.2 to 20 μL/min for the middle channel and from 0.5 to 100 μL/min for side channels); (iii) CS:HA weight ratio calculated at the chip junction (ranging from 0.0781 to 6.25).

1.4.2 Identification of Operating Regimes and fluidodynamic threshold for the experimental campaign

Most experiments have been carried out in two different operating flow rate regimes (Figure I-1b and c) identified as follow : a change in focusing width together with a shift in the position of the relative focusing has been visually observed, through an optical microscope, when a certain threshold is overcome. These observations allow us to choose experimentally two conditions: (1) a *Low flow rate regime*, i.e. middle channel flow rate < 1 μL/min, flow focusing width w below 15 μm and a mixing time τ_{mix} below 30 ms (Figure I-1b); (2) a *High flow rate regime*, i.e. middle channel flow rate ≥ 1 μL/min, flow focusing width w above 15 μm and a mixing time τ_{mix} above 30 ms (Figure I-1c). In both cases, the mixing time range is in the order of tens of milliseconds, which is typically used for polysaccharides nanoparticles fabrication [74]. The experimentally set threshold allows us to investigate two processes characterized by longer and shorter mixing times, respectively higher and lower than the aggregation time reported for CS-based nanoparticles [75,76].

1.4.3 Rational of the experimental campaign on ionotropic gelation in microfluidics

As first step, a detailed analysis of the literature has been performed to explore batch processes implementing ionotropic gelation and to identify the optimal thermodynamic conditions to implement in microfluidics.

The study has revealed that the polymer ratio ,usually kept constant at 6.25 (CS:HA = 6.25:1 weight ratio), is a standard parameter used in the ionotropic gelation as described by Callewaert et al. [23]. The tuning of flow rates and, therefore, of the flow rate ratio allows the translation of the above-mentioned polymer ratio condition to microfluidics.

In particular, during the experimental campaign, the gap from the saturation concentration of the compounds has been investigated to understand how it affects both the nanoprecipitation and the ionotropic gelation, influencing the diffusion and electrostatic coupling of the polymers.

Among the tested conditions and parameters, the experimental work has been focused on those that experimentally allowed reproducibility of the results, stability of the hydrodynamic flow focusing

and high throughput. In particular, an FR^2 of 0.5 has been found out as the most reliable value to carry out the process. In detail, by keeping constant the FR^2, the experiments conducted at the middle channel flow rate of 0.3 μL/min and side channels of 0.6 μL/min refer to the *Low flow rate regime* while those in the *High flow rate regime* have been performed at middle and side channel flow rate of 3 and 6 μL/min, respectively. The effect of polymer concentrations (ranging from 0.05 to 0.2 % w/v for CS and from 0.002 to 0.008 % w/v for HA) and polymer ratios (CS:HA ranging from 1.56 to 6.25) at $FR^2 = 0.5$ have been investigated as discussed in the following at *High* and *Low flow rate regimes*. Representative results obtained using other FR^2 conditions are displayed in the Figure I-S1 of the Appendix A.

1.4.4 Effect of the concentration of the polymers at $FR^2 = 0.5$ and constant polymer ratio of 6.25

Firstly, by keeping constant the FR^2 and the polymer weight ratio, the effect of simultaneously increasing CS and HA concentrations have been explored at *Low* and *High flow rate regime*. In particular, polymer concentrations have been scaled to values feasible in the microfluidic environment.

Z- Average Size obtained by DLS and SEM images, reported in Figure I-2a, reveals the presence of coacervates, whose size and polydispersity decrease with the increasing CS concentration. This is an unexpected phenomenon since the increase in concentration usually brings an increase in the particles size. Indeed, the viscosity of the organic phase increases with the polymer concentration, reducing its diffusion rate towards the aqueous phase and subsequently resulting in larger nanoparticles [77].

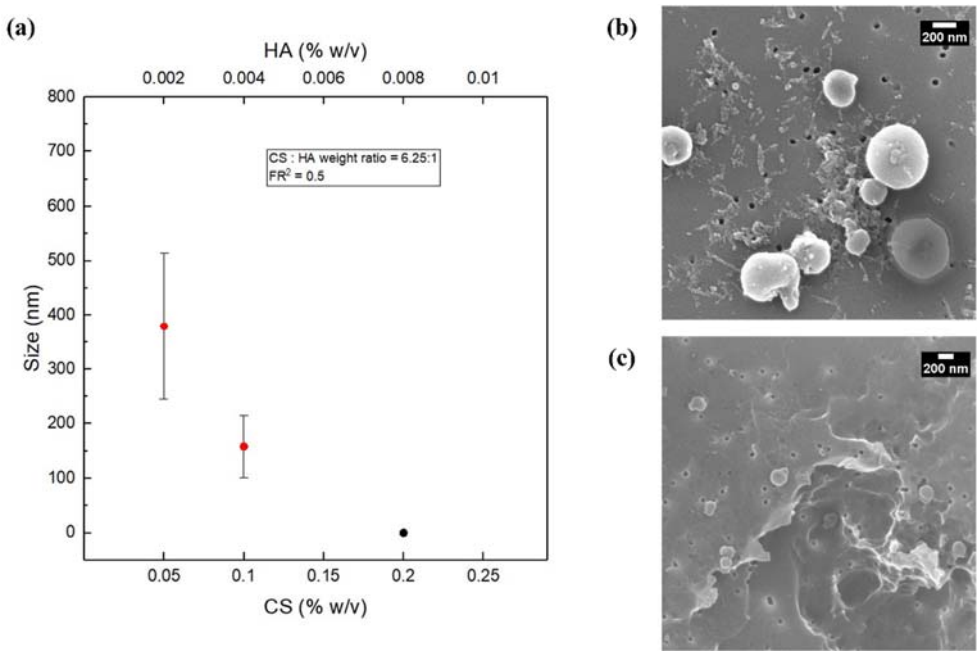

Figure I-2. NPs size and morphology at constant polymer ratio reproducing batch conditions: **(a)** Plot showing size vs CS and HA concentrations at CS: HA weight ratio equal to 6.25 at *Low flow rate regime* (MFR=0.3 μL/min and SFR=0.6 μL/min). The black point indicates a not measurable size due to the only presence of macroaggregates and unreacted materials (see Figure I- S2 of the Appendix A); **(b)** CS= 0.05 %w/v; **(c)** CS = 0.1 %w/v.

The improvement of the stability of the hydrodynamic flow focusing can provide an explanation. Indeed, even a slight increment of the concentrations of the polymer induces the increase of the viscosity, the reduction in the fluctuation of the focusing and better control of the nanoprecipitation, promoting the nucleation to the detriment of the growth [70]. This interpretation is confirmed by the results at the highest CS concentrations, equal to 0.2% w/v where, indeed, this latter condition produces a stable focusing but causes a massive precipitation and promotes the formation of big aggregates instead of NPs [67,78]. At *High flow rate regime,* a similar behaviour has been observed.

1.4.5 Effect of the polymer ratio at $FR^2 = 0.5$

Successively, the effect of polymer concentrations (ranging from 0.05 to 0.2 % w/v for CS and from 0.002 to 0.008 % w/v for HA) and polymer ratios (CS:HA ranging from1.56 to 6.25) at $FR^2 = 0.5$ has been investigated at both *High* and *Low flow rate regimes*.

In details, polymer ratios CS:HA equal to 1.56 (CS=0.0125 %w/v, HA=0.002 %w/v; CS=0.05 %w/v, HA=0.008 %w/v) and CS:HA equal to 3.12 (CS=0.1 %w/v, HA=0.008 %w/v; CS=0.025 %w/v, HA=0.002 %w/v) have been analyzed. Regardless of the flow rate regimes, results show that size grows when polymer ratio increases (Figure I-3 and 4).

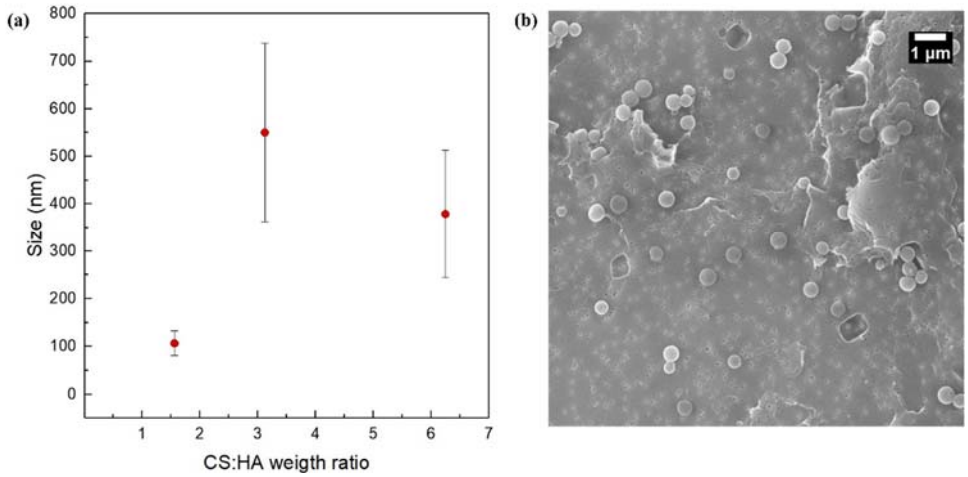

Figure I-3. NPs size and morphology at different polymer ratios at *Low flow rate regime* and $FR^2 = 0.5$: **(a)** Plot of NPs size vs CS: HA weight ratio; **(b)** representative SEM image at CS: HA weigth ratio equal to 3.12.

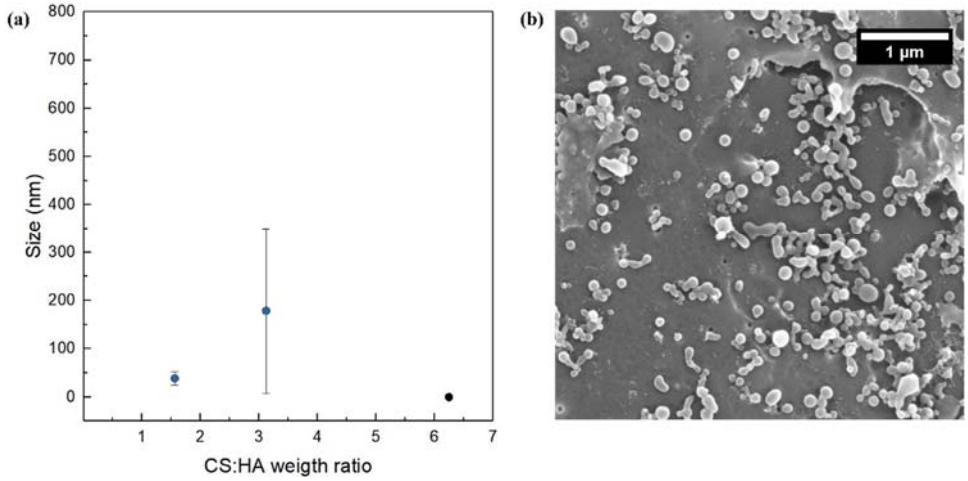

Figure I-4. NPs size and morphology at different polymer ratios at *High flow rate regime* and $FR^2 = 0.5$: **(a)** Plot of NPs size vs CS: HA weight ratio; **(b)** representative SEM image at CS: HA weigth ratio equal to 1.56. The black point indicates, at *High flow rate regime* and CS:HA=6.25, a not measurable size has been identified as result of macroaggregates and unreacted materials (see Figure I- S3 of the Appendix A).

The explanation can be found in the role played by the nucleation phenomenon. Indeed,as already reported, the higher is the concentrations of the polymers, the higher is the size of starting nuclei and the more favourites are the growth phenomena [55]. Moreover, the size of the NPs increases by shifting from *High flow rate regime* to *Low flow rate regime*. In this latter case, the hydrodynamic flow focusing starts closer to the chip junction, promoting physical aggregation. This means that the aggregation is promoted more than nucleation due to the longer polymer availability at the channel crossing, so leading to a higher mean size of the NPs. A similar effect has also been reported previously by Nemati et al. [79] for the use of microfluidics to tune size and shape of chitosan NPs

adsorbing Hg from aqueous solutions for environmental applications. This effect can also be compared with results obtained by other authors in different contexts and proving the fine tunability of the process parameters in microfluidics [78,80,81].

1.4.6 Interpretation of the Operating Regimes and obtained morphologies

NPs morphologies obtained at $FR^2 = 0.5$ and two CS:HA ratio at *High* and *Low flow rates regimes* have been compared in Figure I-5.

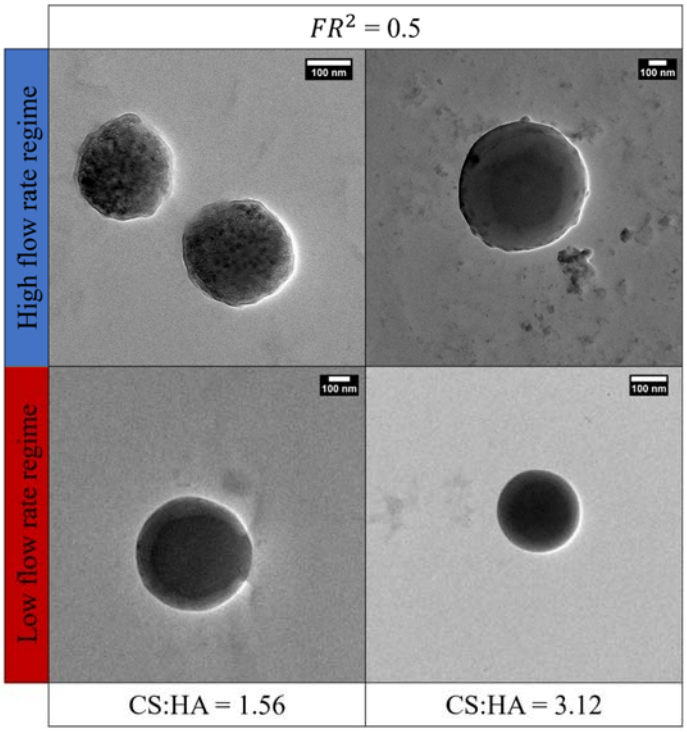

Figure I-5. NPs morphologies obtained by TEM characterization for two different CS:HA weight ratio at constant FR^2 at *High* and *Low flow rate regime*. Sizes range from: upper left 38.57 ± 14.31 nm; upper right 178.63 ±171.47 nm; lower left 471.86± 67.28 nm; lower right 150.33 ± 112.01 nm.

Looking at Figure I- 5, it is worth to notice that the *High flow rate regime* promotes the transition to different morphologies like coprecipitate and core-shell NPs thanks to parameters' modulation while at the *Low flow rate regime*, NPs with a mainly core-shell morphological structure are obtained. At *Low flow rate regime*, the overall size of the core-shell nanostructure as well as the relative dimensions between the core and shell area can be changed by tuning microfluidic process conditions. Moreover, the effect of TPP concentration on the final NPs morphology has also been investigated (Figure I-S4 of the Appendix A). In order to get an overview of the obtained

morphologies, two visual plots at *Low* and *High flow rates regimes* with additional TEM images have been included in the Appendix A (Figure I-S5 and Figure I- S6).

These results highlight microfluidics' ability, determined by the competition between the fluidodynamic forces and the thermodynamics of ionotropic gelation, to tune the parameters to obtain a range of nanoarchitectures attractive from both research and industrial viewpoint in the nanomedicine field [81].

1.4.7 Understanding of the role of fluidodynamic regimes in ionotropic gelation implemented in microfluidics

Reynolds number (Re) values have been investigated to figure out the effect of the *flow rate regimes* on the fluidodynamics [82]. Taking into account the defined 1 μL/min threshold, Re values at FR^2 = 0.5 have been calculated approximately considering the two reproducible conditions previously reported: 0.6 - 0.3 and 6 – 3 μL/min for *Low* and *High flow rates regimes*, respectively. Reynold numbers at different CS and HA concentrations, distinguishing between *High* and *Low flow rate regimes*, are shown in the following Figure I-6.

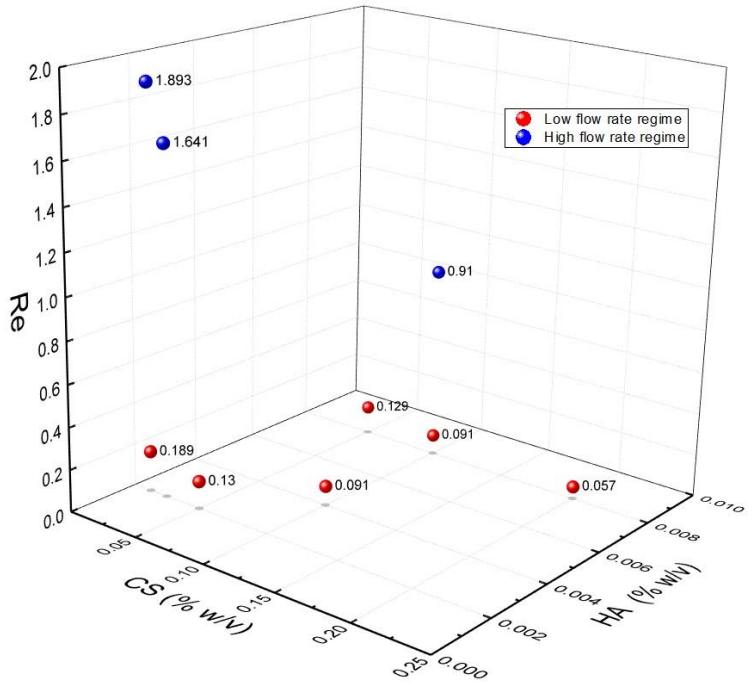

Figure I-6. Characterization of the fluidodynamic regime through Reynolds numbers at different polymer concentrations at *Low* (0.6 – 0.3 – 0.6 μL/min) and *High* (6 – 3 – 6 μL/min) *flow rate regimes*.

Re values confirm that laminar flow within the microfluidic device is always guaranteed. However, another threshold has been observed, which identifies the transition from the *Low* to the *High flow rate regime*. In the case of *High flow rate regime*, phenomena are driven by the fluid velocity and,

therefore, the mixing processes are faster than coacervation also producing coprecipitated morphologies. Instead, at *Low flow rate regime*, the viscous forces drive the coacervation phenomena due to the predominant properties of the materials. The borderline condition reached at Re = 0.91 confirms this explanation. In fact, despite in the *High flow rate regime*, an equilibrium between the inertial and viscous forces is obtained leading to the formation of core-shell morphologies, as already reported in the Figure I-5 (CS:HA= 3.12).

1.4.8 Encapsulation Efficiency and multimodal properties of the hydrogel nanostructures

1.4.8.1 In vitro MRI

The reproducibility of the trial, the high throughput and the observed core-shell morphology have been the leading parameters to identify the best condition for the NPs formation (FR^2 = 0.5, HA = 0.008 %w/v, CS = 0.1 %w/v, TPP = 0.012 %w/v and CS: HA = 3.12). Starting from these conditions, gadolinium has been introduced in the microfluidic process by adding it, at a concentration empirically set equal to that of CS (Gd = 0.1 % w/v), to the polycationic solution.

After dialysis, the presence of Gd slightly affect the size of NPs since it attracts a high amount of water molecules into the polymer matrix leading to larger NPs. For this reason, the Encapsulation Efficiency (EE) has been evaluated by measuring the concentration of the Gd-DTPA within the NPs by ICP-MS and then comparing it to the initial concentration used in the microfluidic process, according to the following formula [83]:

$$EE = \left(\frac{C_{en}}{C_i}\right) \times 100$$

where C_{en} is the Gd-DTPA concentration measured by ICP-MS and C_i is the theoretical Gd-DTPA concentration used in the process.

As proven by ICP-MS values, Gd-DTPA is entrapped within the polymeric matrix resulting in an estimated EE equal to 11.95%. In addition, the longitudinal relaxation time, T_1, of the Gd-DTPA - loaded NPs has been measured using a benchtop relaxometer and compared with the T_1 of both water and free Gd-DTPA in water (Figure I-7).

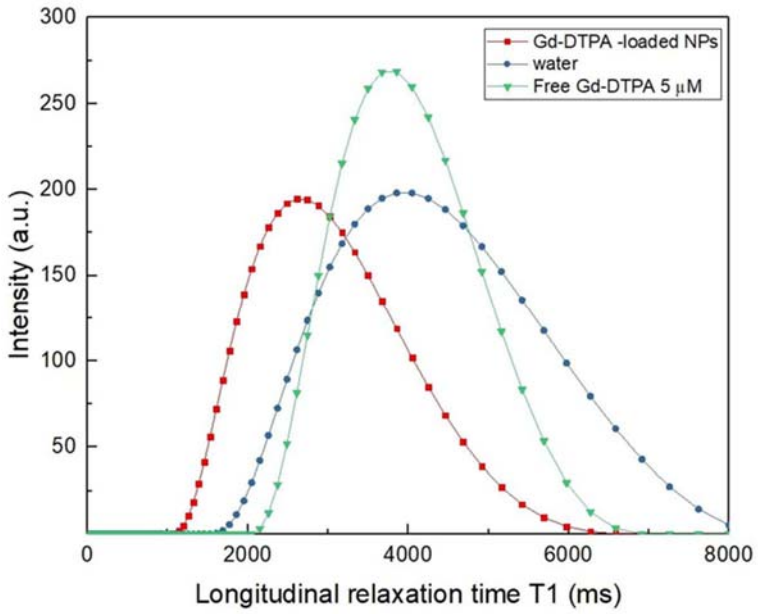

Figure I-7. Relaxation time curves for Gd-DTPA-loaded NPs in water compared to free water and to the corresponding free Gd-DTPA in water.

The T_1 distribution comparison between Gd-DTPA-loaded NPs and the corresponding free Gd-DTPA in water measured by ICP-MS (Gd-DTPA = 5 μM), highlights a 3.8-fold higher relaxivity in the case of loaded NPs, corresponding to a 12.3% enhancement in the longitudinal relaxation rate. These values arise from the water-mediated interaction between the polymer and the metal chelate as described by the *Hydrodenticity* concept. In details, the hydrophilic behaviour of both polymers attracts a large amount of water inside the polymer structure that affects water molecules dynamics and increases interactions between water molecules and the metal chelate. This improved hydration degree of Gd-DTPA results in a relaxivity boosting of the CA leading to an enhancement of the intensity of the MRI signal and so a better contrast between distinct tissues.

1.4.8.2 In vitro Optical Imaging

To demonstrate the multimodal imaging ability of the NPs, ATTO488 fluorophore has been simultaneously added to the polyanionic solution (35 μg/mL) in a one-step process. A concentration of 7 pmol/mL (EE = 16.1 %) of the encapsulated ATTO488 has been estimated through spectrofluorimetric measurements.

1.4.9 In vitro cytotoxicity

Preliminary viability of U87 cells exposed to CS-HA NPs, obtained at the process conditions of FR^2 = 0.5, HA = 0.008 %w/v, CS = 0.1 %w/v, TPP = 0.012 %w/v and CS: HA = 3.12, are displayed in Figure

I-8. Results showed no significant cytotoxicity at different time point up to 24 hours of incubation for a nanoparticle concentration higher than 20 μgr/mL.

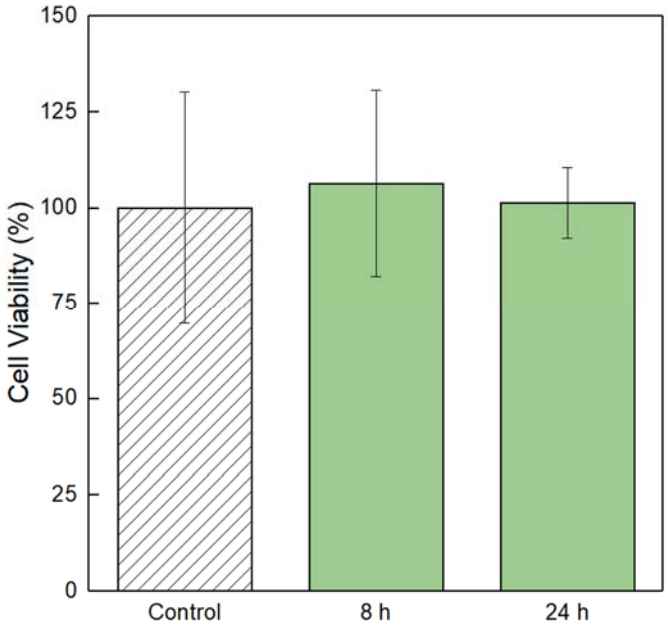

Figure I-8. In vitro cytotoxicity of CS-HA NPs in contact with U87 MG cells at two different time points. NPs have been produced using the best conditions found out during the experimental campaign (High flow rate regime (6 – 3 – 6 μL/min), HA = 0.008 %w/v, CS = 0.1 %w/v, TPP = 0.012 %w/v).

1.5 Conclusion

Starting with the study of batch process conditions, a one-step hydrodynamic flow-focusing process to produce CS-HA NPs by ionotropic gelation has been implemented in a custom-designed microfluidic platform to obtain tailored structures and morphologies by tuning the process parameters. The control over the gelation reaction, occurring in the microfluidic chip, has been achieved by changing the flow rates of the inlets, the volumetric flow rate ratio and the ratio of the different compounds adopted (polymers and crosslinker), producing a variety of nanostructures with different morphologies.

The advantages of the microfluidic flow focusing approach in the design of HA-CS NPs lie, on the one hand, in the possibility to overcome the drawbacks of batch processes (time-consuming, multiple-step processes, higher consumption and waste of unreacted material, poor control overreaction and overall process performance) offering, on the other hand, the possibility to customize the nanovectors by tuning the process parameters. In fact, microfluidic parameters can be handled to control not only the nanoparticles' size but also their morphologies and physicochemical properties, potentially dictate their biological fate.

Preliminary data on the simultaneous encapsulation of both a gadolinium-based CA for MRI and a dye (ATTO488) for Optical Imaging have been also showed, suggesting the potential use of these hybrid nanocarriers in the multimodal imaging field.

1.6 References

1. Anbazhagan, R.; Muthusamy, G.; Krishnamoorthi, R.; Kumaresan, S.; Rajendra Prasad, N.; Lai, J.Y.; Yang, J.M.; Tsai, H.C. PAMAM G4.5 dendrimers for targeted delivery of ferulic acid and paclitaxel to overcome P-glycoprotein-mediated multidrug resistance. *Biotechnol. Bioeng.* **2021**, *118*, 1213-1223.
2. Azzawi, M.; Seifalian, A.; Ahmed, W. Nanotechnology for the diagnosis and treatment of diseases. *Nanomedicine (Lond)* **2016**, *11*, 2025-2027.
3. Karponis, D.; Azzawi, M.; Seifalian, A. An arsenal of magnetic nanoparticles; perspectives in the treatment of cancer. *Nanomedicine (Lond)* **2016**, *11*, 2215-2232.
4. Patel, T.; Zhou, J.; Piepmeier, J.M.; Saltzman, W.M. Polymeric nanoparticles for drug delivery to the central nervous system. *Adv Drug Deliv Rev* . **2012**, *64*, 701-705.
5. Abulateefeh, S.R.; Spain, S.G.; Thurecht, K.J.; Aylott, J.W.; Chan, W.C.; Garnett, M.C.; Alexander, C. Enhanced uptake of nanoparticle drug carriers via a thermoresponsive shell enhances cytotoxicity in a cancer cell line. *Biomater. Sci.* **2013**, *1*, 434-442.
6. Schomann, T.; Mezzanotte, L.; Lourens, I.M.; de Groot, J.C.; Frijns, J.H.; Huisman, M.A. Lentiviral transduction and subsequent loading with nanoparticles do not affect cell viability and proliferation in hair-follicle-bulge-derived stem cells in vitro. *Contrast Media Mol Imaging* . **2016**, *11*, 550-560.
7. Zhong, Y.; Meng, F.; Deng, C.; Zhong, Z. Ligand-directed active tumor-targeting polymeric nanoparticles for cancer chemotherapy. *Biomacromolecules* **2014**, *15*, 1955-1969.
8. Costagliola di Polidoro, A.; Zambito, G.; Haeck, J.; Mezzanotte, L.; Lamfers, M.; Netti, P.A.; Torino, E. Theranostic Design of Angiopep-2 Conjugated Hyaluronic Acid Nanoparticles (Thera-ANG-cHANPs) for Dual Targeting and Boosted Imaging of Glioma Cells. *Cancers* **2021**, *13*, 503.
9. Courant, T.; Roullin, V.G.; Cadiou, C.; Callewaert, M.; Andry, M.C.; Portefaix, C.; Hoeffel, C.; de Goltstein, M.C.; Port, M.; Laurent, S.; et al. Hydrogels incorporating GdDOTA: towards highly efficient dual T1/T2 MRI contrast agents. *Angew Chem Int Ed Engl* **2012**, *51*, 9119-9122.
10. Vecchione, D.; Grimaldi, A.M.; Forte, E.; Bevilacqua, P.; Netti, P.A.; Torino, E. Hybrid Core-Shell (HyCoS) Nanoparticles produced by Complex Coacervation for Multimodal Applications. *Sci. Rep.* **2017**, *7*, 45121.
11. Russo, M.; Bevilacqua, P.; Netti, P.A.; Torino, E. A Microfluidic Platform to design crosslinked Hyaluronic Acid Nanoparticles (cHANPs) for enhanced MRI. *Sci. Rep.* **2016**, *6*, 37906.
12. Costagliola di Polidoro, A.; Grassia, A.; De Sarno, F.; Bevilacqua, P.; Mollo, V.; Romano, E.; Di Taranto, M.D.; Fortunato, G.; Bracale, U.M.; Tramontano, L.; et al. Targeting Nanostrategies for Imaging of Atherosclerosis. *Contrast Media Mol. Imaging* **2021**, *2021*, 6664471.
13. Azzawi, M. Advances in biomaterial design and application for medical intervention. *Nanomedicine (Lond)* **2017**, *12*, 2151-2152.
14. Boccaccini, A.R.; Erol, M.; Stark, W.J.; Mohn, D.; Hong, Z.; Mano, J.F. Polymer/bioactive glass nanocomposites for biomedical applications: A review. *Compos. Sci. Technol.* **2010**, *70*, 1764.
15. De Sarno, F.; Ponsiglione, A.M.; Torino, E. Emerging use of nanoparticles in diagnosis of atherosclerosis disease: A review. *AIP Conf. Proc* **2018**, *1990*, 020021.
16. Majid, A.; Ahmed, W.; Patil-Sen, Y.; Sen, T. Synthesis and Characterisation of Magnetic Nanoparticles in Medicine. In *Micro and Nanomanufacturing Volume II*, Jackson, M.J., Ahmed, W., Eds.; Springer International Publishing: Cham, 2018; pp. 413-442.

17. Patil-Sen, Y.; Torino, E.; De Sarno, F.; Ponsiglione, A.M.; Chhabria, V.; Ahmed, W.; Mercer, T. Biocompatible superparamagnetic core-shell nanoparticles for potential use in hyperthermia-enabled drug release and as an enhanced contrast agent. *Nanotechnology* **2020**, *31*, 375102.
18. Ailincai, D.; Tartau Mititelu, L.; Marin, L. Drug delivery systems based on biocompatible imino-chitosan hydrogels for local anticancer therapy. *Drug Deliv.* **2018**, *25*, 1080-1090.
19. Gupta, R.C.; Lall, R.; Srivastava, A.; Sinha, A. Hyaluronic Acid: Molecular Mechanisms and Therapeutic Trajectory. *Front. Vet. Sci.* **2019**, *6*, 192.
20. Tripodo, G.; Trapani, A.; Torre, M.L.; Giammona, G.; Trapani, G.; Mandracchia, D. Hyaluronic acid and its derivatives in drug delivery and imaging: Recent advances and challenges. *Eur J Pharm Biopharm* **2015**, *97*, 400-416.
21. Olaru, A.M.; Marin, L.; Morariu, S.; Pricope, G.; Pinteala, M.; Tartau-Mititelu, L. Biocompatible chitosan based hydrogels for potential application in local tumour therapy. *Carbohydr Polym* **2018**, *179*, 59-70.
22. Dey, A.; Koli, U.; Dandekar, P.; Jain, R. Investigating behaviour of polymers in nanoparticles of Chitosan Oligosaccharides coated with Hyaluronic Acid. *Polymer* **2016**, *93*, 44-52.
23. Callewaert, M.; Roullin, V.G.; Cadiou, C.; Millart, E.; Van Gulik, L.; Andry, M.C.; Portefaix, C.; Hoeffel, C.; Laurent, S.; Elst, L.V.; et al. Tuning the composition of biocompatible Gd nanohydrogels to achieve hypersensitive dual T1/T2 MRI contrast agents. *J. Mater. Chem. B* **2014**, *2*, 6397-6405.
24. Chen, H.; Qi, B.; Moore, T.; Wang, F.; Colvin, D.C.; Sanjeewa, L.D.; Gore, J.C.; Hwu, S.J.; Mefford, O.T.; Alexis, F.; et al. Multifunctional yolk-in-shell nanoparticles for pH-triggered drug release and imaging. *Small* **2014**, *10*, 3364-3370.
25. Vecchione, D.; Aiello, M.; Cavaliere, C.; Nicolai, E.; Netti, P.A.; Torino, E. Hybrid core shell nanoparticles entrapping Gd-DTPA and (18)F-FDG for simultaneous PET/MRI acquisitions. *Nanomedicine (Lond)* **2017**, *12*, 2223-2231.
26. Torino, E.; Auletta, L.; Vecchione, D.; Orlandella, F.M.; Salvatore, G.; Iaccino, E.; Fiorenza, D.; Grimaldi, A.M.; Sandomenico, A.; Albanese, S.; et al. Multimodal imaging for a theranostic approach in a murine model of B-cell lymphoma with engineered nanoparticles. *Nanomedicine* **2018**, *14*, 483-491.
27. De Sarno, F.; Ponsiglione, A.M.; Grimaldi, A.M.; Netti, P.A.; Torino, E. Effect of crosslinking agent to design nanostructured hyaluronic acid-based hydrogels with improved relaxometric properties. *Carbohydr. Polym .* **2019**, *222*, 114991.
28. De Sarno, F.; Ponsiglione, A.M.; Russo, M.; Grimaldi, A.M.; Forte, E.; Netti, P.A.; Torino, E. Water-Mediated Nanostructures for Enhanced MRI: Impact of Water Dynamics on Relaxometric Properties of Gd-DTPA. *Theranostics* **2019**, *9*, 1809-1824.
29. Ponsiglione, A.M.; Russo, M.; Netti, P.A.; Torino, E. Impact of biopolymer matrices on relaxometric properties of contrast agents. *Interface focus* **2016**, *6*, 20160061-20160061, doi:10.1098/rsfs.2016.0061.
30. Ponsiglione, A.M.; Russo, M.; Torino, E. Glycosaminoglycans and Contrast Agents: The Role of Hyaluronic Acid as MRI Contrast Enhancer. *Biomolecules* **2020**, *10*, doi:10.3390/biom10121612.
31. Russo, M.; Ponsiglione, A.M.; Forte, E.; Netti, P.A.; Torino, E. Hydrodenticity to enhance relaxivity of gadolinium-DTPA within crosslinked hyaluronic acid nanoparticles. *Nanomedicine (Lond.)* **2017**, *12*, 2199-2210.
32. Chittasupho, C.; Posritong, P.; Ariyawong, P. Stability, Cytotoxicity, and Retinal Pigment Epithelial Cell Binding of Hyaluronic Acid-Coated PLGA Nanoparticles Encapsulating Lutein. *AAPS PharmSciTech* **2019**, *20*, 4.
33. Wu, T.; Li, Y.; Lee, D.S. Chitosan-based composite hydrogels for biomedical applications. *Macromol. Res.* **2017**, *25*, 480-488.

34. Wu, F.; Sun, B.; Chu, X.; Zhang, Q.; She, Z.; Song, S.; Zhou, N.; Zhang, J.; Yi, X.; Wu, D.; et al. Hyaluronic Acid-Modified Porous Carbon-Coated Fe3O4 Nanoparticles for Magnetic Resonance Imaging-Guided Photothermal/Chemotherapy of Tumors. *Langmuir* **2019**, *35*, 13135-13144.
35. Al-Qadi, S.; Alatorre-Meda, M.; Martin-Pastor, M.; Taboada, P.; Remuñán-López, C. The role of hyaluronic acid inclusion on the energetics of encapsulation and release of a protein molecule from chitosan-based nanoparticles. *Colloids Surf. B Biointerfaces* **2016**, *141*, 223-232.
36. Chiesa, E.; Dorati, R.; Conti, B.; Modena, T.; Cova, E.; Meloni, F.; Genta, I. Hyaluronic Acid-Decorated Chitosan Nanoparticles for CD44-Targeted Delivery of Everolimus. *Int. J. Mol. Sci.* **2018**, *19*.
37. Chiesa, E.; Greco, A.; Riva, F.; Tosca, E.M.; Dorati, R.; Pisani, S.; Modena, T.; Conti, B.; Genta, I. Staggered Herringbone Microfluid Device for the Manufacturing of Chitosan/TPP Nanoparticles: Systematic Optimization and Preliminary Biological Evaluation. *Int. J. Mol. Sci.* **2019**, *20*.
38. Naskar, S.; Kuotsu, K.; Sharma, S. Chitosan-based nanoparticles as drug delivery systems: a review on two decades of research. *J. Drug Target.* **2019**, *27*, 379-393.
39. Yilmaz, M.D. Layer-by-layer hyaluronic acid/chitosan polyelectrolyte coated mesoporous silica nanoparticles as pH-responsive nanocontainers for optical bleaching of cellulose fabrics. *Carbohydr. Polym.* **2016**, *146*, 174-180.
40. Desai, K.G. Chitosan Nanoparticles Prepared by Ionotropic Gelation: An Overview of Recent Advances. *Crit Rev Ther Drug Carrier Syst .* **2016**, *33*, 107-158.
41. Huang, J.; Ren, J.; Chen, G.; Li, Z.; Liu, Y.; Wang, G.; Wu, X. Tunable sequential drug delivery system based on chitosan/hyaluronic acid hydrogels and PLGA microspheres for management of non-healing infected wounds. *Mater. Sci. Eng. C* **2018**, *89*, 213-222.
42. Lalevée, G.; David, L.; Montembault, A.; Blanchard, K.; Meadows, J.; Malaise, S.; Crépet, A.; Grillo, I.; Morfin, I.; Delair, T.; et al. Highly stretchable hydrogels from complex coacervation of natural polyelectrolytes. *Soft Matter* **2017**, *13*, 6594-6605.
43. Vignesh, S.; Sivashanmugam, A.; Mohandas, A.; Janarthanan, R.; Iyer, S.; Nair, S.V.; Jayakumar, R. Injectable deferoxamine nanoparticles loaded chitosan-hyaluronic acid coacervate hydrogel for therapeutic angiogenesis. *Colloids Surf. B Biointerfaces* **2018**, *161*, 129-138.
44. Unterweger, H.; Tietze, R.; Janko, C.; Zaloga, J.; Lyer, S.; Dürr, S.; Taccardi, N.; Goudouri, O.; Hoppe, A.; Eberbeck, D.; et al. Development and characterization of magnetic iron oxide nanoparticles with a cisplatin-bearing polymer coating for targeted drug delivery. *Int. J. Nanomed.* **2014**, *9*, 3659-3676.
45. Martínez Rivas, C.J.; Tarhini, M.; Badri, W.; Miladi, K.; Greige-Gerges, H.; Nazari, Q.A.; Galindo Rodríguez, S.A.; Román, R.Á.; Fessi, H.; Elaissari, A. Nanoprecipitation process: From encapsulation to drug delivery. *Int. J. Pharm* **2017**, *532*, 66-81.
46. Ahmed, N.; Fessi, H.; Elaissari, A. Theranostic applications of nanoparticles in cancer. *Drug Discov. Today* **2012**, *17*, 928-934.
47. Krishna, K.S.; Li, Y.; Li, S.; Kumar, C.S. Lab-on-a-chip synthesis of inorganic nanomaterials and quantum dots for biomedical applications. *Adv. Drug Deliv. Rev.* **2013**, *65*, 1470-1495.
48. Cejas, C.M.; Maini, L.; Monti, F.; Tabeling, P. Deposition kinetics of bi- and tridisperse colloidal suspensions in microchannels under the van der Waals regime. *Soft Matter* **2019**, *15*, 7438-7447.
49. Hassan, A.A.; Sandre, O.; Cabuil, V.; Tabeling, P. Synthesis of iron oxide nanoparticles in a microfluidic device: preliminary results in a coaxial flow millichannel. *Chem. Commun.* **2008**, 1783-1785, doi:10.1039/B719550H.
50. Luther, S.K.; Braeuer, A. High-pressure microfluidics for the investigation into multi-phase systems using the supercritical fluid extraction of emulsions (SFEE). *J. Supercrit. Fluids* **2012**, *65*, 78-86.

51. Luther, S.K.; Schuster, J.J.; Leipertz, A.; Braeuer, A. Microfluidic investigation into mass transfer in compressible multi-phase systems composed of oil, water and carbon dioxide at elevated pressure. *J. Supercrit. Fluids* **2013**, *84*, 121-131.
52. Maimouni, I.; Cejas, C.M.; Cossy, J.; Tabeling, P.; Russo, M. Microfluidics Mediated Production of Foams for Biomedical Applications. *Micromachines* **2020**, *11*.
53. Torino, E.; Russo, M.; Ponsiglione, A.M. Lab-on-a-chip preparation routes for organic nanomaterials for drug delivery. In *Microfluidics for Pharmaceutical Applications*, Santos, H.A., Liu, D., Zhang, H., Eds.; William Andrew Publishing: 2019; pp. 137-153.
54. Liu, Y.; Yang, G.; Zou, D.; Hui, Y.; Nigam, K.; Middelberg, A.P.J.; Zhao, C. Formulation of Nanoparticles Using Mixing-Induced Nanoprecipitation for Drug Delivery. *Ind. Eng. Chem. Res.* **2020**, *59*, 4134-4149.
55. Capretto, L.; Carugo, D.; Mazzitelli, S.; Nastruzzi, C.; Zhang, X. Microfluidic and lab-on-a-chip preparation routes for organic nanoparticles and vesicular systems for nanomedicine applications. *Adv. Drug Deliv. Rev.* **2013**, *65*, 1496-1532.
56. Ma, J.; Lee, S.M.; Yi, C.; Li, C. Controllable synthesis of functional nanoparticles by microfluidic platforms for biomedical applications – a review. *Lab Chip* **2017**, *17*, 209-226.
57. Nghe, P.; Terriac, E.; Schneider, M.; Li, Z.Z.; Cloitre, M.; Abecassis, B.; Tabeling, P. Microfluidics and complex fluids. *Lab Chip* **2011**, *11*, 788-794.
58. Christensen, A.L.; Lohr, C.; Christensen, S.M.; Stamou, D. Single vesicle biochips for ultra-miniaturized nanoscale fluidics and single molecule bioscience. *Lab Chip* **2013**, *13*, 3613-3625.
59. Huang, F.; Zhu, Z.; Niu, Y.; Zhao, Y.; Si, T.; Xu, R.X. Coaxial oblique interface shearing: tunable generation and sorting of double emulsions for spatial gradient drug release. *Lab Chip* **2020**, *20*, 1249-1258.
60. Kong, L.; Chen, R.; Wang, X.; Zhao, C.; Chen, Q.; Hai, M.; Chen, D.; Yang, Z.; Weitz, D.A. Controlled co-precipitation of biocompatible colorant-loaded nanoparticles by microfluidics for natural color drinks. *Lab Chip* **2019**, *19*, 2089-2095.
61. Salafi, T.; Zeming, K.K.; Zhang, Y. Advancements in microfluidics for nanoparticle separation. *Lab Chip* **2017**, *17*, 11-33.
62. Choi, A.; Seo, K.D.; Kim, D.W.; Kim, B.C.; Kim, D.S. Recent advances in engineering microparticles and their nascent utilization in biomedical delivery and diagnostic applications. *Lab Chip* **2017**, *17*, 591-613.
63. Liu, D.; Zhang, H.; Fontana, F.; Hirvonen, J.T.; Santos, H.A. Microfluidic-assisted fabrication of carriers for controlled drug delivery. *Lab Chip* **2017**, *17*, 1856-1883.
64. Russo, M.; Bevilacqua, P.; Netti, P.A.; Torino, E. Commentary on "A Microfluidic Platform to Design Crosslinked Hyaluronic Acid Nanoparticles (cHANPs) for Enhanced MRI". *Mol. Imaging* **2017**, *16*, 1536012117706237-1536012117706237, doi:10.1177/1536012117706237.
65. Russo, M.; Grimaldi, A.M.; Bevilacqua, P.; Tammaro, O.; Netti, P.A.; Torino, E. PEGylated crosslinked hyaluronic acid nanoparticles designed through a microfluidic platform for nanomedicine. *Nanomedicine (Lond.)* **2017**, *12*, 2211-2222.
66. Forshult, S.E. *Quantitative analysis with pulsed NMR and the CONTIN computer program*; 2004.
67. Tammaro, O.; Costagliola di Polidoro, A.; Romano, E.; Netti, P.A.; Torino, E. A Microfluidic Platform to design Multimodal PEG - crosslinked Hyaluronic Acid Nanoparticles (PEG-cHANPs) for diagnostic applications. *Sci. Rep.* **2020**, *10*, 6028.

68. Bramosanti, M.; Chronopoulou, L.; Grillo, F.; Valletta, A.; Palocci, C. Microfluidic-assisted nanoprecipitation of antiviral-loaded polymeric nanoparticles. *Colloids Surf. A Physicochem Eng Asp* **2017**, *532*, 369-376.
69. Dou, Y.; Wang, B.; Jin, M.; Yu, Y.; Zhou, G.; Shui, L. A review on self-assembly in microfluidic devices. *J. Micromech. Microeng.* **2017**, *27*, 113002.
70. Karnik, R.; Gu, F.; Basto, P.; Cannizzaro, C.; Dean, L.; Kyei-Manu, W.; Langer, R.; Farokhzad, O.C. Microfluidic Platform for Controlled Synthesis of Polymeric Nanoparticles. *Nano Lett.* **2008**, *8*, 2906-2912.
71. Pati, F.; Adhikari, B.; Dhara, S. Development of chitosan–tripolyphosphate fibers through pH dependent ionotropic gelation. *Carbohydr. Res.* **2011**, *346*, 2582-2588.
72. Patil, J.S.; Kamalapur, M.; Marapur, S.; Kadam, D.V. Ionotropic Gelation and Polyelectrolyte Complexation : the Novel Techniques to Design Hydrogel Particulate Sustained , Modulated Drug Delivery System : a Review. 2010.
73. Aktaş, Y.; Andrieux, K.; Alonso, M.J.; Calvo, P.; Gürsoy, R.N.; Couvreur, P.; Çapan, Y. Preparation and in vitro evaluation of chitosan nanoparticles containing a caspase inhibitor. *Int. J. Pharm.* **2005**, *298*, 378-383.
74. Chiesa, E.; Dorati, R.; Pisani, S.; Conti, B.; Bergamini, G.; Modena, T.; Genta, I. The Microfluidic Technique and the Manufacturing of Polysaccharide Nanoparticles. *Pharmaceutics* **2018**, *10*, 267.
75. Majedi, F.S.; Hasani-Sadrabadi, M.M.; Emami, S.H.; Taghipoor, M.; Dashtimoghadam, E.; Bertsch, A.; Moaddel, H.; Renaud, P. Microfluidic synthesis of chitosan-based nanoparticles for fuel cell applications. *Chem. Commun.* **2012**, *48*, 7744-7746.
76. Majedi, F.S.; Hasani-Sadrabadi, M.M.; VanDersarl, J.J.; Mokarram, N.; Hojjati-Emami, S.; Dashtimoghadam, E.; Bonakdar, S.; Shokrgozar, M.A.; Bertsch, A.; Renaud, P. On-Chip Fabrication of Paclitaxel-Loaded Chitosan Nanoparticles for Cancer Therapeutics. *Adv. Funct. Mater.* **2014**, *24*, 432-441.
77. Miladi, K.; Sfar, S.; Fessi, H.; Elaissari, A. Nanoprecipitation Process: From Particle Preparation to In Vivo Applications. In *Polymer Nanoparticles for Nanomedicines: A Guide for their Design, Preparation and Development*, Vauthier, C., Ponchel, G., Eds.; Springer: Cham, 2016; pp. 17-53.
78. Bally, F.; Garg, D.K.; Serra, C.A.; Hoarau, Y.; Anton, N.; Brochon, C.; Parida, D.; Vandamme, T.; Hadziioannou, G. Improved size-tunable preparation of polymeric nanoparticles by microfluidic nanoprecipitation. *Polymer* **2012**, *53*, 5045-5051.
79. Nemati, Y.; Zahedi, P.; Baghdadi, M.; Ramezani, S. Microfluidics combined with ionic gelation method for production of nanoparticles based on thiol-functionalized chitosan to adsorb Hg (II) from aqueous solutions. *J. Environ. Manage.* **2019**, *238*, 166-177.
80. Lee, T.Y.; Choi, T.M.; Shim, T.S.; Frijns, R.A.M.; Kim, S. Microfluidic production of multiple emulsions and functional microcapsules. *Lab Chip* **2016**, *16*, 3415-3440.
81. Pessoa, A.C.S.N.; Sipoli, C.C.; de la Torre, L.G. Effects of diffusion and mixing pattern on microfluidic-assisted synthesis of chitosan/ATP nanoparticles. *Lab Chip* **2017**, *17*, 2281-2293.
82. Zhang, J.; Yan, S.; Yuan, D.; Alici, G.; Nguyen, N.; Ebrahimi Warkiani, M.; Li, W. Fundamentals and applications of inertial microfluidics: a review. *Lab Chip* **2016**, *16*, 10-34.
83. Doiron, A.L.; Chu, K.; Ali, A.; Brannon-Peppas, L. Preparation and initial characterization of biodegradable particles containing gadolinium-DTPA contrast agent for enhanced MRI. *Proc. Natl. Acad. Sci. U.S.A.* **2008**, *105*, 17232-17237.

CHAPTER II – A HIGH-THROUGHPUT MICROFLUIDIC APPROACH TO DESIGN IODINE-BASED PLGA NANOPARTICLES FOR CT ANGIOGRAPHY

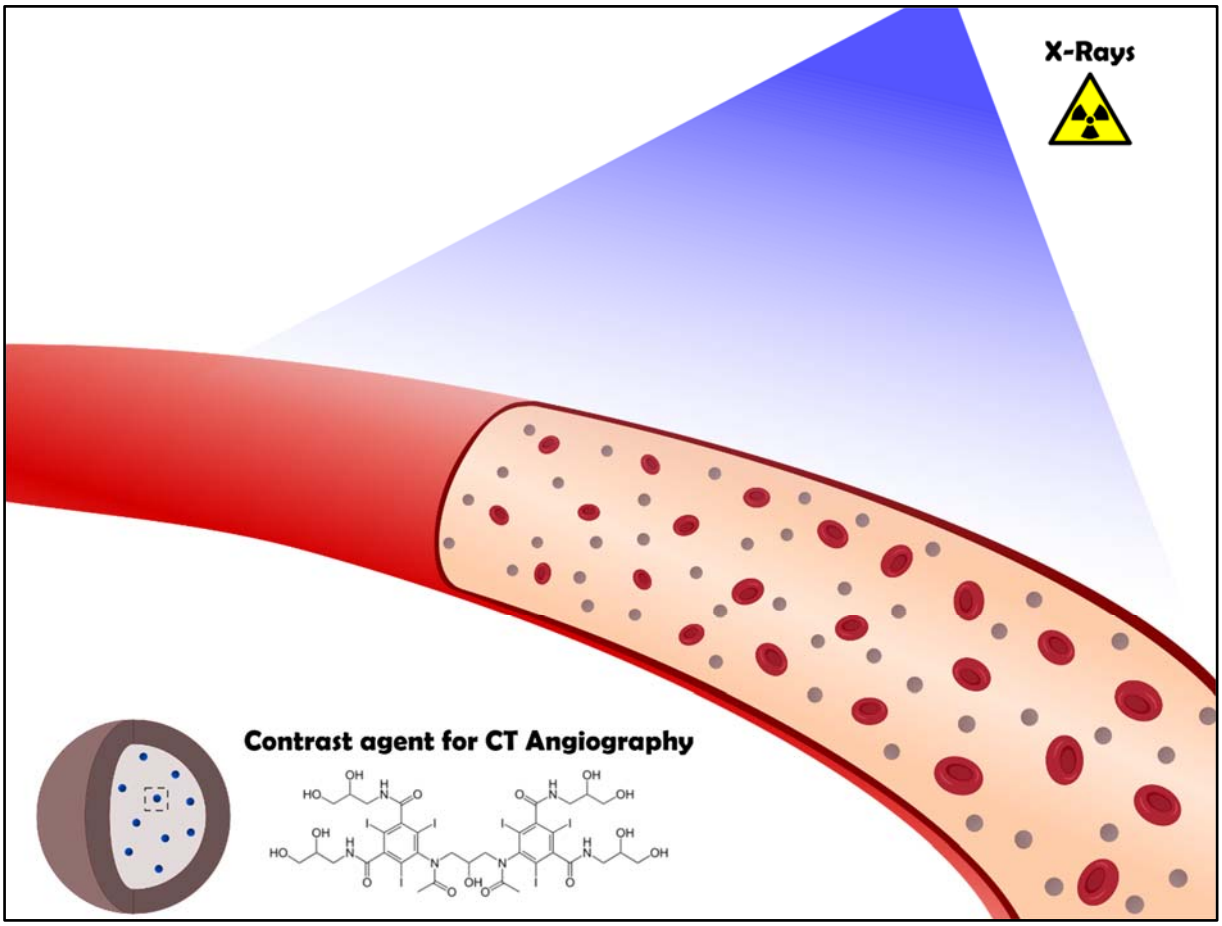

Abstract

CT angiography is an imaging technique that returns an excellent visualization of blood vessels for the detection of vasculature pathologies thanks to the injection of contrast media. In last years, iodine-based contrast media have been increasingly used since they are a good compromise among X-ray attenuation performances, biocompatibility and cost. Although their chemical formulations have been improved for a longer circulation time and a better biocompatibility, iodinated contrast media still exhibit rapid renal clearance and induce side effects in many patients. Here, Iodixanol, a clinically approved iodinated contrast medium for angiography, and poly-lactic-co-glycolic acid (PLGA) have been combined to produce nanocarriers with properties of high biocompatibility and, potentially, long circulation time. An innovative high-throughput microfluidic platform has been designed and optimized to obtain a high yield of monodisperse PLGA nanoparticles by exploiting

the physical principles of nanoprecipitation. The fluorophore ATTO633 has been then utilized to preliminarily evaluate the potential encapsulation efficiency of nanocarriers, even in combination with Gd-DTPA, an MRI contrast agent, to prove the multimodal imaging ability of the nanovector. Finally, a clinically relevant amount of Iodixanol has been encapsulated within nanoparticles and a comparison with the free contrast agent has been provided by the CT attenuation and cytotoxicity point of view in order to highlight the impact of the polymer matrix.

2.1 Introduction

Nowadays, Computed Tomography (CT) is the widest used imaging technique for its ability to provide anatomic details with high resolution at low cost. It is commonly used to visualize vessels, tissues e organs providing information of diagnostic relevance. Thanks to its high temporal resolution, it is also able to quickly catch the cardiac motion. Moreover, the ongoing development of novel hybrid imaging modalities such as PET/CT and SPECT/CT, able to combine anatomical and functional information, is another plus point.

Among several CT applications, CT angiography (CTA) is widely used as an effective and non-invasive technique that enable the anatomic visualization of vessels status. In particular, it can provide essential information to diagnose pulmonary embolism or atherosclerotic stenosis in coronary arteries [1-3]. In this latter case, it has the advantage to allow the study of the morphology, composition and degree of inflammation of coronary atherosclerotic plaques in order to provide clinical indications and identify the risk for the patient [4-6]. Therefore, this is a dynamic process where the injection of a contrast medium (CM) is needed to opacify the bloodstream and evaluate possible deviations or temporal alteration during its passage. In addition to patient related components such as body weight and cardiac output, key factors to determine the CM pharmacokinetics and the consequent enhancement are volume, concentration, injection duration and rate [7-9]. However, while these parameters can be tuned to define the proper protocol, the physicochemical properties of the CM are not arbitrary and so the choice of the optimal one is fundamental. For this reason, it is important to understand how CM works, its properties and its related side effects.

Since the CT is based on the interaction of X-rays with matter and the conversion of detected attenuation coefficients in Hounsfield units (HU), it is difficult to distinguish tissues with similar HU numbers, in particular soft ones [10,11]. For this reason, contrast agents are used to highlight the region of interest increasing the X-rays attenuation in that area. Because the attenuation is

proportional to the third power of the atomic number of the material, the choice is limited to elements with high atomic number [11]. Iodine represents a good compromise between high atomic number (Z=53), biocompatibility and cost compared to metals [10]. In fact, thyroid glands absorb nearly all of the iodine in the body to produce hormones, triiodothyronine (T_3) and thyroxine (T_4) , involved in metabolic, cardiovascular and developmental processes [12,13]. Since a high iodine concentration is needed for successful imaging, more precisely in the millimolar range, a high ratio of iodine atoms per CM molecule is needed. For this reason, iodinated contrast media are usually chemical modifications of a triiodinated benzene ring, with iodine atoms in position 2, 4 and 6 [11,14]. Functional groups such as carboxylic acids and amines are linked to the iodinated aromatic ring to increase biocompatibility and water solubility [11]. Based on the modifications of the organic molecules, different physical properties can be obtained influencing the ionicity, osmolality and viscosity of the CM [15]. Two main distinctions are made to classify CM: ionic or non-ionic and monomer or dimer [11,14-16]. In the first case, non-ionic CM are preferred since the *in vivo* interaction of ionic compounds with anionic and cationic molecules can lead to break up the CM, increasing osmolality. On other side, dimeric CM are able to deliver a higher amount of iodine atoms per molecule. Therefore, non-ionic dimers are the ideal contrast media as they deliver a great amount of iodine with the smaller effect on osmolality [16]. Another classification is made comparing the osmolality of the CM with the plasma one: high-osmolar (HOCM, higher than 1200mOsm/kg), low-osmolar (LOCM, 600 to 800mOsm/kg), and iso-osmolar (IOCM, 290mOsm/kg that is plasma osmolality) contrast medium [16,17]. They are almost eliminated through kidneys where the CM concentration grows leading to its possible dysfunction. In fact, among different adverse reactions following iodinated CM administration such as allergic or cutaneous ones, kidney failure remains the main side effect that can lead to severe consequences [14]. In particular, Contrast-Induced Nephropathy (CIN) or Contrast-Induced Acute Kidney Injury (CIAKI) is defined as an acute renal failure occurring within 24–72 hours after the injection of iodinated radiographic contrast media, whether intravenous or intra-arterial injected , that cannot be attributed to other causes [14,16,18,19]. The risk of CIAKI surely depends on the volume of injected CM, the number and rate of injections and the route of administration. For example, the incidence of CIAKI is higher when the CM is given intraarterially (IA) compared to intravenously (IV) due to the higher dose typically used and the proximity to renal arteries [15]. Indeed, patients undergone coronary angiography have the highest probability to develop AKI as they usually show one or more comorbidities [15,16]. Other factors that can increase the possibility of CIAKI are diabetes, pre-existing renal dysfunction, hypertension,

the use of anti-inflammatory and/or nephrotoxic drugs and dehydration [14,16,17,19]. In order to fully understand pathophysiological mechanisms behind CIAKI development, animal and *in vitro* studies can help to highlight factors that influence renal hemodynamics and possible tissue damages [15,19]. After the injection of the CM in the bloodstream, whether IA or IV, it is considerably diluted before reaching the kidney and, consequently, its osmolality and viscosity is reduced [19]. CM molecules are able to easily overcome the glomerular filter so that their concentration in primary urine is equal to blood plasma one [16,19]. However, along renal tubules, most of the water, driven by osmotic gradients, is reabsorbed causing a considerable increase in CM concentration [18,19]. Consequently, the tubular fluid osmolality and viscosity grows disproportionately (the relationship between concentration and viscosity is exponential) [16,18]. According to the Poiseuille law, since the resistance increases proportionally to fluid viscosity, the fluid flow rate decreases for a given pressure gradient [18,19]. Considering the length and narrow diameter of renal tubules, the high tubular fluid viscosity increases intratubular pressure reducing glomerular filtration rate and leads to extrarenal vessels vasoconstriction [16,19]. The main consequence is renal medulla hypoxia and hypoperfusion that is part of a flow of events that involve cellular damage, oxidative stress and vasoconstriction [19]. It is important to clarify that oxygen delivery, in particular to the outer renal part that is farthest from the descending *vasa recta*, is poor even under normal physiologic conditions [14,18,19]. The break of the balance between oxygen supply and its consumption induced by the CM makes more severe the medullary hypoxia [16]. In fact, this latter lead to the formation of reactive oxygen species (ROS) while a reduction of the vasodilator nitric oxide (NO) production and an increase of the response to vasoconstrictor angiotensin II is induced [14,16,18]. The decrease in NO is due to two reasons: (a) ROS interact with NO and lead to the formation of more powerful oxidant peroxynitrite that is more detrimental [14,16,18]; (b) the loss of endothelial cell viability due to CM [18]. In fact, endothelial cells are the first to come in contact with the contrast agents that exert a direct cytotoxic effect mainly due to the release of free iodine and leads to cell apoptosis and death [14,16,18,19]. Contrast media properties such as ionicity and viscosity and patient pathophysiological conditions such as diabetes influence the entity of the damage [16]. In addition, ROS contribute to cause endothelial cells injury and the produced damage may also release endothelin leading to vasoconstriction and makes the hypoxia worse [14,16,18].

Another organ that can be affected by the injection of the CM is the thyroid. World Health Organization recommends a daily iodine dose of 150 μg (for nonpregnant and adult human beings), whereas iodinated CM contain iodine amount by far higher than recommended [20]. In particular,

when an exposure to high amount of iodine occurs (*i.e.* contrast medium injection), a reduction in thyroid hormones production can be observed (Wolff-Chaikoff effect) [21]. For most individuals this phenomenon is only transient, and the recovery completes in less than 10 days after CM injection. Anyway, some vulnerable patients might not recover from this effect, getting an iodine-induced hypothyroidism [21]. Some cases of Iodine-induced hyperthyroidism have also been reported, especially in those patients with risk factors including nontoxic or diffuse nodular goiter, latent Grave disease and long-standing iodine deficiency [21]. While the outbreak of such metabolic disorders is clearly ascribable to the impact of iodine, to date the biological phenomenology related to their triggering remains not completely understood.

Among all iodinated CM, Iodixanol maybe represents the best choice for its physicochemical properties [22]. Iodixanol (Visipaque®, Chemical formula: $C_{35}H_{44}I_6N_6O_{15}$) is a dimeric iso-osmolal non-ionic hydrophilic contrast medium (iodine content 49.1%, M_W: 1550.20) [23,24]. It is provided in solution where iodine concentration is 270 or 320 mg per ml that means, considering the whole Iodixanol molecule, 550 or 625 mg per ml, respectively [23]. Since Iodixanol is hypotonic to blood, sodium and calcium chloride are added to obtain an injectable isotonic solution (at 37 °C osmolality: 290 mOsm/kg water, viscosity 11.4 mPa*s, density: 1.303 g/ml) [24]. Visipaque® is used for several diagnostic techniques such as angiocardiography, peripheral arteriography (both conventional radiography and digital subtraction angiography), cerebral arteriography, contrast-enhanced computed tomography of the head and body, etc [23,25,26]. Approximately 80 % of the administered dose is excreted unmetabolized through glomerular filtration within 4 hours after intravenous injection [24]. Thanks to its physical properties, the diagnostic efficacy is similar to other iodinated CAs but a lower toxicity has been observed. This latter is mainly related to the iodinated molecule and its hydrophilic behaviour in addition to the cation content of the injectable formulation that led to chemotoxic effects. In fact, pharmacodynamic studies indicate that Iodixanol has fewer cardiovascular effects, causes less renal damage and is associated with similar or smaller changes to the blood-brain barrier and neurological function when compared with non-dimeric non-ionic contrast media [23-28]. A crucial limitation is the rapid clearance through kidneys due to their relatively small size that allow only short imaging times in addition to a non-specific biodistribution [11,24]. The solution to overcome these problems can be found in the development of the so-called "blood pool contrast agents"[29]. The latter can be mainly classified as organic (lipidic or polymeric) or inorganic nanocarriers [10,11,29-31]. In 1999, Torchilin and al. formulated micelles with an iodinated hydrophobic core: methoxypoly(ethylene glycol) (hydrophilic) and poly(ε,N-

(triiodiobenzoyl))-L-lysine (hydrophobic) have been used to prepare an amphiphilic molecules (MPEGiodolysine) that assembled into micellar structures with a size around 80 nm and iodine content of 33.8%. They observed that, after intravenous injection in rats (170 mg I/kg BW), the micellar agent produced an enhancement in the visualization of aorta and heart sustained up to 3 hours after dose injection [32]. Trubetskoy et al. reached an even better result by using same micelles: with an injection dose of 250 mg I/Kg BW in rabbits the visualization of the vasculature was sustained up to 24 [33]. Beside the formulation of micelles, other researchers report the production of liposomes for CM encapsulation. In fact, Mukundan at al. formulated Iodixanol-loaded liposomes, and used polyethylene glycol (PEG) to modify their surface, bringing stealth properties to nanocarriers. They successfully encapsulated up to 105 mg I/ml, which allowed performing very accurate images of the heart vasculature in mice up to two hours [34]. In addition, many works are dedicated to inorganic compounds such as gold nanoparticles because of its good X-ray attenuation behaviour (2.7 times higher than iodine) and its simple surface modification with polymer (e.g. PEG) for a prolongation of their permanence in the blood [30]. A commercially available example is "ExiTron Nano", that consists in an injectable solution of PEGylated alkaline rare earth inorganic nanoparticles sizing around 110 nm. It is widely used for microCT imaging on animals, and particularly in mice it offers a good blood contrast imaging with a half-life up to 3 hours [35]. Recently, an interesting work has been proposed by Hainfeld et al. in which they propose a PEGylated iodine nanoparticles (INPs) contrast agent with a hydraulic diameter of 20 nm. These INPs have the ability of staying in the blood flow up to 40 hours and being 50% cleared from the liver in six months in mice. Also, a good tolerance (4 g I/kg BW) was shown after intravenous injection [36].

As it can be understood from literature, both organic and inorganic nanocarriers can undergo size and surface modifications in order to increase the circulation time in the bloodstream. Firstly, a sufficiently high size prevents glomerular filtration and/or their diffusion through the vascular endothelium. However, on the other side, a size higher than 200 nm induce a rapid uptake by the reticuloendothelial system (RES) and, consequently, their elimination from the bloodstream [30]. Secondly, surface modifications allow to delay the recognition and the subsequent opsonization leading to long-circulation properties. Another advantage of these nanovectors is their ability to simultaneously encapsulate drugs and contrast agents, allowing their usage in multimodal and/or theranostic applications [37,38]. All the reported works bring a strong amelioration to CM circulation time, making possible the visualization of blood vessels even hours after the injection. However,

neither organic nor inorganic nanovectors are intended to face the problem of metabolic thyroid disorders or nephrotoxicity. Especially, long circulating inorganic nanoparticles are mainly obtained by assembling single molecules of CM. Consequently, the body tissues are exposed to these molecules and to potential toxicity. On the other hand, organic micelles could suffer from instability in blood, since, once injected, they experience a strong dilution and their whole structure could undergo cleavage [29]. Although micelles and liposomes could exhibit an instability or leaky behaviour in bloodstream, organic nanovectors seem to be promising, since they can incorporate iodinated molecules. In other words, they provide a protecting cage to it, thus preventing the tissues from CM exposition. Furthermore, among all works reporting the formulation of organic carriers, polymeric nanocarriers have been scarcely tested for long circulation in bloodstream. Lastly, no authors report the test of biopolymeric nanoparticles as carrier for iodinated CM throughout the blood circulation.

Among several nanocarriers, PLGA is one of the most known copolymers having a great suitability to be used as nanocarrier to deliver drugs throughout the body [39,40]. This strong interest in PLGA copolymer is due to its biocompatibility, mechanical properties, versatility and loading capability [39-43]. Several strategies are available to prepare PLGA nanovectors such as double emulsion, coacervation and nanoprecipitation [39,40,43]. In particular, this latter involves the use of two miscible solvents, one in which the solute is dissolved called "solvent" and the other one called "non-solvent"[44]. The mixing of the two phases gives rise to a thermodynamic instability determining the precipitation of polymer as nanoparticles in order to reach the equilibrium through three distinguishable steps: nucleation, growth and aggregation [41,44,45]. However, a precise control on the nanoprecipitation process is required to obtain tunable physical and chemical properties depending on the specific application. From this point of view, microfluidics represents a useful tool to finely control the mixing process through the manipulation of small amounts of fluids thanks to the ensured laminar flow condition ($Re < 100$) [45,46]. Other benefits of the microfluidic technique are a higher encapsulation efficiency, a high throughput and its easy scalability. In particular, the hydrodynamic flow focusing (HFF), implemented in the microfluidic chip, has proven to be suitable to finely control the mixing on a small length scale leading to uniform and small nanoparticles (NPs) [41,45-47]. It can be described as a central stream, composed of the polymeric solution with the possible addition of a drug and/or a contrast agent, squeezed between two adjacent side flows, the so called "non-solvent phase". For example, Karnik et al. produced PLGA-PEG nanoparticles in a flow-focusing geometry by exploiting the physical principle of nanoprecipitation and showing how

the control of the flow rates, the geometrical properties of the chip and the miscibility between the solvent and the non-solvent phase are fundamental to evaluate the mixing time (τ_{mix}) between fluids and so the obtained NPs properties [48].

2.2 Aim of the Chapter II

In this Chapter, the goal is to develop an innovative nanocarrier with long circulating properties encapsulating an iodinated contrast agent. A microfluidic approach is proposed to have a better manipulation of the nanoprecipitation process and, consequently, of the nanoparticle's properties. The loaded nanovector is intended to overcome the limitations of commonly used contrast media by acting on their pharmacokinetics. We aim to demonstrate how the presence of the polymer matrix influences, not only the imaging signal, but also the intrinsic viscosity and the toxicity of the contrast agent. To achieve this purpose, PLGA is chosen for its biocompatibility, mechanical properties, versatility and loading capability. In particular, taking advantage of this latter property, it could be possible to reach the mM amount of contrast medium required for CT analysis. Moreover, acting on the physicochemical properties of the nanovector, it could be possible to lengthen the permanence of the contrast medium in the bloodstream by reducing the renal clearance and consequently the administration dosage. Moreover, the blood flow could be slowed down acting on the viscosity of the solution through a modulation of the local concentration of the nanovector.

2.3 Materials and Methods

2.3.1 Materials

Resomer RG 504H Poly(lactic-co-glycolic) acid 50:50 (45 kDa) has been purchased from Evonik (Essen, Germany) and used to produce nanoparticles. Poly(lactide-co-glycolic)(85:15)-poly(ethylene glycol)-carboxylic acid (5-13 kDa) has been purchased from Sigma Aldrich (St. Louis, MO, USA) to produce micelles. ATTO633 BioReagent (λex: 633 nm; λem: 657 nm; molecular weight: 652 g/mol), suitable for fluorescence has been purchased by Sigma Aldrich (St. Louis, MO, USA). Gd-DTPA (M_W: 547.57 Da; Sigma-Aldrich, St. Louis, MO, USA) has been used to prove the multimodal imaging ability of the nanocarrier. Iodixanol CT-contrast agent (M_W: 1550.18 g/mol; chemical formula: $C_{35}H_{44}I_6N_6O_{15}$) has been bought by Sigma Aldrich (St. Louis, MO, USA) while VISIPAQUE 320 (GE Healthcare, Chicago, IL, USA; bottle of 200 mL; 290 mOsmol/kg water; 26.6 and 11.8 cP at 25 and 37 °respectively; 1.369 and 1.356 g/mL at 25 and 37 °C, respectively) has been kindly gifted by Italian National Research Council - Institute of Clinical Physiology (CNR-IFC). Sodium dodecyl sulfate (SDS Molecular biology grade, HLB=40) has been obtained by AppliChem GmbH (Darmstadt,

Hessen, Germany). Acetone (Carlo Erba Reagents, Milan, Italy ; purity > 99,8%, chemical formula: CH_3COCH_3,) has been used to prepare polymeric solution while Milli-Q water (Milli-Q Plus, Q-POD®, Merck KGaA, Darmstadt, Germany) from the preparation of stock solutions to the dialysis of the sample.

2.3.2 Microfluidic platform

The microfluidic setup has been the same used for the production of CS-HA NPs as described in the previous Chapter. The only differences can be found in the volume syringes (2.5 instead of 5 mL) and the collection method (vial filled with 2 mL of water).

2.3.3 Production of PLGA nanoparticles

Poly(lactide-co-glycolic) acid is a hydrophobic copolymer poorly soluble in water and freely soluble in most of organic solvents. For NPs production, PLGA has been dissolved in acetone and a solubility study has been made to assess its solubility in this solvent. Acetone amount has been added with a step of 1 mL into a beaker containing 25 mg of PLGA. After this assessment, preliminary studies to explore the physical phenomenon of nanoprecipitation within the microfluidic channels at different PLGA concentrations, ranging from 1 to 25 mg/mL, and different flow rates have been performed. In particular, as shown in Figure II-1, the polymer solution has been injected in the middle channel (middle flow rate, MFR) while water in the side ones (side flow rate, SFR).

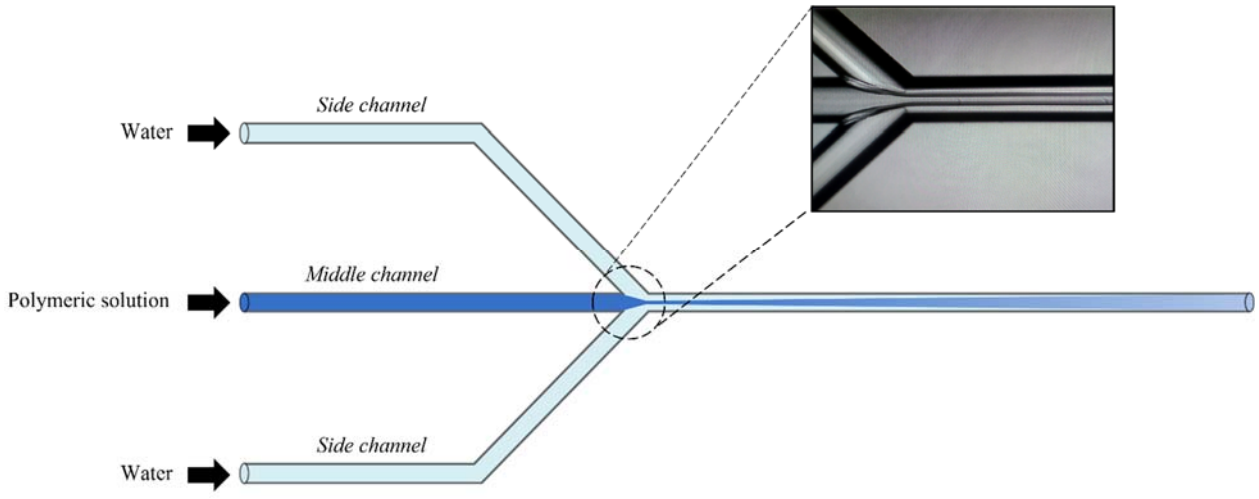

Figure II-1. Representation of the hydrodynamic flow focusing within the chip. Polymer solution is pushed in the middle channel while both side channels are injected with water. An image of the hydrodynamic flow focusing visualized through a stereomicroscope is also provided.

Successively, a feasibility study has been conducted to identify the best process conditions in terms of high throughput and NPs size. Starting from the results obtained in the previous study, PLGA concentrations equal to 1 mg/mL has firstly been tested at different flow rates: SFR ranging from 1 μL/min to 10 μL/min (1; 3; 5; 7; 10 μL/min) and MFR from 1 μL/min to 5 μL/min (1; 2.5; 5 μL/min). In particular, MFR has been fixed at one of listed values and all the combinations with SFR have been tested. After the identification of optimal flow rates conditions at [PLGA]=1 mg/mL, these latter have been performed at other two polymer concentrations, 3 mg/mL and 5 mg/mL.

2.3.4 Production of ATTO633-loaded PLGA nanoparticles

ATTO633 dye has been used to evaluate the potential encapsulation efficiency of PLGA nanoparticles. In particular, keeping constant the PLGA concentration, ATTO633 has been added in the polymer solution at four different concentrations (0.01,0.05,0.1,0.15 mg/mL) according to the previously shown scheme (Figure II-1).

2.3.5 Production of Iodixanol-loaded PLGA nanoparticles

As starting point, a Iodixanol solubility study has been performed keeping the solution in stirring (150 rpm) at the constant temperature of 25 °C. In fact, due to the high hydrophilic behaviour of Iodixanol, its solubility in acetone is really low. For this reason, water has been added stepwise (20 μL at time) to the polymer solution up to the complete Iodixanol solubilization in order to obtain a water-acetone mixture whose ratio is still able to simultaneously solubilize PLGA and Iodixanol. It has been found out that a water content higher than 10 % of the total solvent volume leads to the PLGA precipitation. In particular, an acetone-water ratio equal to 92%-8% allows to solubilize Iodixanol and PLGA up to 2 and 1 mg/mL respectively. However, before introducing Iodixanol in the microfluidic process, the influence of the water in the polymer solution on the nanoprecipitation process and, consequently, on the NPs properties, has been tested. In particular, middle channel has been injected with an acetone (92%) -water (8%) co-solvent at [PLGA] =1 mg/mL according to the result of the above-mentioned solubility study.

The PLGA-Iodixanol stock solution has been obtained as follows: PLGA in acetone (1 mg/mL) and Iodixanol in water (1.57 to 2.15 mg/mL) solutions are prepared separately. Successively, this latter is added dropwise keeping the solution in stirring (150 rpm). A first set of trials have been carried out introducing Iodixanol in the polymer solution as previously described and successively, in order to maximize its content within NPs and reach the minimum required amount to perform CT analysis,

other trials have been performed replacing the water within side channels with a diluted aqueous VISIPAQUE solution (dilution factor: 1:3; Iodixanol content: 217.33 mg/mL).

2.3.6 Nanoparticles morphological characterization

The size distribution and polydispersity index (PDI) of NPs have been analyzed through the Dynamic Light Scattering (DLS) technique (Malvern Panalytical Ltd, Malvern, UK) using 1 mL for each trial. Three measurements, each one of 15 scans, with an equilibration time of 120 s at the fixed temperature of 25 °C, have been carried out on samples.

Moreover, morphology of PLGA NPs has been assessed through Scanning Electron microscope analysis (SEM, Ultraplus Field Emission, Carl Zeiss, Oberkochen, Germany). After collection and dialysis in water, samples are filtered on membrane of 50 nm pore size and then coated with 7 nm Au.

2.3.7 ATTO633 encapsulation efficiency estimation and cellular uptake

To evaluate ATTO633 amount within NPs, Spectrofluorometer analyses (EnSpire Multimode Plate Reader, PerkinElmer Inc, Waltham, MA, USA) have been performed. In particular, the obtained value is then used to compute the NPs encapsulation efficiency as follows:

$$EE(\%) = \frac{Measured\ ATTO633\ concentration}{Theoretical\ ATTO633\ concentration} * 100 \qquad (1)$$

Moreover, the non-loaded NPs suspension, at the same flow rate conditions of ATTO633-loaded one, has been analyzed through the spectrofluorometer as a "blank" to assess how strongly the polymer matrix could interfere during measurements on ATTO633-loaded particles due to a possible screening effect of the polymer nanovector on the encapsulated fluorophore. For this reason, a NPs digestion protocol has been developed. In detail, a proper amount of collection is firstly diluted in acetone to allow the digestion of NPs and, consequently, the release of encapsulated ATTO633 and then in water. Finally, the encapsulation efficiency is computed using the previous formula. A preliminary cellular uptake and localization experiment has also been performed using ATTO633-loaded polymeric NPs. U87 Human glioblastoma tumoral cells have been employed and let in contact with NPs. In detail, cells have been seeded at a density of 5x104 cells/well in 8 slide μ-well glass bottom (IBIDI® GMBH). After 24h, medium supplied with ATTO633-loaded NPs (50 μg/mL) has been added and incubated for 4h. To stain cell nucleus and lysosomes, Hoechst 33342 (0.5 μM) and Lysotracker green (0.1 μM) have been added to the culture medium and incubated for 15 min. Live cells have been observed at Leica Microsystems TCS SP5 Laser Scanning Confocal Microscope (Leica Microsystems, Wetzlar, Germany) equipped with an incubator to keep the

temperature at 37°C and CO_2 levels at 5%, with a 60x oil objective. Hoechst 33342, Lysotracker and ATTO633-loaded NPs have been excited with a 405-diode laser, 488 nm Argon laser and HeNe 633 nm laser, respectively.

2.3.8 Iodixanol encapsulated amount and *in vitro* CT

Varian Cary® 100, 300 UV-Vis spectrophotometer (Agilent Technologies, Santa Clara, CA, USA) has been used to quantify the Iodixanol amount within NPs looking at the characteristic peak of the molecule at 246 nm.

The evaluation of attenuation values has been performed in collaboration with the University Hospital of Pisa. Each sample has been loaded in a 1 mL eppendorf tube and scanned using a multidetector row CT (LightSpeed VCT 64, GE Healthcare, Milwaukee, WI, USA).

2.3.9 ATTO633 and Iodixanol release study

ATTO633 or Iodixanol PLGA NPs have been loaded in a membrane with a cut-off of 10kDa and placed in a graduated cylinder filled with 10 mL of water. The system has been stirred at 300 rpm and 1 mL of the external phase have been collected at established time points up to 24 hours.

2.3.10 Rheological behaviour of Iodixanol-loaded NPs

To evaluate the viscosity of Iodixanol-loaded NPs solution, rheological analysis (TA Instruments, New Castle, DE, USA) has been performed at 25 and 37 °C in a shear rate range from 1 to 1000 s^{-1} using a cone-plate geometry of 25 mm.

2.4 Results

2.4.1 Exploration of the PLGA nanoprecipitation phenomenon in microfluidics

Taken in consideration the really high PLGA solubility in acetone, some preliminary studies on the microfluidic platform have been carried out at polymer concentration of 25 mg/mL and 15 mg/mL. Neither the former nor the latter has been suitable for the microfluidic platform since a strong polymer precipitation causes the microchannels obstruction in a moment. Therefore, other trials have been carried out at lower polymer concentration of 5 mg/mL. Although a blockage of channels does not occur immediately, a strong precipitation is still present at the junction and through the outlet channel. This phenomenon translates in short-lasting trials while longer trials has been finally obtained at PLGA concentration of 1 mg/mL. For this reason, once the polymer concentration has been set at this last value, several flow rates conditions have been explored. All the obtained NPs have shown a very low standard deviation that has been confirmed by SEM analysis (see Figure II-S1 in Appendix B). The trend of particles size can be recognized in the following Figure II-2a.

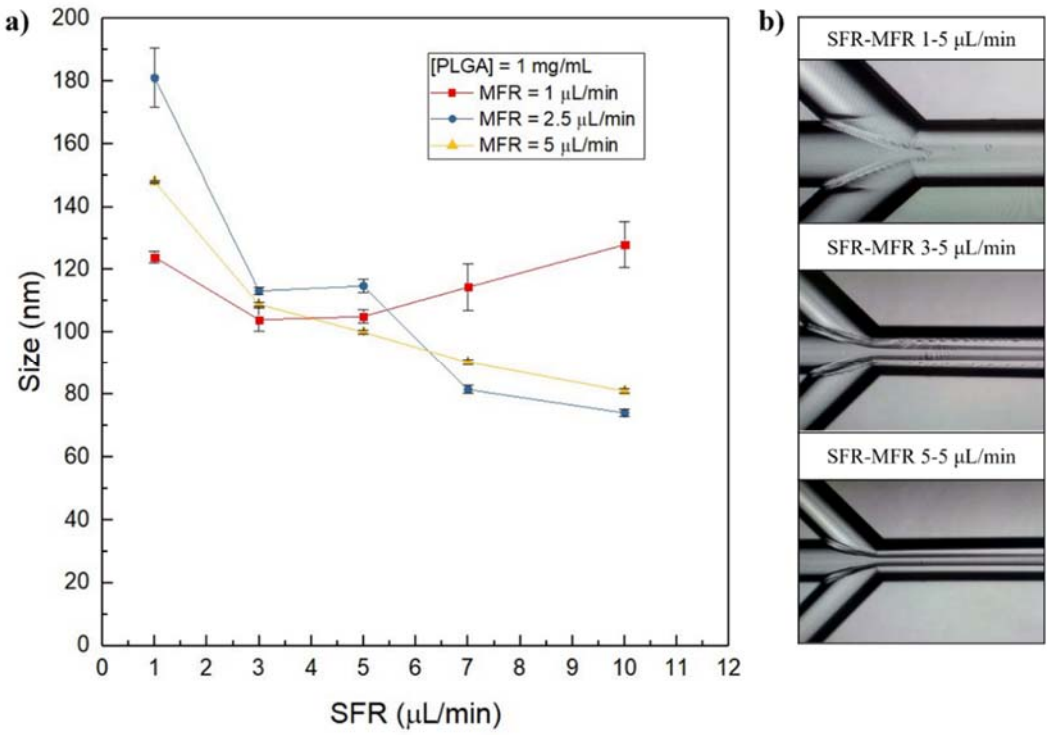

Figure II-2. (a) NPs size trend at three different MFR values and [PLGA]=1 mg/mL when SFR grows; **(b)** hydrodynamic flow focusing images captures through stereomicroscope for: A) SFR-MFR 1-5 μl/min; B) SFR-MFR 3-5 μl/min; C) SFR-MFR 5-5 μl/min

At MFR= 1 μL/min the NPs mean size grows for SFR values higher than 3 μL/min and also the standard deviation becomes wider. At MFR equal to 2.5 and 5 μL/min a decreasing trend is visible with a constant small standard deviation in size for this latter MFR condition. A possible explanation for this different trend can be found in the affinity, miscibility and diffusion rate change between water and acetone which affect the final NPs size. In particular, the motion of the anti-solvent (water) toward the solvent (acetone) and vice versa is influenced by the fluid flow rate within channels. Therefore, for a certain value of MFR, increasing the SFR the mixing between solvent and anti-solvent is faster leading to promote nucleation over growth and agglomeration and resulting is smaller NPs. A visual representation of this phenomenon is visible in Figure II-2b looking at the hydrodynamic flow focusing width and edges. In fact, for example, at value of SFR=1 μL/min, the flow focusing edges are not well visible, because the two SFR are not able to squeeze the MFR and therefore, a no proper mixing happens leading to bigger NPs. Instead, increasing the SFR value, the hydrodynamic flow focusing is narrower with well-defined edges representing the optimal mutual diffusion between water and acetone. Taking into account the result obtained, three flow rates conditions have been identified as optimal in terms of production volume, process duration, flow focusing stability and quality of product in terms of NPs shape and size uniformity: MFR=5 μL/min,

and SFR values of 1,3 and 5 μL/min. Successively, these conditions have been tested with other two higher polymer concentrations, 3 mg/mL and 5 mg/mL in order to highlight the influence of polymer concentration on the nanoprecipitation process . As it is shown in Figure II-3, the polymer concentration results to play a role on NPs dimension: the higher the polymer concentration, the larger the particle size (see Figure II-S2 and II-S3 in Appendix B for SEM analysis and size distribution curves comparison).

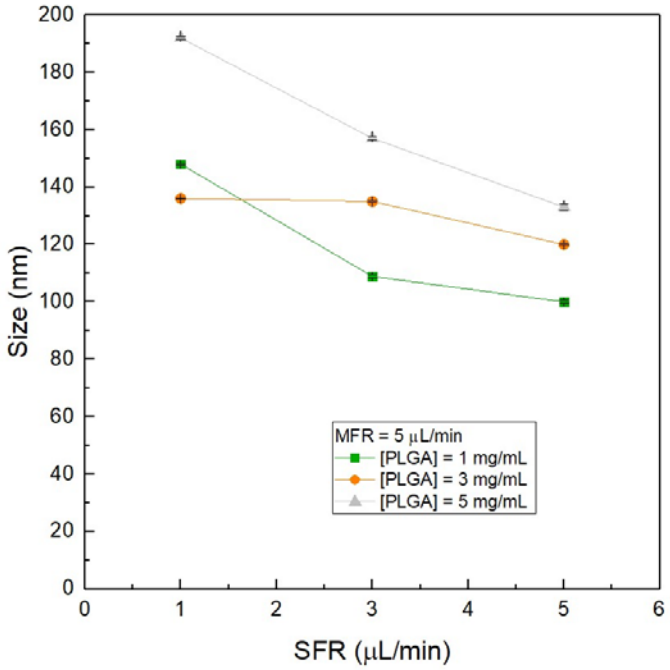

Figure II-3. NPs size trend at three different PLGA concentrations at best conditions SFR-MFR 1-5 μL/min, 3-5 μL/min and 5-5 μL/min. A role of the polymer concentration on NPs size is identified whereas standard deviation still remains low.

Although the high throughput is still present at higher PLGA concentrations, the microfluidic process to produce nanocarriers is more difficult to stabilize and the polymer precipitation results to be more consistent at the junction of chip and outlet channel compared to trials carried out at [PLGA]=1 mg/mL. In fact, the high polymer concentration promotes the collision between nuclei leading to the formation of bigger NPs. Therefore, the PLGA concentration equal to 1 mg/mL has been chosen as gold standard whereas the three optimal SFR-MFR combinations have been also tested in the next implementations of the process before making a decision.

2.4.2 ATTO633 to evaluate PLGA encapsulation efficiency

ATTO633 loaded NPs have been produced with the three best conditions found out in the previous study at [PLGA] = 1 mg/mL. Except for [ATTO633] = 0.01 mg/mL, the ATTO633 encapsulation

efficiency has been evaluated before and after NPs digestion according to the protocol described in the Method section. The variability of the EE depending on the presence of PLGA matrix is shown in Figure II-4.

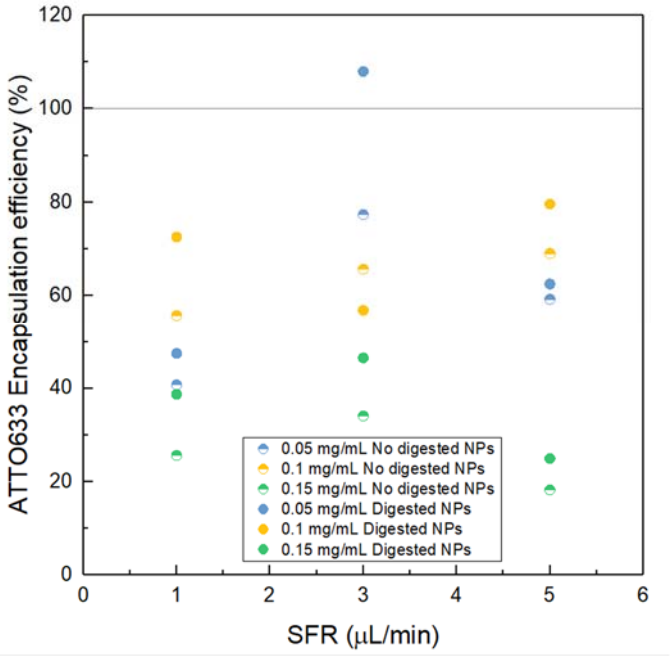

Figure II-4. Encapsulation efficiency values for ATTO633 concentrations of 0.05, 0.1 and 0.15 mg/mL at different SFR (1-3-5 μL/min) and same MFR (5 μL/min) before and after digestion protocol.

For what concern non-digested NPs, the encapsulation efficiency values range from 18 % to 77 %, showing a general trend: the lower the ATTO633 concentration the higher the encapsulation efficiency. Successively, the digestion protocol has been performed to release the encapsulated dye. From Figure II-4, it is possible to notice that digested NPs have encapsulation efficiencies generally higher than those reported in the case of non-digested samples. In addition, the condition [ATTO633] =0.05 mg/mL returns an encapsulation efficiency slightly above the hundred percent (108%), suggesting that something wrong is happened during the measurement or the NPs digestion protocol.

Successively, the ATTO633 release profile from PLGA NPs has been evaluated. In detail, the condition used to perform this study has been the one which previously showed the higher ATTO633 concentration encapsulation efficiency ([ATTO633] =0.05 mg/mL, SFR-MFR 3-5 μL/min). As reported in Figure II-5, after 23h, the 84% of the encapsulated ATTO633 has been released showing an initial burst, probably due to a no well-performed dialysis, followed by a second tract ascribable to the adsorption of the dye on the NPs surface and then the release of the ATTO633.

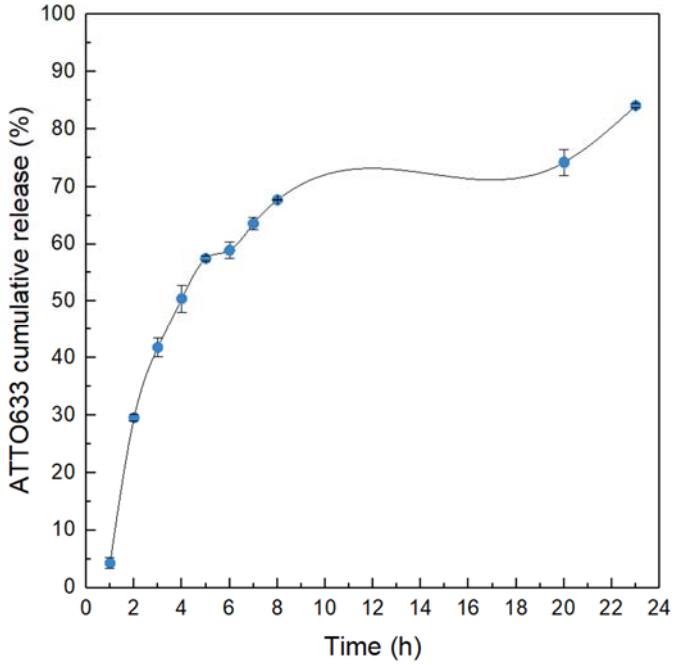

Figure II-5. Release profile of ATTO633 from PLGA NPs

ATTO633-loaded NPs have also been put in contact with human glioblastoma cells to evaluate their internalization. As shown in Figure II-6, it is worth noting that, after 4 hours, NPs enter into the cells but not inside lysosomes, confirming that NPs are still not degraded. In addition, no cell death has been reported proving the nanocarriers safety.

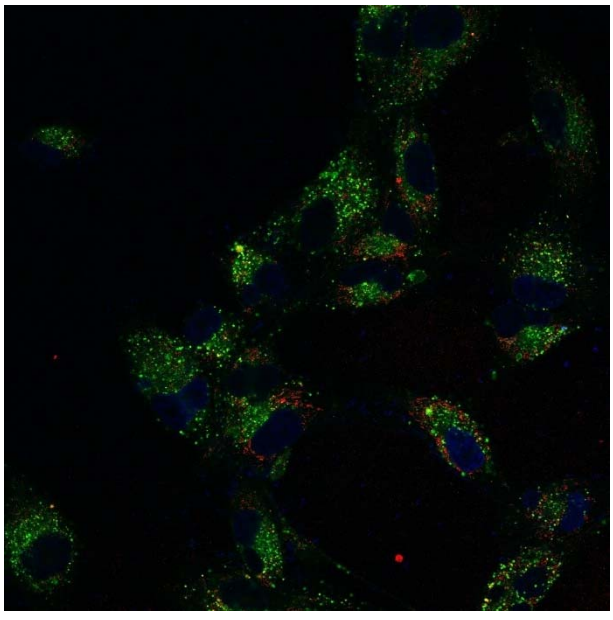

Figure II-6. Live imaging of cellular uptake where the blue, green and red colours correspond to cellular nuclei, lysosome and NPs, respectively.

2.4.3 Multimodal imaging ability of the PLGA nanovector

To understand if the nanocarrier can be potentially used for multimodal imaging applications, water in both side channel has been replaced by a Gd-DTPA aqueous solution of 1 mg /mL. According to the previous results, PLGA nanocarriers show a high encapsulation efficiency: 69% and 58% for ATTO633 and Gd-DTPA, respectively. Furthermore, the *Hydrodenticity* concept, largely explained in Chapter I, has been explored. The loaded gadolinium amount has been evaluated by ICP-MS measurement (see Method section in Chapter I) and then compared to the same concentration of free contrast agent in terms of T_1. In this case, no enhancement in the longitudinal relaxation rate has been obtained, as shown in the following figure, probably due to the hydrophobic behaviour of the polymer that interfere with the water-gadolinium interaction.

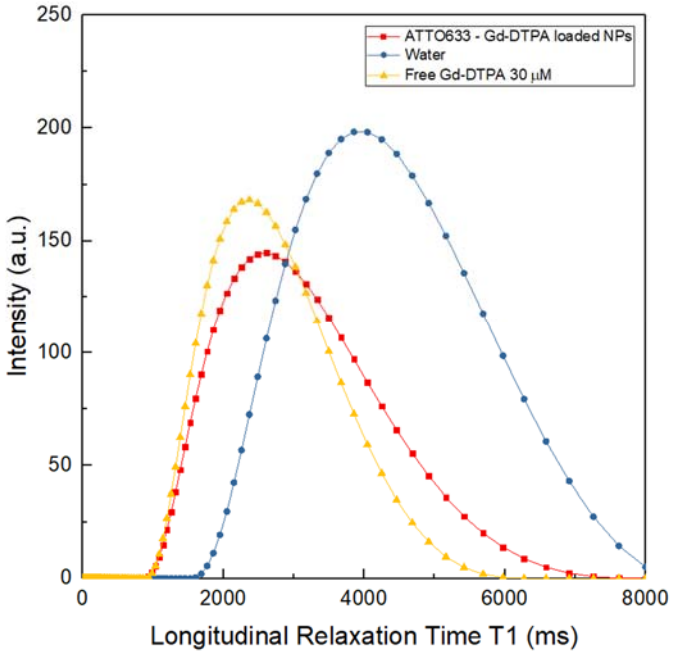

Figure II-7. Relaxation time curves for ATTO633 and Gd-DTPA-loaded NPs in water compared to free water and to the corresponding free Gd-DTPA in water.

2.4.4 Encapsulation of the iodinated contrast agent

As described in the Method section, the acetone 92% - water 8% proportion ensures the Iodixanol solubilization up to almost 2 mg/mL and the PLGA dissolution up to 1 mg/mL. However, the presence of water, although in a small amount, can influence the mutual diffusion of solvent through the nonsolvent phase and vice versa during the microfluidic process. This translates in a different τ_{mix} and particles sizes. Therefore, the water influence has been evaluated by producing PLGA NPs with the above-mentioned acetone-water co-solvent ratio at the SFR-MFR gold standard conditions previously reported. As shown in Figure II-8a, the presence of water slightly influences the

nanoprecipitation process leading to a reduction of NPs size in all three conditions due to a faster mutual diffusion between middle and side streams (shorter τ_{mix}).

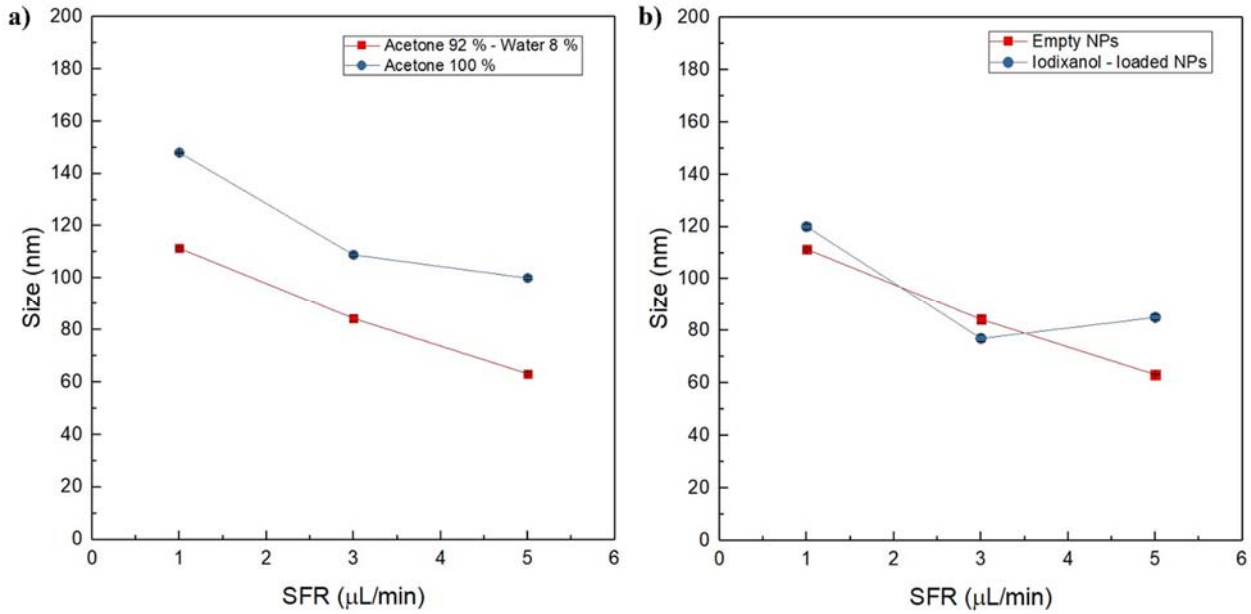

Figure II-8. (a) NPs size trend after the introduction of 10 % water in the solvent compared to 100 % acetone; **(b)** NPs size trend after the introduction of Iodixanol in the process.

After this assessment, best conditions returned from the nanoparticles production feasibility study have been used to produce Iodixanol-loaded PLGA NPs. As shown in Figure II-8b, the presence of Iodixanol, encapsulated or not, slightly affects NPs size at SFR condition equal to 1 and 3 µL/min while a more pronounced difference exists at 5 µL/min (SEM images are reported in Figure II-S4 of

the Appendix B). Moreover, NPs show a high size stability in water at both 25 and 37 °C whether empty or Iodixanol-loaded as illustrated below in Figure II-9.

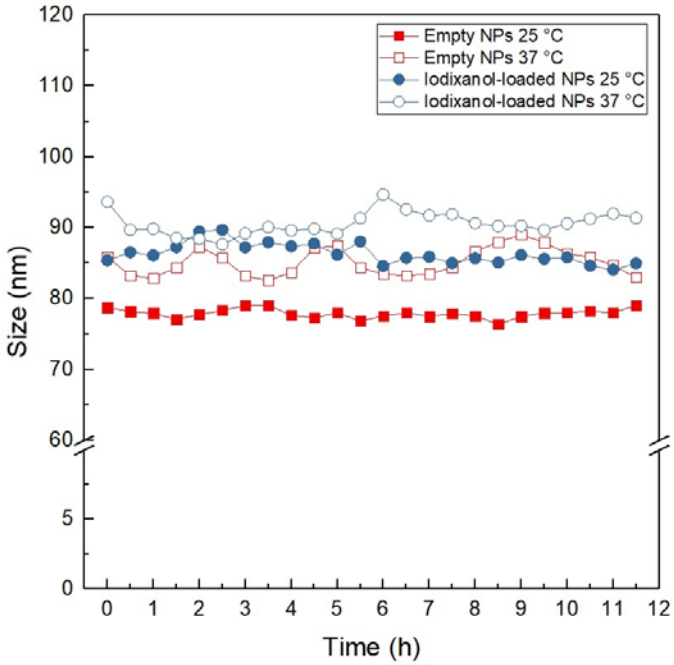

Figure II-9. Empty and Iodixanol-loaded NPs size stability study up to 12h at 25 and 37 °C performed through DLS measurements

Despite the good NPs size and stability, UV-Vis measurements have returned a too much low Iodixanol content to be used in clinical practice. For this reason, the first strategy has been to achieve a higher Iodixanol-loaded NPs concentration. Two different methods have been used to get this result: Optima™ MAX-XP Benchtop Ultracentrifuge (Beckman Coulter, Brea, CA, USA; MLA-80 Fixed Angle Rotor (26 Angle); 50000 rpm, 15 min and 18 °C) and Thermo Scientific™ SL 16R Centrifuge (Thermo Fischer Scientific, Waltham, MA, USA; 7000 rpm, 10 min and 20 °C; Corning® Spin-X® UF 20 mL Centrifugal Concentrator, 50,000 MWCO Membrane). Although both methods have led to comparable results, a value in the range of μg/mL has still been detected.

This means that Iodixanol amount within NPs has to be highly increased in order to reach a clinically relevant CT image contrast. For this reason, taking in consideration the high loading capability of PLGA NPs, the contrast agent concentration in the microfluidic process has been significantly increased replacing water with a diluted VISIPAQUE 320 solution as described in the Method section. No significant differences in the nanoprecipitation process and final NPs size have been detected. A Nanoparticle Tracking Analysis (NanoSight NS300, Malvern Panalytical Ltd, Malvern, UK) has reported a mean size of 70.3 ±1.2 nm and a concentration of $1.33e^{+11}$ ± $1.15e^{+10}$ particles/mL.

Using this strategy, a considerable boost in the encapsulated Iodixanol amount has been achieved reaching concentrations in the range of 15-20 mg/mL, suitable for CT analysis.

At this point, as previously made for ATTO633, the release profile of Iodixanol has been evaluated up to 24 hours as shown in Figure II-10.

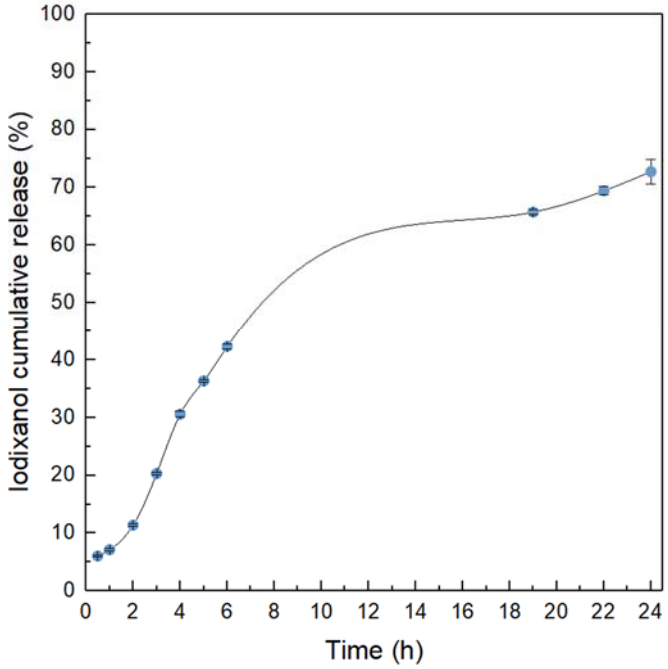

Figure II-10. Iodixanol release profile from PLGA Nps up to 24 hours

As visible in the graph, at 24 hours about 73% of the encapsulated Iodixanol has been released from NPs following a profile that is quite comparable with that of ATTO633. In particular, in both cases, most of the release happens between 2 and 8 hours.

Iodixanol-loaded NPs have been then tested through CT analysis in order to understand how the polymer matrix around the contrast agent can influence its attenuation, expressed in Hounsfield Units (HU). Therefore, to make a comparison with free Iodixanol HU values, a calibration curve has firstly been built up. The HU values have been measured for empty NPs and Iodixanol-loaded NPs at two different concentrations (9 and 18 mg/mL) as shown in Figure II-11.

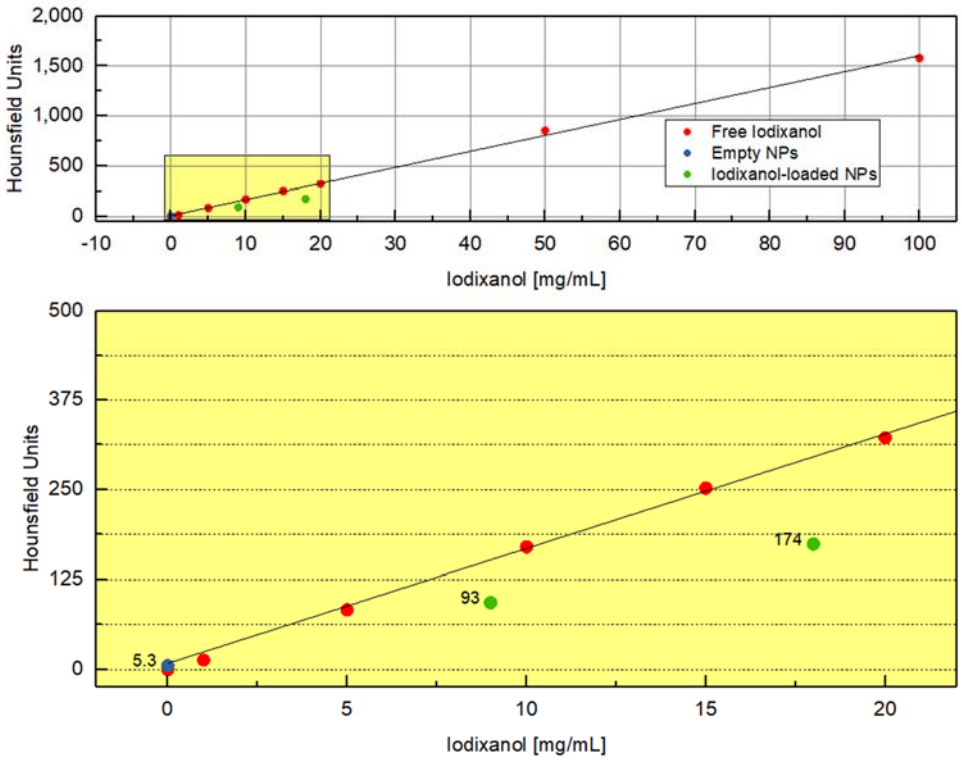

Figure II-11. In vitro evaluation of Iodixanol-loaded NPs attenuation by CT measurements

The HU value of empty NPs has resulted to be higher than water ([Iodixanol]=0 mg/mL) demonstrating that the polymer network acts on the attenuation of X-rays. However, moving to Iodixanol-loaded NPs, results have shown HU values lower than the corresponding free Iodixanol concentrations probably due to the presence of the polymer matrix that hinder the attenuation power of the Iodixanol loaded within NPs.

2.4.4.1 Preliminary *in vitro* toxicity analysis

Successively, an MTT assay has been performed on U87 cells with the aim to compare Iodixanol influence on the cellular activity when it is encapsulated or not within NPs (information about the protocol have been presented in the method section of Chapter I). In details, taking in consideration the iodine that is responsible for attenuation during CT measurements, a high iodine concentration has been tested as reported in Figure II-12. Despite a clear difference between free and loaded Iodixanol has not been found out, the high payload seems to apply a mechanical stress on cells influencing their metabolic activity drastically reducing their growth and reproduction due to the environmental change (see Figure II-S5).

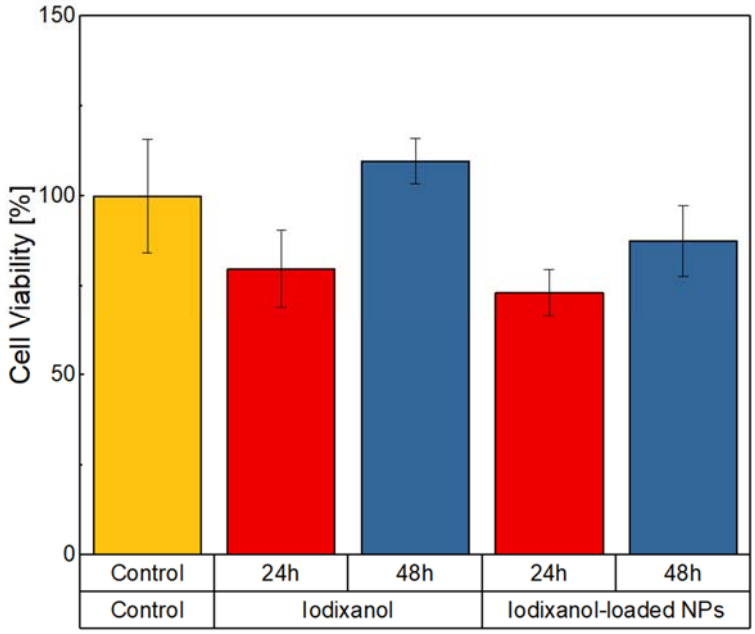

Figure II-12. MTT assay performed to study the cell metabolic activity when put in contact with free and loaded Iodixanol at the concentrations of 7.2 mgI/mL.

2.4.4.2 Preliminary results o*f in vitro* rheological behaviour of Iodixanol-loaded NPs

Blood analogues are emerging as a powerful tool to overcome the ethical, economical and safety issues related to human blood. However, several Newtonian and non-Newtonian models can be found in literature due to the difficulty to exactly mimic the rheological behave of blood [49-52]. The selected analog fluid developed by Carneiro et al. is based on an aqueous solution of 4% SDS (w/w) in which PDMS microparticles of ~7 μm are suspended to simulate the plasma and red blood cells, respectively [51]. Preliminary results show that Iodixanol-loaded NPs, despite the really high concentration, do not lead to an increment of the total viscosity when they are integrated within the SDS solution, even when the concentration of this latter is higher. Instead, it is worth to notice that a synergic effect with free Iodixanol can be recognized.

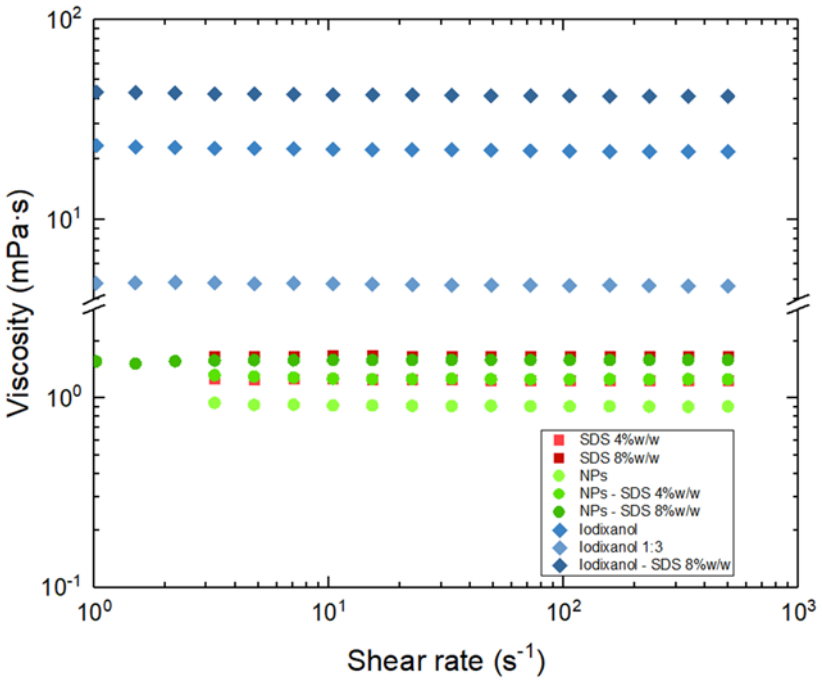

Figure II-13. Rheological measurement of free and loaded Iodixanol in a blood analogue fluid

2.4.5 Preliminary study on PLGA-PEG micelles production

PLGA nanocarriers, due to their hydrophobicity, would be rapidly intercepted by RES as soon as they are injected into the blood flow, determining their elimination by liver and spleen [53,54]. Surface modifications allow to delay the recognition and the subsequent opsonization leading to long-circulation properties. The most common strategy is the PEGylation, namely the surface modification with the hydrophilic polymer poly (ethylene glycol) (PEG) [29,30,55]. In fact, PEG acts by increasing the hydrophilicity of particles, preventing them from the binding of plasma proteins, and by changing their apparent charge (making them neutral). The PEG ability to increase circulation time depends on its incorporated amount and its chains length [29]. Therefore, PEGylation seems to be the easiest and most versatile strategy to achieve a longer circulation time [39,40,42,43,54,56]. To obtain a PLGA-based nanocarrier with a PEG corona, two possible ways can be taken in consideration: in the first case already structured PLGA nanoparticles are chemically modified linking PEG onto the surface while , in the other case, PLGA-PEG block copolymers are used to prepare polymeric micelles made of a PLGA hydrophobic core and a PEG hydrophilic ring[54]. The second choice has been taken in consideration.

PLGA-PEG block copolymer is an amphiphilic polymer with PLGA being strongly hydrophobic and PEG being hydrophilic. For this reason, a solubility study has been carried out to assess the suitable acetone-water ratio to solubilize the copolymer and to be consequently used into the microfluidic process. Firstly, PLGA-PEG has been dissolved in acetone in order to achieve the PLGA block

solubility. Then, water has been added step by step (20 µl at time) until the complete solubilization of PEG part of block copolymer preventing, at the same time, the precipitation of the PLGA. The water percentage able to completely solubilize the PEG portion has been quantified as around 2% of total co-solvent volume. This represents the lower limit of water content in co-solvent composition that solubilizes PLGA-PEG amphiphilic copolymer. Moreover, as the water amount increases, the PLGA part solubility in co-solvent decreases until its precipitation occurs. For this reason, a further investigation has been made to find out the upper limit of water content that still solubilizes the co-polymer, preventing the PLGA precipitation. This value, found out to be 10 %, is identifiable since the solution becomes cloudy due to PLGA insolubility. In other words, the water percentage range in which PLGA-PEG block copolymer is easily solubilized is 2%-10%.

The polymer solution has been dissolved in acetone (94%) and water (6%) co-solvent in order to be in the middle of the previously found range, so avoiding a possible precipitation of one of the two copolymer parts. Several flow rates conditions have been tested included those identified as best ones in the PLGA NPs feasibility study. Although the study needs to be deepened, the production of micelles seems not to be as abundant as for NPs. In Figure II-14, the relationship between flow rate conditions and size variation is summarized. Unlike for the NPs production, the micellization still does not offer a clear size trend.

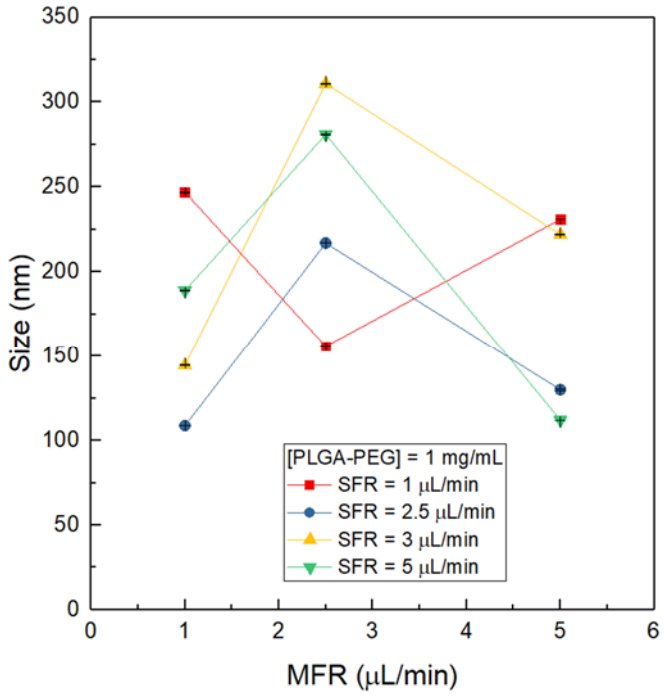

Figure II-14. PLGA-PEG micelles size trend at fixed SFR value and different MFR

2.5 Conclusion

A nanoprecipitation process has been implemented in a custom-made microfluidic platform to produce PLGA nanovectors with the aim to lengthen the delivery of a CT angiography contrast agent in the bloodstream. The effect of flow rates and polymer concentration on the nanoparticles formation has been explored resulting in a high throughput and a great size homogeneity. The well-known high loading capability of PLGA nanovector has been confirmed by the encapsulation of ATTO633 dye, alone or in combination with Gd-DTPA. Finally, Iodixanol has been successfully encapsulated within nanoparticles reaching concentrations in the mg range that are required for *in vivo* clinical use. Furthermore, preliminary data on Iodixanol-loaded NPs cytoxicity, X-rays attenuation and rheological behaviour have been also provided. In particular, for both Iodixanol and ATTO633, the polymer matrix has shown to interfere on the signal intensity if compared to free dye or iodinated contrast agent.

2.6 References

1. Seitun, S.; De Lorenzi, C.; Cademartiri, F.; Buscaglia, A.; Travaglio, N.; Balbi, M.; Bezante, G.P. CT Myocardial Perfusion Imaging: A New Frontier in Cardiac Imaging. *Biomed. Res. Int* . **2018**, *2018*, 7295460.
2. Carità, P.; Guaricci, A.I.; Muscogiuri, G.; Carrabba, N.; Pontone, G. Prognostic Value and Therapeutic Perspectives of Coronary CT Angiography: A Literature Review. *Biomed. Res. Int* . **2018**, *2018*, 6528238.
3. John, G.; Marti, C.; Poletti, P.-A.; Perrier, A. Hemodynamic Indexes Derived from Computed Tomography Angiography to Predict Pulmonary Embolism Related Mortality. *Biomed. Res. Int.* **2014**, *2014*, 363756.
4. Sun, Z.; Xu, L. Coronary CT Angiography in the Quantitative Assessment of Coronary Plaques. *Biomed. Res. Int.* **2014**, *2014*, 346380.
5. Kigka, V.I.; Rigas, G.; Sakellarios, A.; Siogkas, P.; Andrikos, I.O.; Exarchos, T.P.; Loggitsi, D.; Anagnostopoulos, C.D.; Michalis, L.K.; Neglia, D.; et al. 3D reconstruction of coronary arteries and atherosclerotic plaques based on computed tomography angiography images. *Biomed. Signal Process. Control* **2018**, *40*, 286-294.
6. Motoyama, S.; Ito, H.; Sarai, M.; Kondo, T.; Kawai, H.; Nagahara, Y.; Harigaya, H.; Kan, S.; Anno, H.; Takahashi, H.; et al. Plaque Characterization by Coronary Computed Tomography Angiography and the Likelihood of Acute Coronary Events in Mid-Term Follow-Up. *J. Am. Coll. Cardiol* . **2015**, *66*, 337-346.
7. Bae, K.T. Intravenous Contrast Medium Administration and Scan Timing at CT: Considerations and Approaches. *Radiology* **2010**, *256*, 32-61.
8. Bae, K.T.; Heiken, J.P. Scan and contrast administration principles of MDCT. *Eur. Radiol.* **2005**, *15*, e46-e59.
9. Faggioni, L.; Gabelloni, M. Iodine Concentration and Optimization in Computed Tomography Angiography: Current Issues. *Invest. Radiol.* **2016**, *51*, 816-822.

10. Lusic, H.; Grinstaff, M.W. X-ray-computed tomography contrast agents. *Chem. Rev.* **2013**, *113*, 1641-1666.
11. Lee, N.; Choi, S.H.; Hyeon, T. Nano-Sized CT Contrast Agents. *Adv. Mater.* **2013**, *25*, 2641-2660.
12. Spitzweg, C.; Heufelder, A.E.; Morris, J.C. Thyroid Iodine Transport. *Thyroid* **2000**, *10*, 321-330.
13. Smith, J.W.; Evans, A.T.; Costall, B.; Smythe, J.W. Thyroid hormones, brain function and cognition: a brief review. *Neurosci. Biobehav. Rev.* **2002**, *26*, 45-60.
14. Andreucci, M.; Solomon, R.; Tasanarong, A. Side Effects of Radiographic Contrast Media: Pathogenesis, Risk Factors, and Prevention. *Biomed. Res. Int.* **2014**, *2014*, 741018.
15. Solomon, R. Contrast Media: Are There Differences in Nephrotoxicity among Contrast Media? *Biomed. Res. Int.* **2014**, *2014*, 934947.
16. Andreucci, M.; Faga, T.; Pisani, A.; Sabbatini, M.; Russo, D.; Michael, A. The Choice of the Iodinated Radiographic Contrast Media to Prevent Contrast-Induced Nephropathy. *Advances in Nephrology* **2014**, *2014*, 691623.
17. Caiazza, A.; Russo, L.; Sabbatini, M.; Russo, D. Hemodynamic and Tubular Changes Induced by Contrast Media. *Biomed. Res. Int.* **2014**, *2014*, 578974.
18. Andreucci, M.; Faga, T.; Pisani, A.; Sabbatini, M.; Michael, A. Acute Kidney Injury by Radiographic Contrast Media: Pathogenesis and Prevention. *Biomed. Res. Int.* **2014**, *2014*, 362725.
19. Seeliger, E.; Lenhard, D.C.; Persson, P.B. Contrast Media Viscosity versus Osmolality in Kidney Injury: Lessons from Animal Studies. *Biomed. Res. Int.* **2014**, *2014*, 358136.
20. World Health, O. Assessment of iodine deficiency disorders and monitoring their elimination : a guide for programme managers. **2007**.
21. Leung, A.M.; Braverman, L.E. Consequences of excess iodine. *Nat. Rev. Endocrinol .* **2014**, *10*, 136-142.
22. Eivindvik, K.; Sjogren, C.E. Physicochemical properties of iodixanol. *Acta Radiol.* **1995**, *399*, 32-38.
23. Fountaine, H.; Harnish, P.; Andrew, E.; Grynne, B. Safety, tolerance, and pharmacokinetics of iodixanol injection, a nonionic, isosmolar, hexa-iodinated contrast agent. *Acad. Radiol.* **1996**, *3*, S475-S484.
24. Spencer, C.M.; Goa, K.L. Iodixanol. A review of its pharmacodynamic and pharmacokinetic properties and diagnostic use as an x-ray contrast medium. *Drugs* **1996**, *52*, 899-927.
25. Kløw, N.E.; Levorstad, K.; Berg, K.J.; Brodahl, U.; Endresen, K.; Kristoffersen, D.T.; Laake, B.; Simonsen, S.; Tofte, A.J.; Lundby, B. Iodixanol in cardioangiography in patients with coronary artery disease. Tolerability, cardiac and renal effects. *Acta Radiol.* **1993**, *34*, 72-77.
26. Tveit, K.; Bolz, K.D.; Bolstad, B.; Haugland, T.; Berg, K.J.; Skjaerpe, T.; Kloster, Y.F. Iodixanol in cardioangiography. A double-blind parallel comparison between iodixanol 320 mg I/ml and ioxaglate 320 mg I/ml. *Acta Radiol.* **1994**, *35*, 614-618.
27. Erdogan, A.; Davidson, C.J. Recent clinical trials of iodixanol. *Rev. Cardiovasc. Med.* **2003**, *4 Suppl 5*, S43-50.
28. Heinrich, M.C.; Häberle, L.; Müller, V.; Bautz, W.; Uder, M. Nephrotoxicity of Iso-osmolar Iodixanol Compared with Nonionic Low-osmolar Contrast Media: Meta-analysis of Randomized Controlled Trials. *Radiology* **2009**, *250*, 68-86.
29. Hallouard, F.; Anton, N.; Choquet, P.; Constantinesco, A.; Vandamme, T. Iodinated blood pool contrast media for preclinical X-ray imaging applications – A review. *Biomaterials* **2010**, *31*, 6249-6268.
30. Anton, N.; Vandamme, T.F. Nanotechnology for computed tomography: a real potential recently disclosed. *Pharm. Res.* **2014**, *31*, 20-34.
31. Cormode, D.P.; Naha, P.C.; Fayad, Z.A. Nanoparticle contrast agents for computed tomography: a focus on micelles. *Contrast Media Mol. Imaging* **2014**, *9*, 37-52.

32. Torchilin, V.P.; Frank-Kamenetsky Md Fau - Wolf, G.L.; Wolf, G.L. CT visualization of blood pool in rats by using long-circulating, iodine-containing micelles. *Acad. Radiol.* **1999**, *6*, 61-65.
33. Trubetskoy, V.S.; Gazelle Gs Fau - Wolf, G.L.; Wolf Gl Fau - Torchilin, V.P.; Torchilin, V.P. Block-copolymer of polyethylene glycol and polylysine as a carrier of organic iodine: design of long-circulating particulate contrast medium for X-ray computed tomography. *J. Drug Target.* **1997**, *4*, 381-388.
34. Mukundan, S., Jr.; Ghaghada Kb Fau - Badea, C.T.; Badea Ct Fau - Kao, C.-Y.; Kao Cy Fau - Hedlund, L.W.; Hedlund Lw Fau - Provenzale, J.M.; Provenzale Jm Fau - Johnson, G.A.; Johnson Ga Fau - Chen, E.; Chen E Fau - Bellamkonda, R.V.; Bellamkonda Rv Fau - Annapragada, A.; Annapragada, A. A liposomal nanoscale contrast agent for preclinical CT in mice. *AJR Am. J. Roentgenol .* **2006**, *186*, 300-307.
35. Boll, H.; Nittka, S.; Doyon, F.; Neumaier, M.; Marx, A.; Kramer, M.; Groden, C.; Brockmann, M.A. Micro-CT Based Experimental Liver Imaging Using a Nanoparticulate Contrast Agent: A Longitudinal Study in Mice. *PLoS One* **2011**, *6*, e25692.
36. Hainfeld, J.F.; Ridwan, S.M.; Stanishevskiy, Y.; Smilowitz, N.R.; Davis, J.; Smilowitz, H.M. Small, Long Blood Half-Life Iodine Nanoparticle for Vascular and Tumor Imaging. *Sci. Rep.* **2018**, *8*, 13803.
37. Wallyn, J.; Anton, N.; Mertz, D.; Begin-Colin, S.; Perton, F.; Serra, C.A.; Franconi, F.; Lemaire, L.; Chiper, M.; Libouban, H.; et al. Magnetite- and Iodine-Containing Nanoemulsion as a Dual Modal Contrast Agent for X-ray/Magnetic Resonance Imaging. *ACS Appl. Mater. Interfaces* **2019**, *11*, 403-416.
38. Ma, X.; Zhao, Y.; Liang, X.-J. Theranostic Nanoparticles Engineered for Clinic and Pharmaceutics. *Acc. Chem. Res.* **2011**, *44*, 1114-1122.
39. Rezvantalab, S.; Drude, N.I.; Moraveji, M.K.; Güvener, N.; Koons, E.K.; Shi, Y.; Lammers, T.; Kiessling, F. PLGA-Based Nanoparticles in Cancer Treatment. *Front. Pharmacol.* **2018**, *9*, 1260-1260.
40. Essa, D.; Kondiah, P.P.D.; Choonara, Y.E.; Pillay, V. The Design of Poly(lactide-co-glycolide) Nanocarriers for Medical Applications. *Front. Bioeng Biotechnol.* **2020**, *8*, 48.
41. Lababidi, N.; Sigal, V.; Koenneke, A.; Schwarzkopf, K.; Manz, A.; Schneider, M. Microfluidics as tool to prepare size-tunable PLGA nanoparticles with high curcumin encapsulation for efficient mucus penetration. *Beilstein J. Nanotechnol.* **2019**, *10*, 2280-2293.
42. Mir, M.; Ahmed, N.; Rehman, A.u. Recent applications of PLGA based nanostructures in drug delivery. *Colloids Surf. B Biointerfaces* **2017**, *159*, 217-231.
43. Makadia, H.K.; Siegel, S.J. Poly Lactic-co-Glycolic Acid (PLGA) as Biodegradable Controlled Drug Delivery Carrier. *Polymers (Basel)* **2011**, *3*, 1377-1397.
44. Martínez Rivas, C.J.; Tarhini, M.; Badri, W.; Miladi, K.; Greige-Gerges, H.; Nazari, Q.A.; Galindo Rodríguez, S.A.; Román, R.Á.; Fessi, H.; Elaissari, A. Nanoprecipitation process: From encapsulation to drug delivery. *Int. J. Pharm* **2017**, *532*, 66-81.
45. Liu, Y.; Yang, G.; Zou, D.; Hui, Y.; Nigam, K.; Middelberg, A.P.J.; Zhao, C. Formulation of Nanoparticles Using Mixing-Induced Nanoprecipitation for Drug Delivery. *Ind. Eng. Chem. Res.* **2020**, *59*, 4134-4149.
46. Capretto, L.; Cheng, W.; Carugo, D.; Katsamenis, O.L.; Hill, M.; Zhang, X. Mechanism of co-nanoprecipitation of organic actives and block copolymers in a microfluidic environment. *Nanotechnology* **2012**, *23*, 375602.
47. Schneider, T.; Chapman, G.H.; Häfeli, U.O. Effects of chemical and physical parameters in the generation of microspheres by hydrodynamic flow focusing. *Colloids Surf. B Biointerfaces* **2011**, *87*, 361-368.

48. Karnik, R.; Gu, F.; Basto, P.; Cannizzaro, C.; Dean, L.; Kyei-Manu, W.; Langer, R.; Farokhzad, O.C. Microfluidic Platform for Controlled Synthesis of Polymeric Nanoparticles. *Nano Lett.* **2008**, *8*, 2906-2912.
49. Lima, R.; Vega, E.J.; Moita, A.S.; Miranda, J.M.; Pinho, D.; Moreira, A.L.N. Fast, flexible and low-cost multiphase blood analogue for biomedical and energy applications. *Exp. Fluids* **2020**, *61*, 231.
50. Pinho, D.; Muñoz-Sánchez, B.N.; Anes, C.F.; Vega, E.J.; Lima, R. Flexible PDMS microparticles to mimic RBCs in blood particulate analogue fluids. *Mech. Res. Commu.* **2019**, *100*, 103399.
51. Carneiro, J.; Lima, R.; Campos, J.B.L.M.; Miranda, J.M. A microparticle blood analogue suspension matching blood rheology. *Soft Matter* **2021**, *17*, 3963-3974.
52. Completo, C.; Geraldes, V.; Semiao, V. Rheological and dynamical characterization of blood analogue flows in a slit. *Int. J. Heat Fluid Flow* **2014**, *46*, 17-28.
53. Makadia, H.K.; Siegel, S.J. Poly Lactic-co-Glycolic Acid (PLGA) as Biodegradable Controlled Drug Delivery Carrier. *Polymers* **2011**, *3*, 1377-1397, doi:10.3390/polym3031377.
54. Sah, H.; Thoma, L.A.; Desu, H.R.; Sah, E.; Wood, G.C. Concepts and practices used to develop functional PLGA-based nanoparticulate systems. *Int. J. Nanomedicine* **2013**, *8*, 747-765.
55. Hallouard, F.; Briançon S Fau - Anton, N.; Anton N Fau - Li, X.; Li X Fau - Vandamme, T.; Vandamme T Fau - Fessi, H.; Fessi, H. Poly(ethylene glycol)-poly(ε-caprolactone) iodinated nanocapsules as contrast agents for X-ray imaging. *Pharm. Res.* **2013**, *30*, 2020-2035.
56. Kim, D.; El-Shall, H.; Dennis, D.; Morey, T. Interaction of PLGA nanoparticles with human blood constituents. *Colloids Surf. B Biointerfaces* **2005**, *40*, 83-91.

CHAPTER III – THE POTENTIAL OF ARTIFICIAL NEURAL NETWORKS FOR THE OPTIMAL DESIGN OF PARTICLES

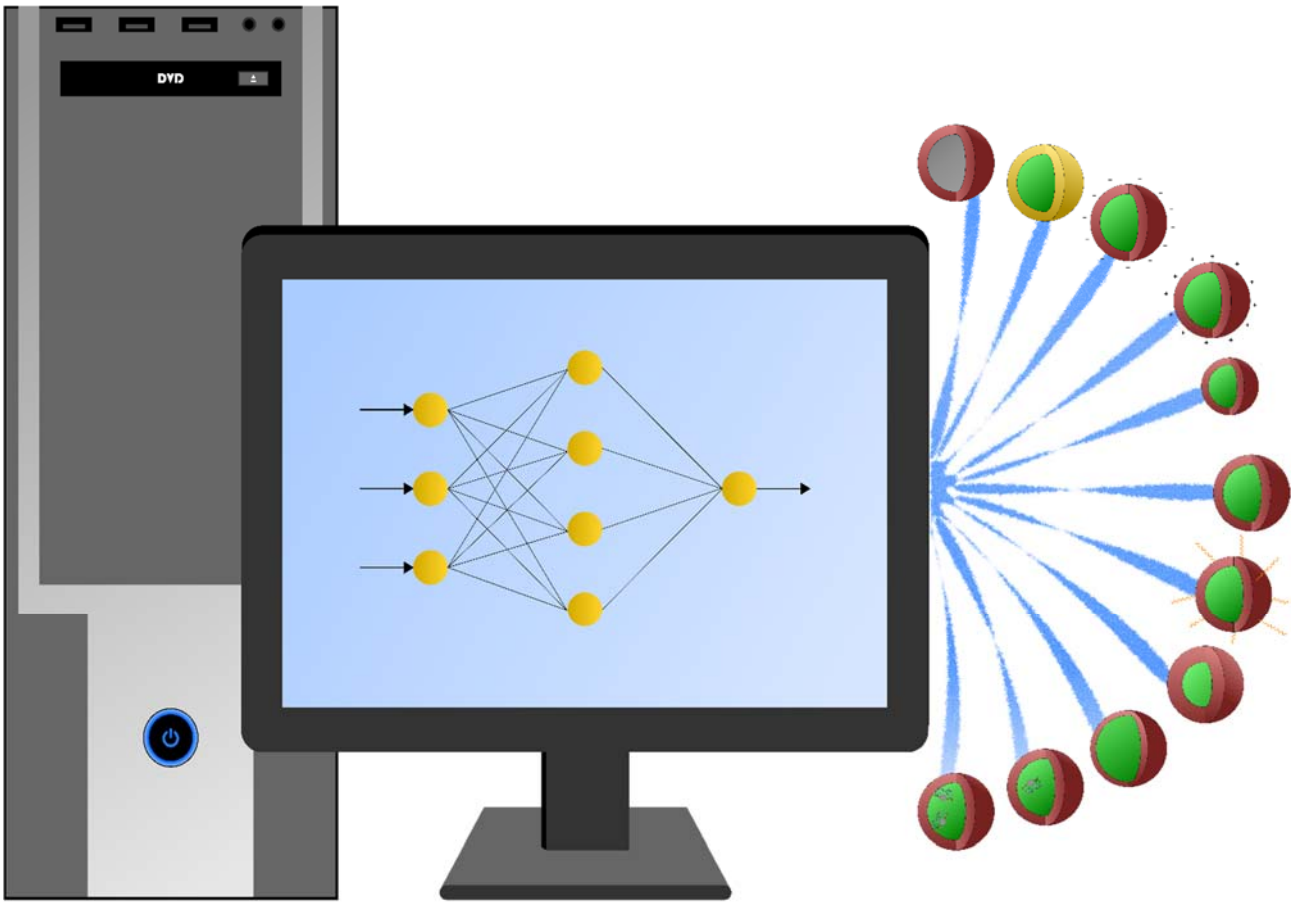

Abstract

The morphological, structural and functional properties of particles play a key role in their *in vivo* fate and therapeutic and/or imaging ability. For this reason, these latter need to be finely designed through the use of more sophisticated production methods, such as microfluidics, that allow to handle process parameters and directly influence the vector properties. However, this is a challenging task to achieve since multiple variables come into play requiring very expensive experimental campaign, in terms of material and time, before reaching the optimal design of the particle. The wide range of applicability of Artificial intelligence (AI) can help to drastically reduce the number of trials leading to understand the input-output relationship of the production process and predict several properties of the particle. Thanks to a supervised learning approach, different Artificial Neural Networks (ANNs) have been trained to predict nanoparticles final size during the microfluidic production of nanoparticles, allowing to give a deep insight of the influence of process

parameters, or to classify the microfluidic regime during the droplet generation of microparticles. Moreover, an additional ANN has been build up to conduct a preliminary study on the interaction between a hyaluronic acid hydrogel and an MRI contrast agent in a bulk system in order to understand how its imaging ability can be influenced by the presence of the polymer matrix.

3.1 Introduction

Artificial intelligence (AI) is an area of computer science concerning with building software capable of carrying out tasks similar to those that the human brain routinely performs [1]. In particular, Artificial Neural Networks (ANNs) learn from experience starting from appropriate examples just as human brain do, without following a set of predefined computational rules. Therefore, ANN architecture is inspired by biological neurons to simulate the way in which they process information [2-4]. In fact, each neuron has many dendrites that carry information into the cell body and an axon which transmits the signal through synapse to the next neuron. The power of the human brain lies in the full interconnection between more than 100 billion neurons which receive and send impulses. Similarly, the ANN is composed by artificial neurons connected among them by coefficients named weights. Each incoming signal is adjusted by multiplying it by the relative weight. Their sum is then passed through a transfer function, typically a sigmoid one, to produce the output for that neuron [2,5,6]. Obviously, the network has at most a few hundred neurons but is able to process extensive amounts of data and make accurate predictions. ANNs differ from each other by their learning rules, by the transfer function and by the connection formula. For example, the absence or presence of feedback connections allows to distinguish between feedforward and feedback networks [2]. In this latter case, the output of each neuron depends on the weighted sum of input signals and also on its previous state. About the learning rules, the most used is the backpropagation in which the weights are continuously adjusted by training the network to map a set of input data until the prediction error, defined as the difference between the predicted and target value, is minimized [7]. In this regard, it is important to provide the network with a sufficient number of training data. In fact, a short training does not allow to reach a certain level of accuracy while, on the other side, if it is too long, the network is overtrained becoming excessively specific for that cluster of data [2,7]. Two are the possible training approach based on the kind of data available and the scope of the study: unsupervised learning and supervised learning [2]. In the first one, the model receives unlabeled data and tries to extract features and patterns on its own. Instead, in the other case, the algorithm

learns from the previous experience in order to help the algorithm to evaluate its accuracy on training data.

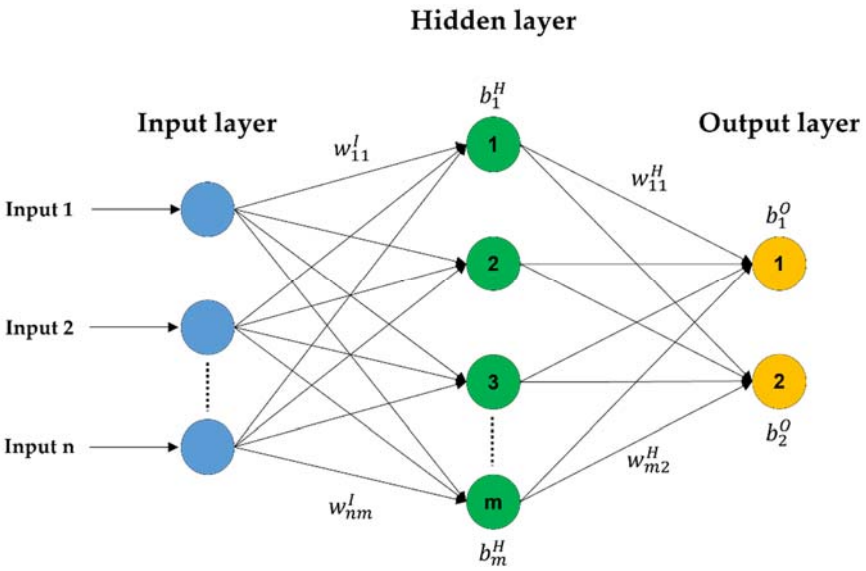

Figure III-1. Example of a feedforward network with multiple layers.

The feedforward supervised network with backpropagation learning rule is one of the most used ANN [5-8]. As shown in Figure III-1, the general structure of an ANN is made up of three parts: input, hidden and output layers [2]. The first layer receives input data that are then delivered to the hidden layer/s. Here, the core of the process takes place. The number of hidden layers and their neurons depends on the nature and the complexity of the problem. Then, the output layer shows the final result of the process performed by the previous layers. While the optimum number of hidden layers and neurons have to be decided upstream through a trial-and-error approach, the weights of each connection are evaluated starting from a training set of data. In fact, as previously explained, in order to find the best relation between input and output, connection weights and biases are continuously adjusted trying to get closer to the experimental outcome [3].

Neural networks can be used to classify inputs into categories (pattern recognition, supervised learning), to find a model that provide the best fit of inputs data (regression analysis, supervised learning) and to group data by similarity (clustering, unsupervised learning).

Therefore, thanks to their adaptability to different problems and goals, ANN have proved to be a powerful tool in several fields including the pharmaceutical and nanotechnology research [2,4,9-14]. In fact, to reach the desired morphological, structural and functional properties of the nanovector, many variables have to be considered and handled. However, the control of nanovector properties such as size, shape and charge, together with the encapsulation efficiency and loading degree of

drugs and/or imaging agents, is essential since they influence the nano-biointeractions and, consequently, the therapeutic and diagnostic efficacy. Among nanoparticles characteristics, size is crucial to overcome biological barriers and reach the specific target site. In fact, delivery aspects, including blood circulation half-life, opsonisation, targeting cellular uptake and tumor permeability are all influenced by nanoparticle size [15-18]. Therefore, when nanostructures are designed for a specific application, NPs size needs to be accurately chosen. Recently, several works have taken advantage of ANNs to predict NPs size and find the optimal process conditions.

In 2011, Asadi et al. developed an ANN model to understand which process parameter influenced the most the size of PLA-PEG-PLA nanoparticles produced by nanoprecipitation under different conditions [19]. Successively, Youshia et al. built a predictive model to estimate the size and the polydispersity index of polymeric nanoparticles (ethyl cellulose and PLGA of different molecular weights) produced by emulsification solvent evaporation method identifying PVA concentration as the main influential parameter on the final output [20]. Instead, the effect of PEG chain length, chitosan/PEG ratio and pH of solution on NPs size and zeta potential was studied by Bozuyuk et al. using ANN and predicted results were confirmed through experimental characterization [21]. Recently, Maleki et al. took advantage of ANN to find the optimized formulation to produce mPEG-PLGA nanoparticles with an ideal size for the simultaneous delivery of etoposide and paclitaxel [22].

To obtain the desired nanoparticles size, the optimization, the control and the reproducibility of the adopted production methods are crucial. Microfluidics offers several advantages to finely tune and precisely control nanoparticles size and other properties [23-28]. However, the number of parameters to handle goes up leading to huge experimental campaigns to find the optimal process conditions due to the nonlinear nature of the relationships between input and output parameters of the microfluidic process. ANN models can help to predict one or more outputs allowing to save time and effort. Recently, several works have developed ANNs to predict different parameters involved in the production of nanoparticles by microfluidics. Ali et al. in 2009 created an ANN to identify the factor that influenced the most the prednisolone nanoparticles size produced by nanoprecipitation in a microfluidic device [29]. They found out that the antisolvent flow rate play a key role in the supersaturation phenomenon by promoting the nucleation rate to the detriment of growth at higher value leading to smaller particles size. Instead, Aghajani and co-workers developed ANN models to study different nanoprecipitation process in the same microfluidic reactor for distinct purposes: the polydispersity index and the stability of an acetaminophen suspension and the size of stable ^{127}I nanoparticles [5,6,8]. In all three cases, the microfluidic parameters and the presence of surfactant

had a direct or inverse relation on the final output. Very recently, Damiati et al. developed ANN predictive models for PLGA droplet and particle sizes produced in three diverse microfluidic systems, both individually and in sequential combination, demonstrating a really accurate prediction [30].

3.2 Aim of the Chapter III

In this Chapter, the aim is to take advantage of machine learning to investigate the influence of different process parameters on the final outcome in a microfluidic system. Starting from the experimental data obtained in the previous Chapters, two different artificial neural networks are developed to find a relationship between input parameters and the obtained size with the goal to modulate the process and get the desired nanoparticles dimension. In fact, the building of the network allows to obtain information about the trend on the size also for input values not experimentally explored. Furthermore, we intend to pursue a similar goal to explore a microdroplet generation process performed for two different hyaluronic acid molecular weights through an analysis of the obtained flow regimes since they can lead to different microparticles size. In addition, another aim is the preliminary study of the interaction between HA-DVS hydrogel and GD-DTPA solutions to deeply explore, through the use of an ANN, the Hydrodenticty effect.

3.3 Materials and Methods

3.3.1 Materials

For the production of polymer microparticles, Hyaluronic Acid (HA) with two different molecular weights (50 and 250kDa) has been purchased from CreativePEGWorks (Chapel Hill, NC, USA). Divinyl sulfone (DVS) (contains <650 p.p.m. hydroquinone as inhibitor; purity 97%; density 1.117 g/mL at 25_C (lit.), molecular formula C4H6O2S, Mw = 118.15 Da) and sodium hydroxide NaOH (ACS reagent, ≥97.0%, Mw = 40.00 Da), purchased from Merck KGaA (Darmstadt, Germany)., has been used to perform the crosslinking reaction of polymer chains.To prepare the continuous phase, Mineral oil (density 0.84 g/ml at 25°C) and non-ionic surfactant Span80 (molecular formula C24H44O6; density 0.986 g/ml at 25 °C; HLB 4.3 (lipophilic); viscosity 1000-2000 mPa*s at 20°C) have been purchased from Merck KGaA (Darmstadt, Germany). Acetone (CHROMASOLV, for HLPC, ≥99.8%; the molecular formula: CH_3COCH_3), used for device cleaning, has been obtained from Merck KGaA (Darmstadt, Germany) as well as the water used for synthesis and characterization purified by distillation, deionization and reverse osmosis (Milli-Q Plus, Q-POD®).

Materials used for the production of CS-HA and PLGA NPs have been presented in Chapter 1 and 2, respectively, while in the case of crosslinked HA hydrogel – Gd solution, they have been reported in the Material section of the work published by Ponsiglione et al. [31].

3.3.2 Methods

3.3.2.1 Microfluidic strategies for the synthesis of nano and microparticles

In the case of PLGA and CS-HA NPs, reactions have been carried out within the main body of a custom-made quartz glass microfluidic chip, designed to promote the hydrodynamic flow focusing thanks to a junction angle of 135° between the middle channel and each one of the two side channels. Details about the microfluidic platform and the production processes are reported in the Method section of Chapter 1 and 2 for CS-HA and PLGA NPs, respectively.

Instead, for the production of HA μPs, an innovative microfluidic platform has been used to produce droplets with a really high size monodispersity. The Telos® System (Dolomite Microfluidics, Blacktrace Holding Ltd brand, Royston, UK) is an ideal product for the scale-up of the process since up to 10 modules can be assembled and work in parallel. Each Telos® module is provided with a valves system that allows to interrupt or not its own input streams. Thanks to a clamp mechanism, each module holds a microfluidic chip of 7 junctions. This means that a full system setup is able to carry out 70 droplet generation processes in parallel enabling the daily production of litres of droplets or particles. In this case, two modules have been used to perform the process, each one provided with a Telos® 2 Reagent Chip SC with channel dimension of 100 μm. To push reagent solutions, Mitos Pressure Pumps (Dolomite Microfluidics, Blacktrace Holding Ltd brand, Royston, UK) flow rate (μL/min) or pressure (mbar) has been set thanks to the Flow Control Centre software and flow sensors that allow a continuous conversion according to the density and viscosity of fluids in the software library. In particular, pressure has been managed for the known Mineral Oil while flow rate has been chosen for the polymer solution. Finally, a system of FEP tubing links each pump with the Telos® System and permits droplets collection.

By keeping constant the oily continuous phase at values of 600, 700, 800 and 900 mbar, the flow rate of the dispersed phase has been varied in a wide range to observe changes in the obtained microfluidic regime. In particular, every 10 minutes, the flow rate of the polymer phase has been increased of 2 μL/min. However, due to the high polymer concentration used to carry out the process (1 and 2.5 %w/v for the HA 250 and 50 kDa, respectively), the pressure of the dispersed phase has been continuously monitored. In fact, to keep constant the flow rate, abnormal pressure values have been reached when a channel blockage occurs. In the flow focusing

configuration, different dripping sub-regimes have been observed as result of surface tension, viscous and inertial forces until co-flow as shown in Figure III-2.

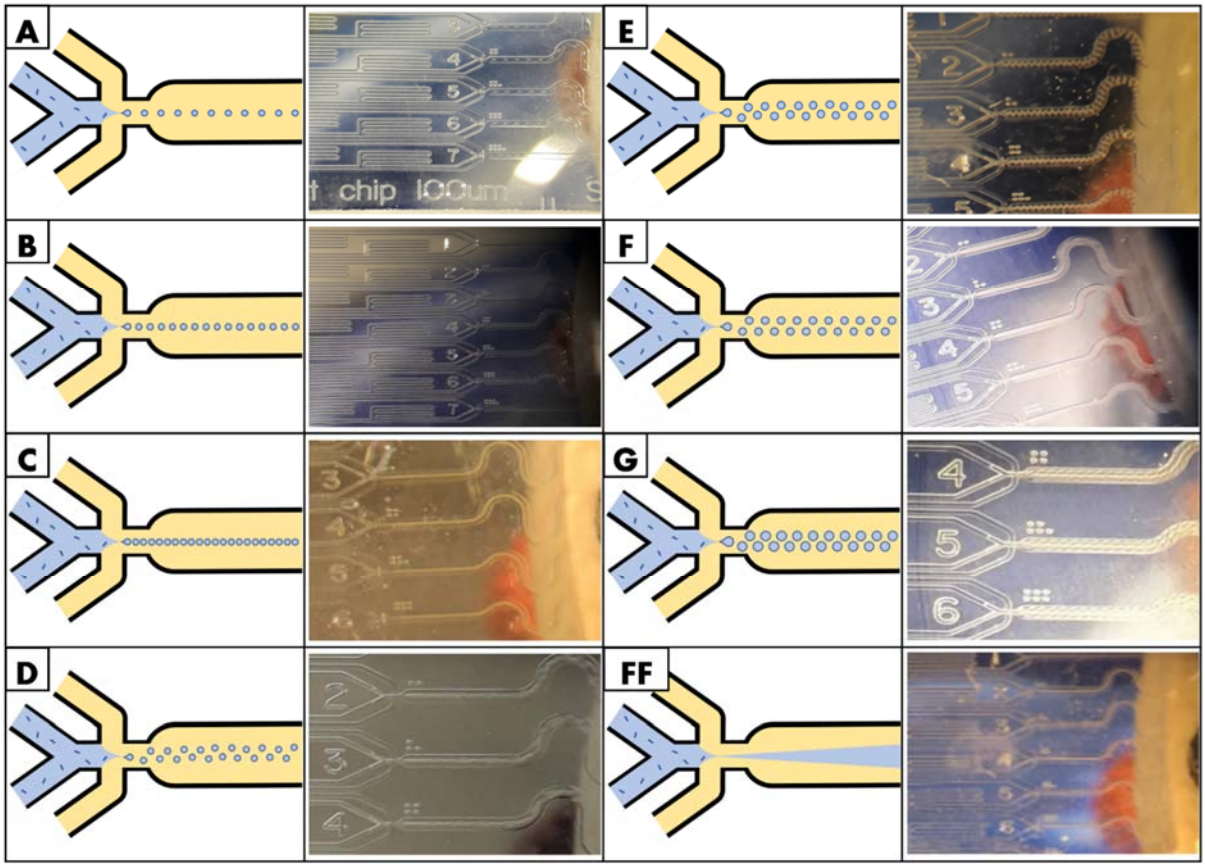

Figure III-2. Schematic representation and relative image of the different observed microfluidic droplet generation regimes.

3.3.2.2 Biopolymer matrices to study the interaction with Gd-DTPA

Data about the longitudinal relaxation rate of Gd-DTPA in a crosslinked or non-crosslinked HA hydrogel at different conditions have been taken from the Supplementary material of the study conducted by Ponsiglione et al. (see Method and Result section for details about the preparation of samples and the performed measurements) [31]. In addition, further data have been created by linear interpolation with the aim to increase the variability of the input data.

3.3.2.3 Artificial neural networks

ANN have been implemented using MATLAB R2020a software. A multilayer feedforward-back propagation neural network has been used for all the four microfluidic processes described above in order to model the complex input-output relationships. The adopted ANN architecture consists of three separate layers, an input layer, one hidden layer and an output layer as showed in Figure III-3.

		NEURAL NETWORK	INPUT PARAMETERS	OUTPUT PARAMETERS
PLGA NPs	REGRESSION PROBLEM	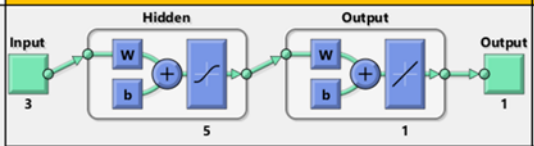	• PLGA concentration (mg/mL) • Middle flow rate (μL/min) • Side flow rate (μL/min)	Nanoparticles size
CS-HA NPs		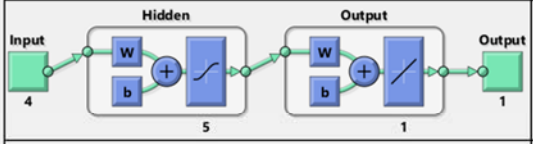	• CS concentration (%w/v) • HA concentration (%w/v) • TPP concentration (%w/v) • Flow rate ratio	
HA-DVS Hydrogel		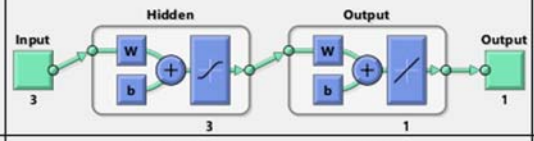	• Gd concentration (mM) • HA concentration (%w/v) • DVS concentration (%w/v)	Relaxation rate
HA μPs	CLASSIFICATION PROBLEM	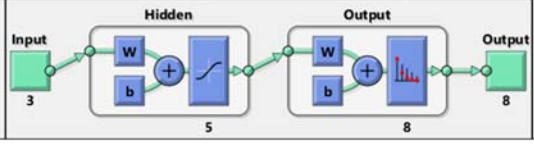	• HA concentration (%w/v) • Oil pressure (mbar) • Middle flow rate (μL/min)	Microfluidic regime

Figure III-3. Scheme of Artificial Neural Networks architectures used to resolve regression (PLGA and CS-HA NPs, HA Hydrogel – Gd solution) and classification problem (HA μPs), each one with its own input and output parameters.

The optimum number of neurons in the hidden layer has been selected through a trial-and-error approach. The Levenberg-Marquardt algorithm has been chosen as training function to optimize the Mean Squared Error (MSE). Experimental samples have been divided into three groups: the "training subset" (70% of the samples) to train the network in order to establish the input–output relationships trying to match experimental data; the "validation subset" (15% of the samples) to stop overtraining during the learning process; the "test subset" (15% of the samples) to evaluate the trained network predictability. The number of input variables are chosen among the main process variables (microfluidic and polymer/contrast agent concentrations parameters) that experimentally have influenced the final output (see Figure III-3). According to the problem, the number of outputs has been different: one neuron for regression where the final goal is the NPs size or the longitudinal relaxation rate prediction while eight neurons for classification, one for each response class, where the target variables are the microfluidic regime.

Obviously, the representation of the result is different depending on the problem. In the case of regression, an example of the expected result is showed below (Figure III-4). The experimental and predicted NPs sizes are reported on the x and y axis respectively. The blue line represents the fitting of the data predicted by the ANN with the experimental ones while the dashed lines their perfect correspondence.

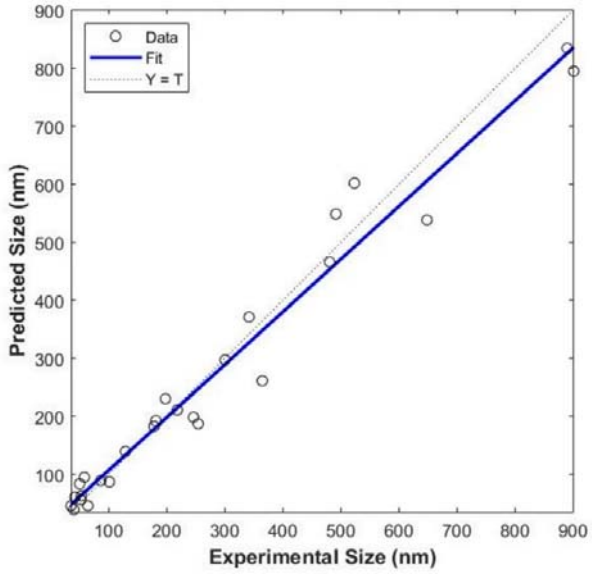

Figure III-4. Example of regression analysis plot between predicted and experimental data

The predictive capability of the two trained regression model has been evaluated by computing the squared correlation coefficient, the determination coefficient R^2 and the root-mean-square-error (RMSE). This has been done both for each subset (training, test and validation) and the whole dataset. In particular, the R^2 and the RMSE are calculated using the following equations[7,19]:

$$RMSE = \sqrt{\frac{1}{n}\sum_{i=1}^{n}\left(y_i - y_p\right)^2} \quad (1)$$

$$R^2 = 1 - \frac{\sum_{i=1}^{n}\left(y_i - y_p\right)^2}{\sum_{i=1}^{n}(y_i - \bar{y})^2} \quad (2)$$

where y_i are the experimentally observed values, y_p are the predicted values by the ANN and $\bar{y}$ is the mean of the variable. The closer to 1 is the R^2, the better is the predictability of the model.

In addition, the impact of input variables on the output is determined calculating the contribution of i-th input data to k-th output (C_{ik}), which represents the relative importance of input data according to the weightings of the ANN model, using the following equation[7,19]:

$$C_{ik} = \left|\sum_j \ a_{ij} \times b_{jk}\right| \quad (3)$$

where a_{ij} are the weightings of connecting links between i-th input neuron and j-th hidden neuron, while b_{jk} are the weightings of connecting links between j-th hidden neuron and k-th output.

Finally, a semi-quantitative method is adopted to get insight into interactions between the input variables and the output of the microfluidic processes [19,29,32]. Thanks to the use of 3D-graph obtained from the optimized ANN, it is possible to have on overview of how the output changes depending on two input variables, while keeping the remaining inputs constant.

In the case of classification of microfluidic regimes, the confusion matrix describes the performance of the ANN in terms of identification of the correct class (see Figure III-5). Along the diagonal the number of true positives for each class are reported while the other cells represent the classification errors. The x and y percentages stand for the correct and incorrect classification, respectively. These latter are referred to the predicted classes moving along rows while to the experimental classes along columns. Lastly, in the corner of the matrix, xT returns the total percentage of correct classification of input data while yT the percentage of misclassification.

Figure III-5. General aspect of confusion matrix as result of ANN classification

3.4 Results

3.4.1 Regression to predict NPs size

3.4.1.1 Prediction of PLGA NPs size

Table III-S1 in Appendix C shows the experimental NPs size measured by DLS technique, the predicted size and error values calculated by the ANN model for the PLGA NPs. A total number of 30 trials have been used to build up the ANN model (20 for train and 5 for both test and validation). The correlation relationship between the target and predicted data is analysed in Figure III-6.

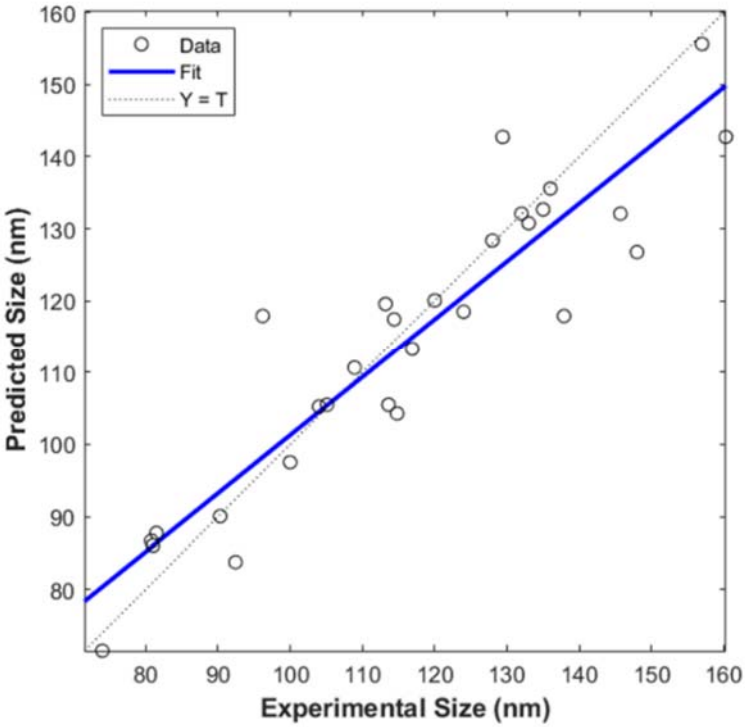

Figure III-6. Experimental versus predicted PLGA NPs size and regression for all data set.

The best predictive model has given R and RMSE values of 0.93368 and 7.95979, 0.94631 and 12.40957, and 0.95582 and 13.84081 for training, validation, and test data, respectively. The overall R for the model is 0.9086 with a RMSE of 9.99165, representing a measure of the quality of the trained network and of its high predictability. The prediction error has been also analyzed to find possible trends based on PLGA concentration.

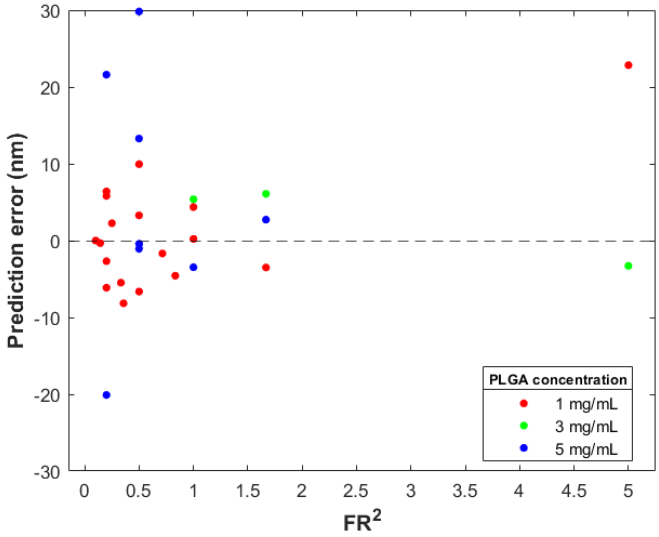

Figure III-7. Prediction error plot at different in the estimation of PLGA NPs size FR^2 based on polymer concentration

As shown in Figure III-7, the predicted size diverges of ±30 nm at most from the experimental data for all data set. The prediction error is even lower than 10 nm for $FR^2 \leq 2$ when PLGA concentration is equal to 1 mg /mL.

Once the weights of neuron connections have been established by the model, it is possible to estimate the relative importance of each input parameter on the NPs size using the formula indicated in the method section (see Figure III-8). The highest influence of the side flow rate on the final outcome is validated by the Karnik and co-workers' theory[25]. In fact, the supersaturation rate and the mixing time within the microfluidic chip are strongly dependent on this parameter. For example, increasing the side flow rate value, the supersaturation level is quickly reached and the mixing time is faster leading to promote nucleation to the detriment of growth resulting in smaller NPs.

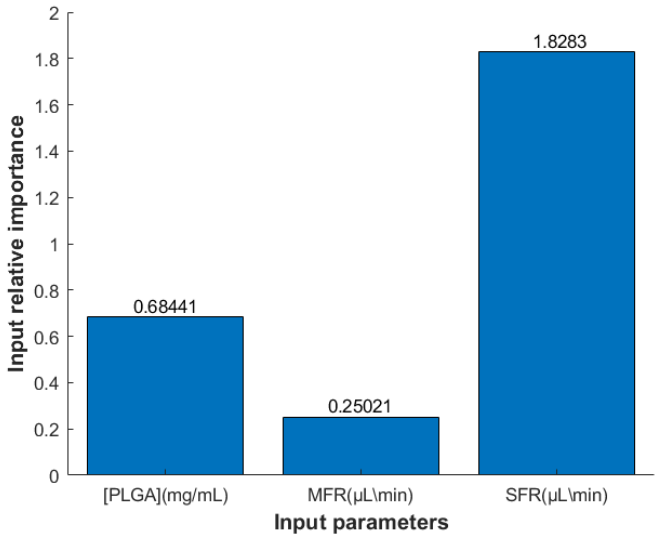

Figure III-8. Relative importance of the three input parameters on the outcome predicted by the PLGA ANN.

In order to evaluate the effect of the flow rates on the NPs size, 3D graphs have been plotted by varying middle and side flow rates and keeping constant the PLGA concentration at the three experimentally tested values (1, 3 and 5 mg/mL).

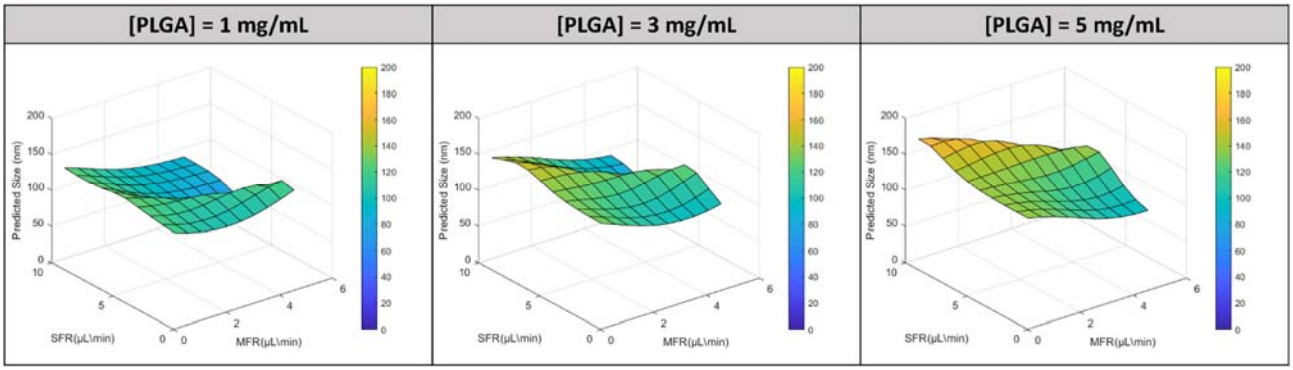

Figure III-9. ANN simulations of the influence of middle and side flow rates at different PLGA concentrations.

According to the Figure III-9, results shown that higher size are obtained when the polymer concentration grows. Moreover, a threshold that moves to higher side flow rate values by increasing PLGA concentration comes out in the NPs size trend. In the following plots, the experimental and predicted values are added to the previous graph to show how much the values diverge from the curves of the ANN model.

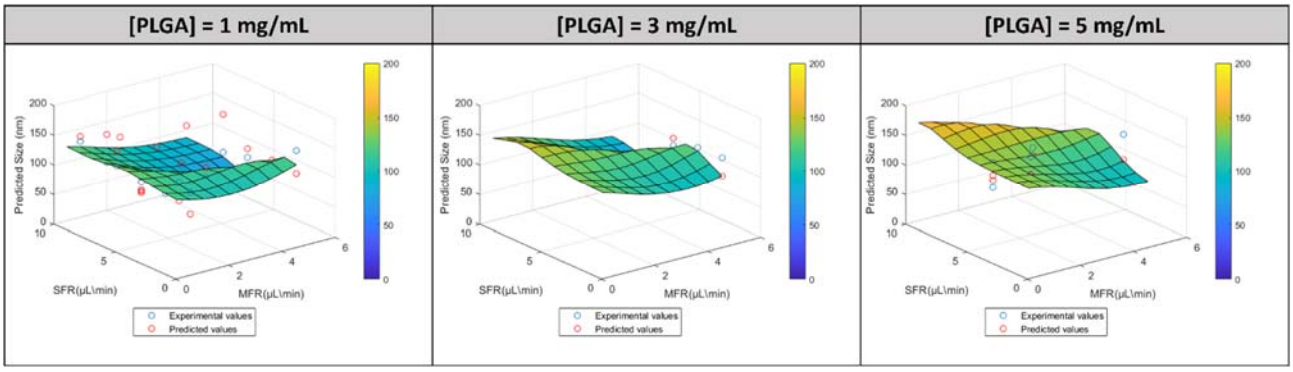

Figure III-10. 3D curves of the predicted size at different PLGA concentration compared to experimental and predicted values.

3.4.1.2 Prediction of CS – HA NPs size

Table III-S2 tabulates the NPs size measured by DLS technique and the predicted size and the error values estimated by the ANN for the CS-HA NPs. Looking at predicted values, it is possible to notice that, despite the great variability of the experimental NPs size, the ANN model sometimes predicts the same size. The explanation lies in the relative value of input parameters since, although identical or similar to each other, has led to experimentally different NPs size. Therefore, the ANN is able to predict only one value for that input values combination highlighting a not proper control of the NPs production process or not well performed size measurements. This aspect is reflected on the correlation between experimental and predicted NPs size as shown in the following figure.

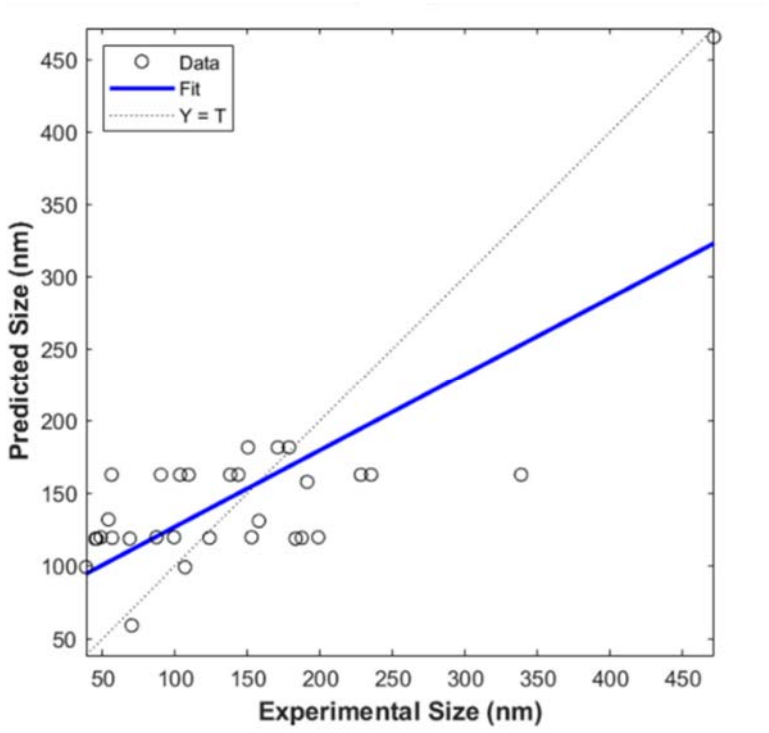

Figure III-11. Experimental versus predicted CS-HA NPs size and regression for all data set.

The best predictive model has given R and RMSE values of 0.74861 and 67.69205, 0.82774 and 43.89277, and 0.95675 and 44.732 for training, validation, and test data, respectively while the overall R f is 0.74524 with a RMSE of 61.46874.

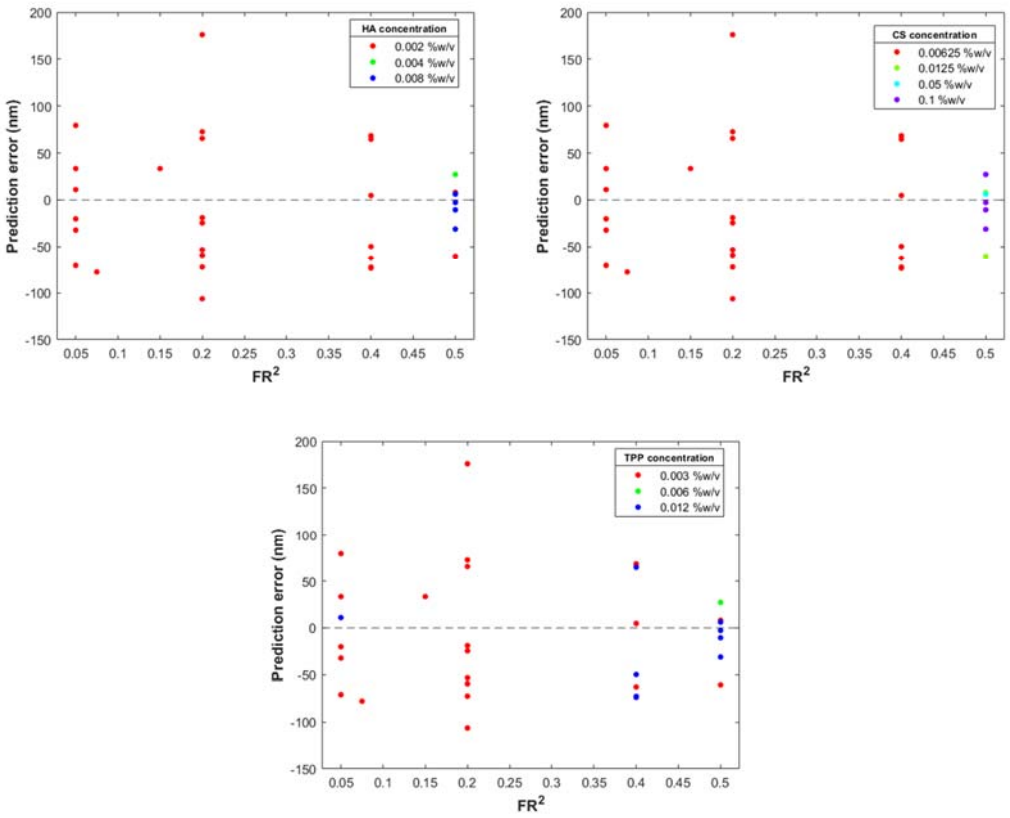

Figure III-12. Prediction error of the ANN in the estimation of CS-HA NPs size at different FR^2 based on HA, CS or TPP concentrations

The prediction error has been plotted based on HA, CS or TPP concentration in order to find possible trends. The error values are lower at $FR^2 = 0.5$, identified as the experimental optimal condition, independently from polymers or crosslinker concentration point of view. However, there is a lack in the variability of input data that does not allow to highlight a clear explainable trend. Therefore, the same analysis has been carried out on data divided in the two operational regimes, *High* and *Low*, as explained in the Chapter 1 and showed in Figure III-13.

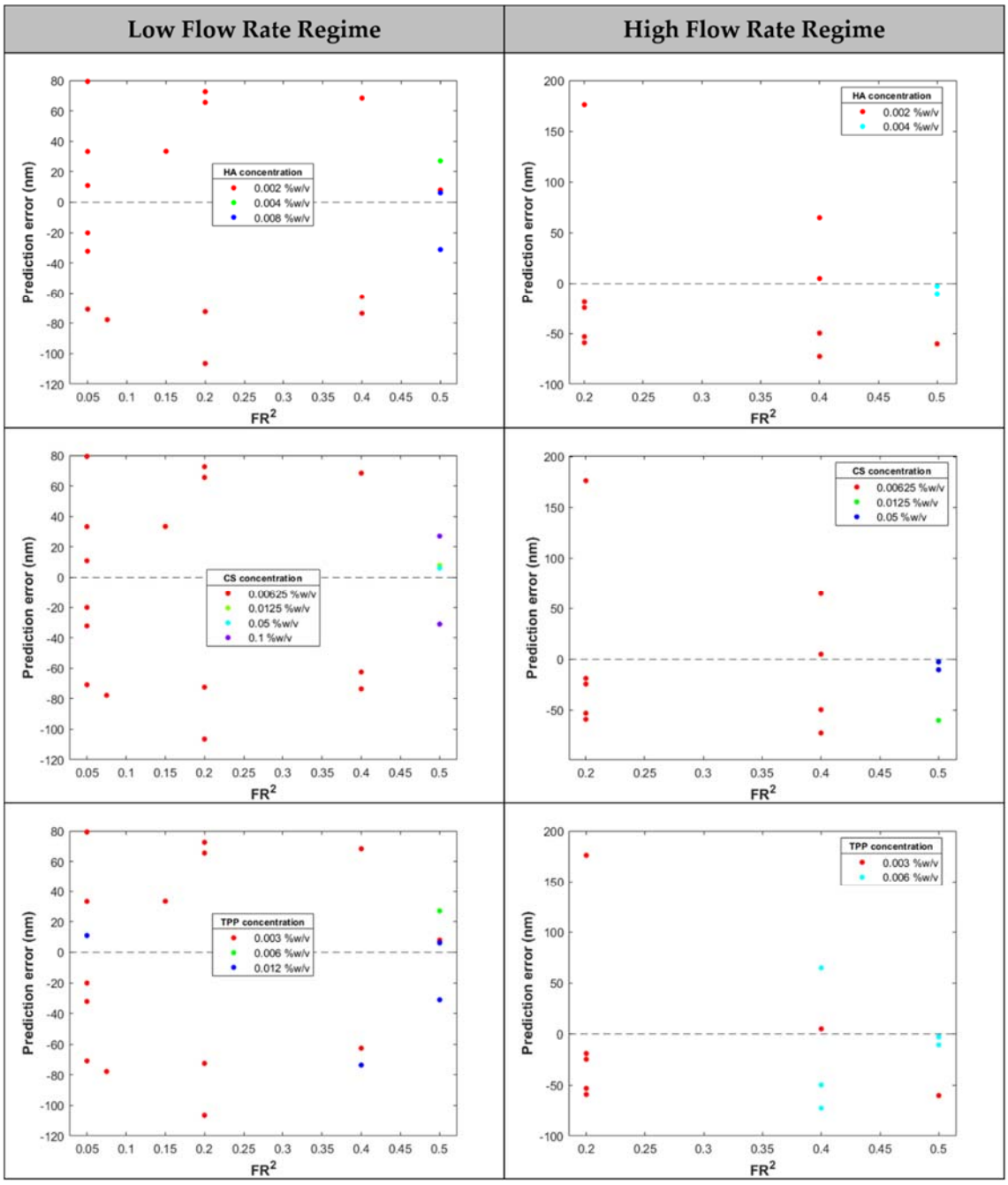

Figure III-13. Prediction error of the ANN in the estimation of CS-HA NPs size at different FR^2 based on HA, CS or TPP concentrations in the two operational regimes.

Even in this case, no trend in the prediction error has been found and the consideration previously done are still valid. About the influence of each input parameter on the predicted NPs size, there is an almost equal contribution of polymers and crosslinker concentrations as shown in Figure III-14.

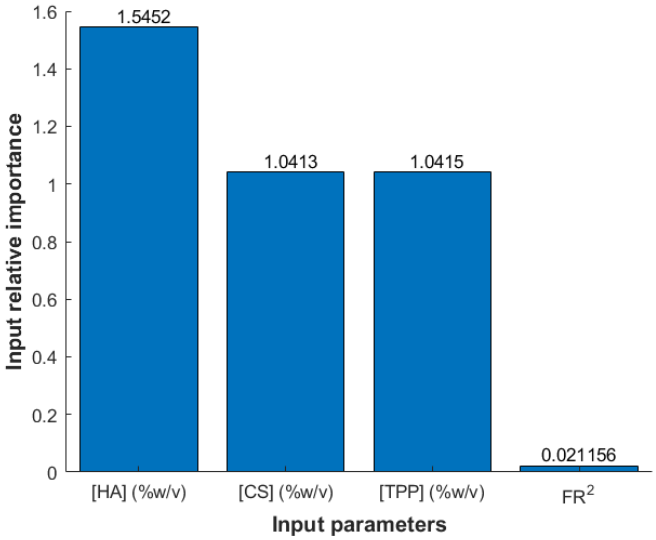

Figure III-14. Relative importance of the four input parameters on the outcome predicted by the CS-HA ANN.

The slightly higher value of hyaluronic acid importance can be related to the formation of the hydrophilic coating of the NPs that influence the water supply and consequently the NPs size.Finally, the prediction of NPs size trend has been represented through the use of 3D graphs in Figure III-15. It is worth to notice that a greater effect on NPs size occurs increasing HA concentration both for different and same CS concentration. Moreover, it seems that the TPP and FR^2 influence on NPs size decrease by reducing CS concentration in particular at HA value of 0.008 %w/v.

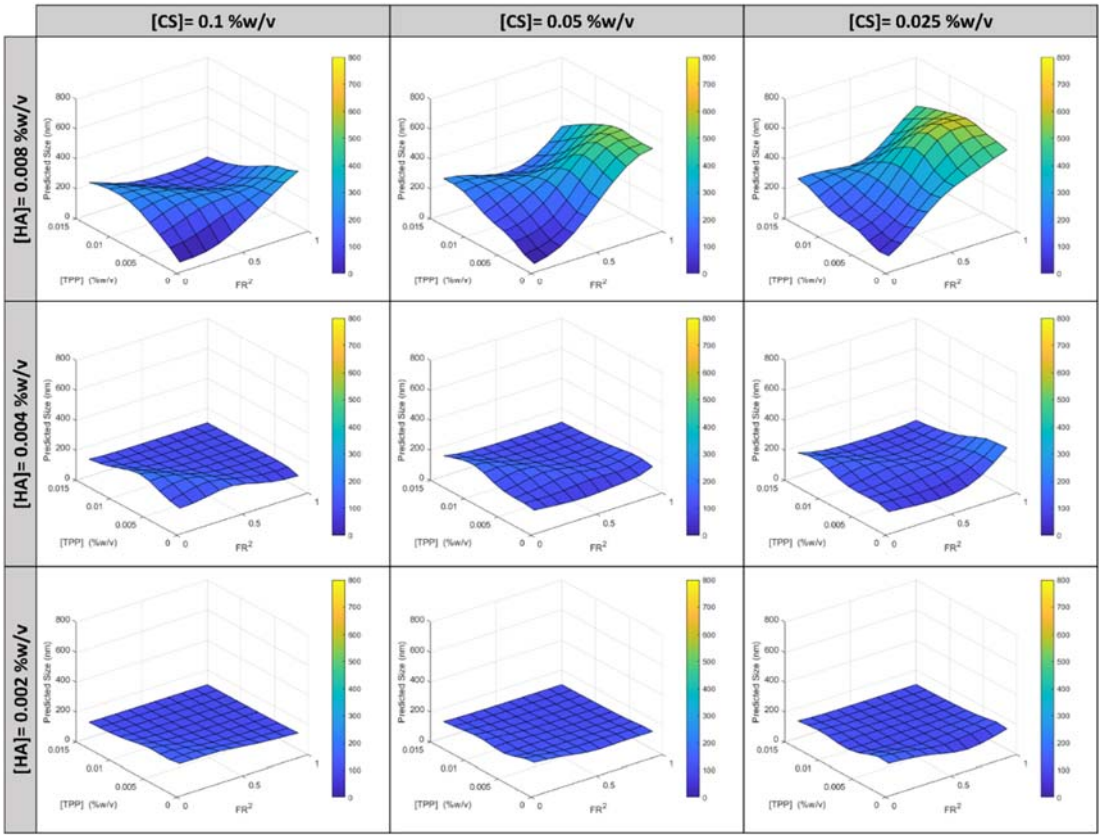

Figure III-15. ANN simulations of the influence of FR^2 and TPP concentration at different CS and HA concentrations

3.4.1.3 Models comparison

The overall R^2 and the RMSE of the two implemented ANN models are reported in the following table.

Table III-1. Comparison of the determination coefficient (R^2) and RMSE in both models.

	PLGA NPs	CS-HA NPs
R	0.9086	0.7424
R^2	0.8255	0.55
RMSE	9.9917	61.47

The lower values of R and R^2 and the higher value of RMSE of CS-HA NPs relies on the variability of input data as previously discussed by looking at the distribution of prediction error. Instead, the ANN model of PLGA NPs seem to estimate quite well the size remaining in a narrow range of error.

3.4.2 Regression to predict gadolinium relaxation rate in a HA crosslinked hydrogel

In the Table III-S3 the relaxation rates obtained by benchtop relaxometer measurements are listed together with the predicted values and the prediction errors. As visible in Figure III-16, the correlation between experimental and predicted values is really high.

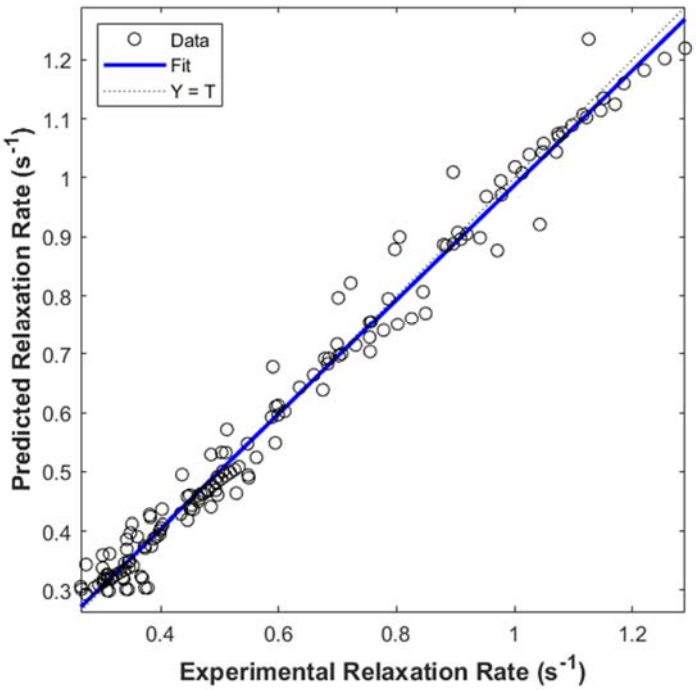

Figure III-16. Experimental versus predicted relaxation rate and regression for all data set.

In fact, the best predictive model has given R and RMSE values of 0.99122 and 0.036224, 0.99586 and 0.03138, and 0.9832 and 0.046698 for training, validation, and test data, respectively. The overall R for the model is 0.99095 with a RMSE of 0.037316 demonstrating the high prediction accuracy of the network. The prediction error has been analyzed based on DVS concentration. As shown in Figure III-17, the relaxation rate diverges of ±0.12 s^{-1} at most from the experimental data for all data set but a trend has not been found.

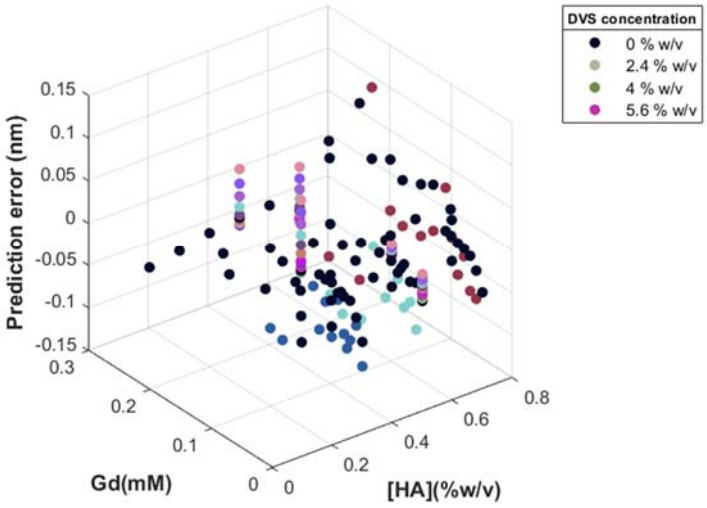

Figure III-17. Prediction error of the ANN in the estimation of the relaxation rate at different HA and Gd concentrations based on DVS concentration

In the following figure, the relative importance of each input parameter on the predicted relaxation rate has been displayed. The obtained result can be explained by looking at the Solomon-Bloembergen Morgan (SBM) theory and the *Hydrodenticity* concept [33-37]. In fact, according to the first thesis, the interaction between the contrast agent and water molecules lead to strongly increase the longitudinal relaxation rate. In addition, the presence of a hydrophilic polymer such as HA and the crosslinking degree affect the water molecules' dynamics and in particular the SBM correlation times as explained by the Hydrodenticty effect [31]. Therefore, the improved relaxation rate is the result of an increased residence lifetime of water molecules within the crosslinked polymer matrix, a restricted molecular tumbling, and a resulting faster exchange rate with metal ions.

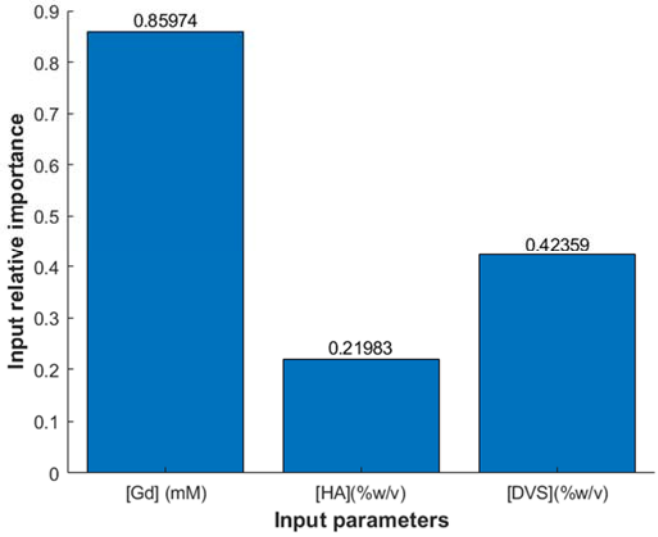

Figure III-18. Relative importance of the four input parameters on the outcome predicted by the CS-HA ANN.

Finally, the ANN has been used to simulate the trend of the relaxation rate at Gd concentration values of 0, 0.1 and 0.2 mM to varying HA and DVS conditions (Figure III-19).

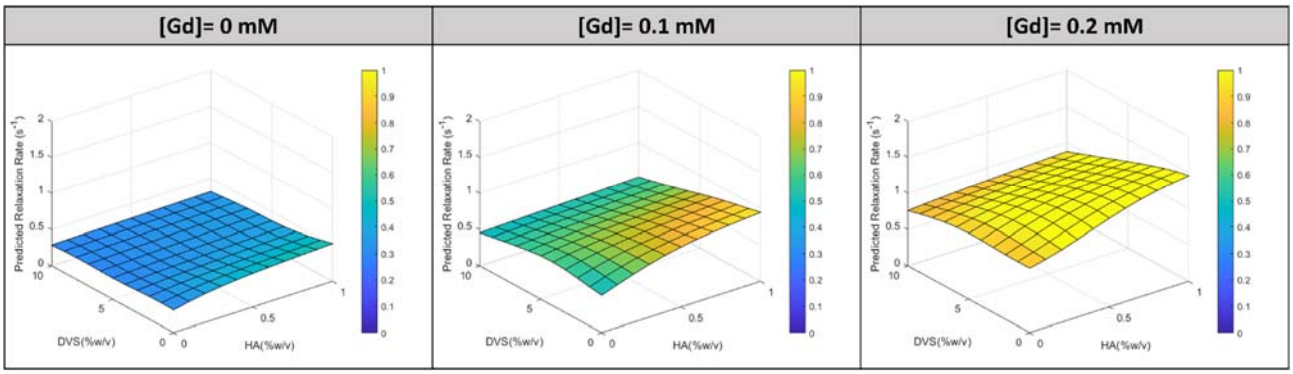

Figure III-19. ANN simulations of the influence of HA and DVS concentration at different Gd concentrations

As expected, the longitudinal relaxation values grow with the Gd concentration while a different dependence from HA and DVS concentrations comes out, in particular at Gd values different from zero. In fact, the relaxation rate seems to grow with the increase of HA concentration. However, the DVS concentration negatively affect the relaxation rate. This predicted behaviour could be due to a too high crosslink degree of the hydrogel that involves the reduction of the total volume leading to expel water from the polymer matrix. The result is an increment of the free bulk water that less easily enters in the hydrogel and interacts with Gd causing a slight reduction of the total relaxation rate.

3.4.3 Prediction of microfluidic regimes

Confusion matrices in Figure III-20a and c show the result of the prediction of the different dripping microfluidic regimes (A to G) up to the transition to the hydrodynamic flow focusing (FF) for the HA with a molecular weight of 50 and 250 kDa, respectively.

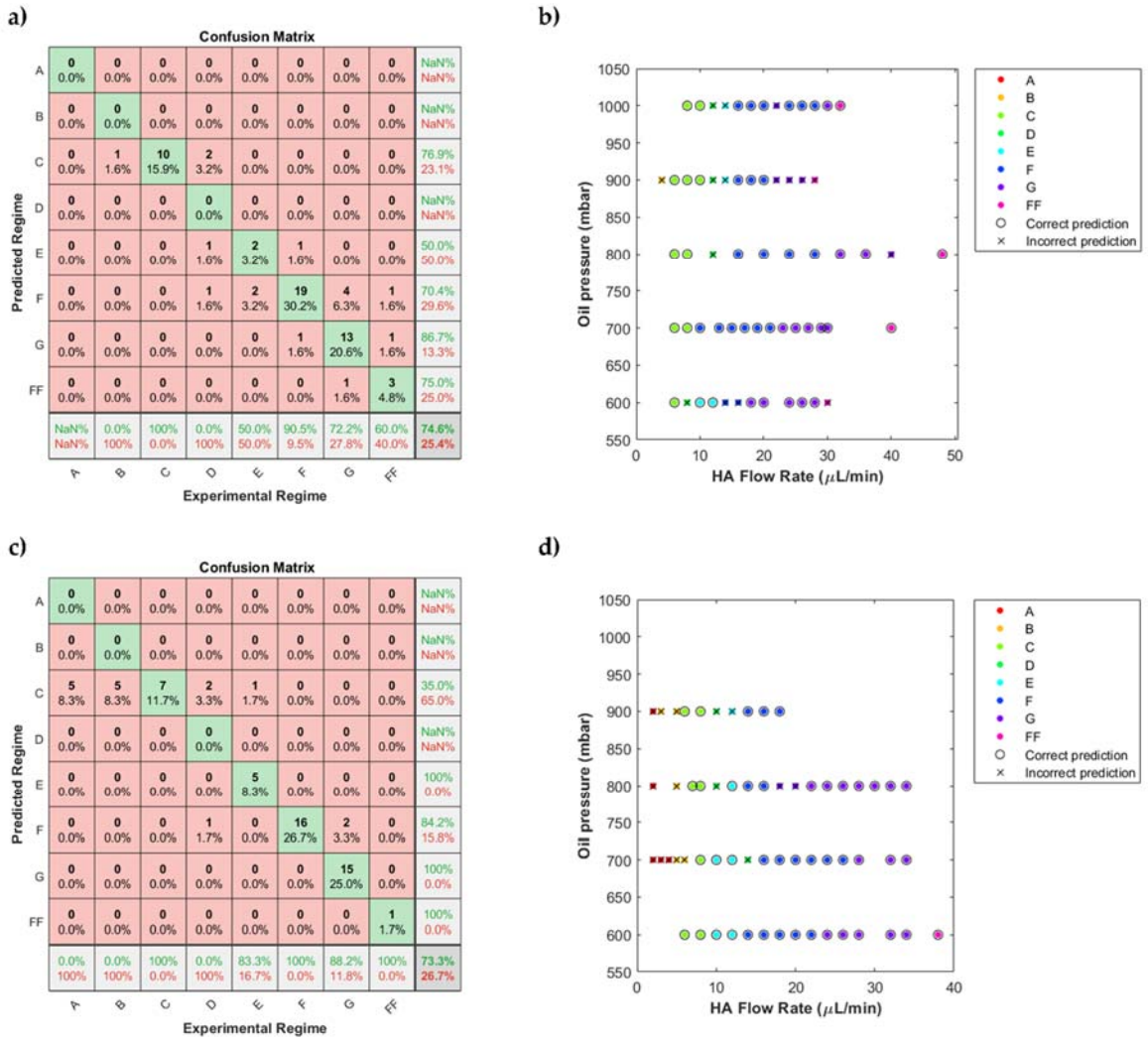

Figure III-20. Confusion matrix representing the classfication of the dripping regimes by ANN compared to the experimental obtained ones for **(a)** HA 50 kDa and **(c)** HA 250 kDA; Identification of the misclassification points at different mineral oil pressure and polymer solution flow rates based on the specific regime for **(b)** HA 50 kDa and **(d)** HA 250 kDa.

Looking at the lower right corner of the first matrix, the total misclassification error is 25.4 % while the 74.6 % of data are correctly predicted. In the case of HA 250 KDa, the percentages are more or less the same: 73.3 % of regimes correspond to the experimental ones and 26.7 % are differently predicted. In particular, Figure III-20b and d show the Mineral Oil pressure – HA flow rate combinations of data that are correctly or no predicted for both molecular weights.

Successively, another attempt has been done with the same ANN models by grouping microfluidics regime based on the layer of microparticles that are formed within the output channel during their production. In particular, data have been divided in three groups: Monolayer (A, B, C), Bilayer (D, E, F, G) and Flow Focusing (FF).

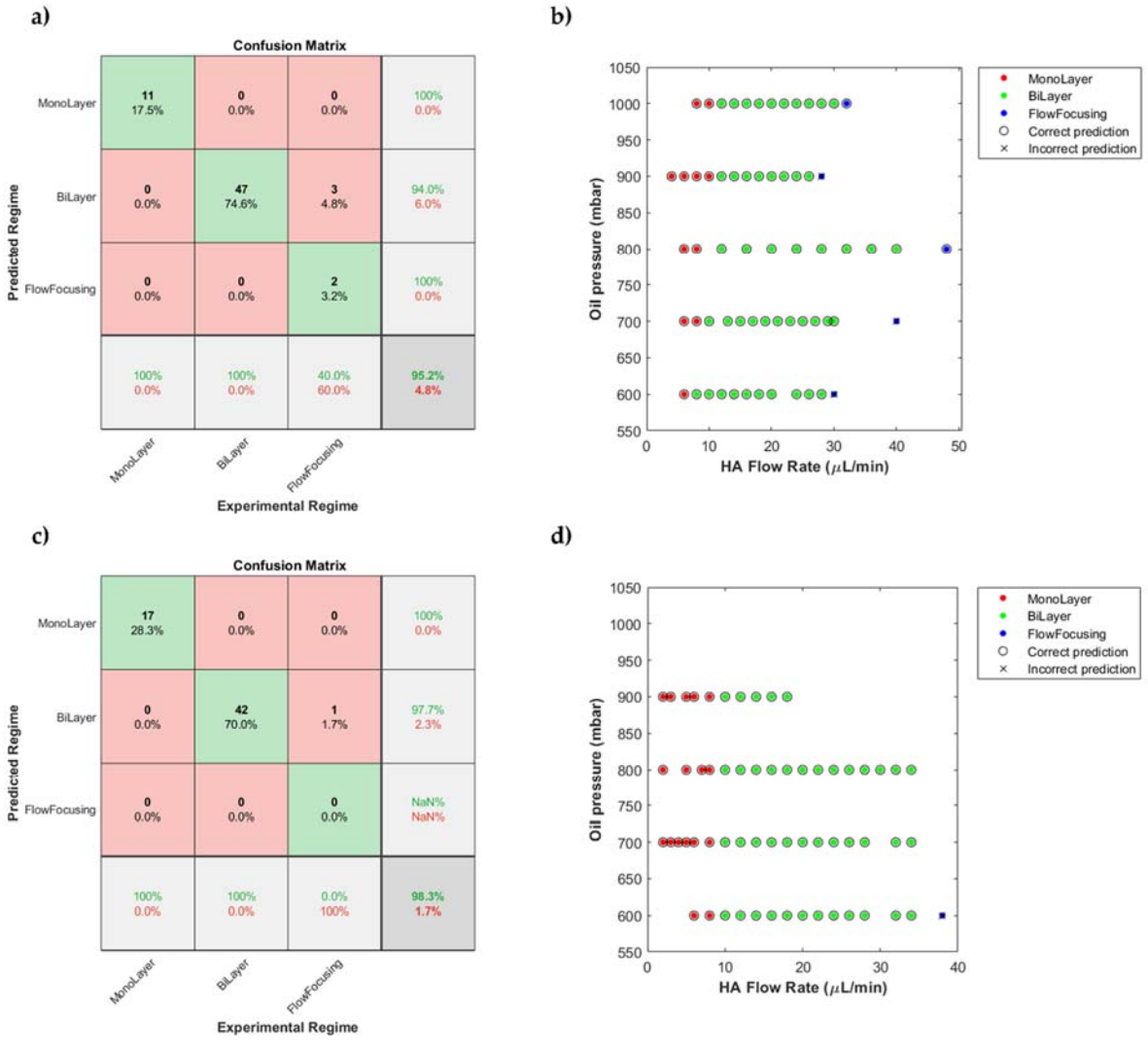

Figure III-21. Confusion matrix and individuation of the points misclassified by the ANN after the grouping of similar regimes for HA 50 kDa (**(a)** and **(b)**) and HA 250 kDa (**(c)** and **(d)**).

As shown in Figure III-21, the misclassification error is drastically reduced in both cases since the range of prediction of each category is larger. However, in four cases, three for HA 50 kDa and one for HA 250 kDa, experimentally observed flow focusing have been predicted as Bilayer. This result most likely suggests that the high polymer concentration used to carried out both processes has resulted in a partial obstruction of the channel influencing the real fluidodynamics and so leading to an inaccurate categorization.

3.5 Conclusion

Four feedforward supervised ANNs have been developed to perform different tasks and get important information about processes and their operational parameters. Firstly, CS-HA and PLGA nanoparticles' size has been predicted starting from data collected in previous Chapters. The

nonlinear relationship between input and output has been analysed exploring the influence of each parameter on the final outcome and the predicted size trend by ANN. The two systems have shown a different correlation between predicted and experimental data highlighting the importance of a required variability of input data. Then, a droplet generation process for the production of polymer microparticles has been studied with the aim to understand if the observed regime corresponds to the real one. In fact, thanks to the use of ANN, it has been possible to understand that the high polymer concentrations used in the process for long time has influenced the fluidodynamics within the microfluidic chip leading to no correct droplet generation regimes. Finally, the behaviour of Gd-DTPA in a crosslinked HA hydrogel has been studied to quantify the impact of polymer matrix properties on the longitudinal relaxation rate of the contrast agent.

3.6 References

1. Patel, J.L.; Goyal, R.K. Applications of artificial neural networks in medical science. *Curr. Clin. Pharmacol .* **2007**, *2*, 217-226.
2. Agatonovic-Kustrin, S.; Beresford, R. Basic concepts of artificial neural network (ANN) modeling and its application in pharmaceutical research. *J. Pharm. Biomed.* **2000**, *22*, 717-727.
3. Krogh, A. What are artificial neural networks? *Nat. Biotechnol.* **2008**, *26*, 195-197.
4. Wu, Y.; Feng, J. Development and Application of Artificial Neural Network. *Wireless Pers. Commun.* **2018**, *102*, 1645-1656.
5. Aghajani, M.H.; Pashazadeh, A.M.; Mostafavi, S.H.; Abbasi, S.; Hajibagheri-Fard, M.; Assadi, M.; Aghajani, M. Size Control in the Nanoprecipitation Process of Stable Iodine (^{127}I) Using Microchannel Reactor-Optimization by Artificial Neural Networks. *AAPS PharmSciTech* **2015**, *16*, 1059-1068.
6. Aghajani, M.; Shahverdi, A.R.; Rezayat, S.M.; Amini, M.A.; Amani, A. Preparation and optimization of acetaminophen nanosuspension through nanoprecipitation using microfluidic devices: an artificial neural networks study. *Pharm. Dev. Technol.* **2013**, *18*, 609-618.
7. Hattori, T.; Kito, S. Analysis of factors controlling catalytic activity by neural network. *Catal. Today* **2006**, *111*, 328-332.
8. Aghajani, M.; Shahverdi, A.R.; Amani, A. The use of artificial neural networks for optimizing polydispersity index (PDI) in nanoprecipitation process of acetaminophen in microfluidic devices. *AAPS PharmSciTech* **2012**, *13*, 1293-1301.
9. Vamathevan, J.; Clark, D.; Czodrowski, P.; Dunham, I.; Ferran, E.; Lee, G.; Li, B.; Madabhushi, A.; Shah, P.; Spitzer, M.; et al. Applications of machine learning in drug discovery and development. *Nat. Rev. Drug Discov.* **2019**, *18*, 463-477.
10. Réda, C.; Kaufmann, E.; Delahaye-Duriez, A. Machine learning applications in drug development. *Comput. Struct. Biotechnol. J.* **2020**, *18*, 241-252.
11. Hayat, H.; Nukala, A.; Nyamira, A.; Fan, J.; Wang, P. A concise review: the synergy between artificial intelligence and biomedical nanomaterials that empowers nanomedicine. *Biomed. Mater.* **2021**, *16*, 052001.
12. Sacha, G.M.; Varona, P. Artificial intelligence in nanotechnology. *Nanotechnology* **2013**, *24*, 452002.
13. Nichols, J.A.; Herbert Chan, H.W.; Baker, M.A.B. Machine learning: applications of artificial intelligence to imaging and diagnosis. *Biophys. Rev.* **2019**, *11*, 111-118.

14. Abiodun, O.I.; Jantan, A.; Omolara, A.E.; Dada, K.V.; Mohamed, N.A.; Arshad, H. State-of-the-art in artificial neural network applications: A survey. *Heliyon* **2018**, *4*, e00938.
15. Elsabahy, M.; Wooley, K.L. Design of polymeric nanoparticles for biomedical delivery applications. *Chem. Soc. Rev.* **2012**, *41*, 2545-2561.
16. Hoshyar, N.; Gray, S.; Han, H.; Bao, G. The effect of nanoparticle size on in vivo pharmacokinetics and cellular interaction. *Nanomedicine (Lond.)* **2016**, *11*, 673-692.
17. He, C.; Hu, Y.; Yin, L.; Tang, C.; Yin, C. Effects of particle size and surface charge on cellular uptake and biodistribution of polymeric nanoparticles. *Biomaterials* **2010**, *31*, 3657-3666.
18. Yin Win, K.; Feng, S. Effects of particle size and surface coating on cellular uptake of polymeric nanoparticles for oral delivery of anticancer drugs. *Biomaterials* **2005**, *26*, 2713-2722.
19. Asadi, H.; Rostamizadeh, K.; Salari, D.; Hamidi, M. Preparation of biodegradable nanoparticles of tri-block PLA–PEG–PLA copolymer and determination of factors controlling the particle size using artificial neural network. *J. Microencapsul.* **2011**, *28*, 406-416.
20. Youshia, J.; Ali, M.E.; Lamprecht, A. Artificial neural network based particle size prediction of polymeric nanoparticles. *Eur. J. Pharm. Biopharm.* **2017**, *119*, 333-342.
21. Bozuyuk, U.; Dogan, N.O.; Kizilel, S. Deep Insight into PEGylation of Bioadhesive Chitosan Nanoparticles: Sensitivity Study for the Key Parameters Through Artificial Neural Network Model. *ACS Appl. Mater. Interfaces* **2018**, *10*, 33945-33955.
22. Maleki, H.; Naghibzadeh, M.; Amani, A.; Adabi, M.; Khosravani, M. Preparation of Paclitaxel and Etoposide Co-loaded mPEG-PLGA Nanoparticles: an Investigation with Artificial Neural Network. *J. Pharm. Innov.* **2021**, *16*, 11-25.
23. Ma, J.; Lee, S.M.; Yi, C.; Li, C. Controllable synthesis of functional nanoparticles by microfluidic platforms for biomedical applications – a review. *Lab Chip* **2017**, *17*, 209-226.
24. Capretto, L.; Carugo, D.; Mazzitelli, S.; Nastruzzi, C.; Zhang, X. Microfluidic and lab-on-a-chip preparation routes for organic nanoparticles and vesicular systems for nanomedicine applications. *Adv. Drug Deliv. Rev.* **2013**, *65*, 1496-1532.
25. Karnik, R.; Gu, F.; Basto, P.; Cannizzaro, C.; Dean, L.; Kyei-Manu, W.; Langer, R.; Farokhzad, O.C. Microfluidic Platform for Controlled Synthesis of Polymeric Nanoparticles. *Nano Lett.* **2008**, *8*, 2906-2912.
26. Russo, M.; Bevilacqua, P.; Netti, P.A.; Torino, E. A Microfluidic Platform to design crosslinked Hyaluronic Acid Nanoparticles (cHANPs) for enhanced MRI. *Sci. Rep.* **2016**, *6*, 37906.
27. Tammaro, O.; Costagliola di Polidoro, A.; Romano, E.; Netti, P.A.; Torino, E. A Microfluidic Platform to design Multimodal PEG - crosslinked Hyaluronic Acid Nanoparticles (PEG-cHANPs) for diagnostic applications. *Sci. Rep.* **2020**, *10*, 6028.
28. Ding, S.; Anton, N.; Vandamme, T.F.; Serra, C.A. Microfluidic nanoprecipitation systems for preparing pure drug or polymeric drug loaded nanoparticles: an overview. *Expert Opin. Drug Deliv.* **2016**, *13*, 1447-1460.
29. Ali, H.; Blagden, L.; York, P.; Amani, A.; Brook, T. Artificial neural networks modelling the prednisolone nanoprecipitation in microfluidic reactors. *Eur. J. Pharm. Sci* . **2009**, *37*, 514-522.
30. Damiati, S.A.; Rossi, D.; Joensson, H.N.; Damiati, S. Artificial intelligence application for rapid fabrication of size-tunable PLGA microparticles in microfluidics. *Sci. Rep.* **2020**, *10*, 19517.
31. Ponsiglione, A.M.; Russo, M.; Netti, P.A.; Torino, E. Impact of biopolymer matrices on relaxometric properties of contrast agents. *Interface Focus* **2016**, *6*, 20160061.
32. Amani, A.; York, P.; Chrystyn, H.; Clark, B.J.; Do, D.Q. Determination of factors controlling the particle size in nanoemulsions using Artificial Neural Networks. *Eur. J. Pharm. Sci.* **2008**, *35*, 42-51.

33. Solomon, I. Relaxation Processes in a System of Two Spins. *Phys. Rev.* **1955**, *99*, 559-565.
34. Smeraldo, A.; Netti, P.A.; Torino, E. New Strategies in the Design of Paramagnetic CAs. *Contrast Media Mol. Imaging* **2020**, *2020*, 4327479.
35. Ponsiglione, A.M.; Russo, M.; Torino, E. Glycosaminoglycans and Contrast Agents: The Role of Hyaluronic Acid as MRI Contrast Enhancer. *Biomolecules* **2020**, *10*.
36. Russo, M.; Ponsiglione, A.M.; Forte, E.; Netti, P.A.; Torino, E. Hydrodenticity to enhance relaxivity of gadolinium-DTPA within crosslinked hyaluronic acid nanoparticles. *Nanomedicine (Lond.)* **2017**, *12*, 2199-2210.
37. De Sarno, F.; Ponsiglione, A.M.; Grimaldi, A.M.; Netti, P.A.; Torino, E. Effect of crosslinking agent to design nanostructured hyaluronic acid-based hydrogels with improved relaxometric properties. *Carbohydr. Polym* . **2019**, *222*, 114991.

MAIN CONCLUSION AND FUTURE PERSPECTIVE

In the present work, different polymer - contrast agent systems in a nanostructured form have been analyzed to understand how the physicochemical properties of the polymer matrix can impact on the imaging ability. In fact, an optimal design of the nanovector allows to reach the specific target and obtain information and/or treat diseases with cellular and molecular precision overcoming the main limitations of clinically used contrast agents. In particular, the control of nanovector properties such as size, shape and charge, together with the encapsulation efficiency and loading degree of drugs and/or imaging agents lead to improve the nano-biointeractions enhancing the diagnostic and therapeutic performances. To achieve this goal, microfluidics has been chosen as a tool to finely tune morphological, structural and functional properties of the nanovectors in a controllable and reproducible manner.

In the Chapter I, a microfluidic hydrodynamic flow focusing approach to produce nanoparticles by ionotropic gelation of chitosan and sodium tripolyphosphate, followed by complex coacervation between chitosan and hyaluronic acid has been presented. The proposed microfluidic approach allows to modulate the size of nanoparticles and their morphologies and structures by varying process parameters. In fact, the variation of the involved parameters (flow rates, polymer concentrations, polymer weight ratio and crosslinking degree) has demonstrated to influence the ionotropic gelation reaction resulting in the formation of several architectures such as coprecipitates or different core-shell nanostructures. In particular, the distinction between the *High* and *Low flow rate regime* has highlighted the influence of the τ_{mix} on the formation of the nanoarchitectures. In fact, low flow rates allow the formation of the core-shell nanostructure and, through a fine handling of the CS:HA weight ratio, the change in the core and shell dimensions. Compared to batch processing, the implemented microfluidic process has required lower polymer concentrations leading to control and optimize the interaction among the chosen compounds at molecular level. This fine control over the nanoarchitecture has also proven to affect the functional properties of the nanocarrier. In fact, it also be possible to take advantage of the properties of the hydrogel matrix to obtain a relaxivity boost of the encapsulated gadolinium-based contrast agent for Magnetic Resonance Imaging as explained by the *Hydrodenticity* concept. In detail, the presence of the hydrophilic polymer matrix affects the water molecular dynamic and influences the characteristic correlation times of the Solomon-Bloembergen-Morgan (SBM) theory leading to the enhancement of the relaxivity of the Gd-DTPA. In addition, the opportunity to tune the nanoparticles architecture

by changing microfluidic parameters and, consequently, the chitosan - hyaluronic acid ratio, allows the control of the gadolinium-based contrast agent hydration and the modulation of its relaxometric properties. In particular, the presence of the double polymer network crosslinked by TPP leads to an increment of the water molecules lifetime (τ_M) and a reduction of both rotational τ_R and translational diffusional τ_D correlation times. According to the SBM and Hwang and Freed theories for the inner and outer spheres, respectively, the result is an enhancement of the total relaxivity. Finally, the simultaneous encapsulation of ATTO488 dye for Optical Imaging has highlighted the possibility to use this nanocarrier as a promising multimodal imaging probe.

In the Chapter II, a nanoprecipitation process for the production of PLGA-based contrast agent for Computed Tomography Angiography (CTA) has been developed. Here too, a microfluidic hydrodynamic flow focusing has been used to take advantage of the tunability of the process parameters that this technique offers. In fact, this method has demonstrated to be highly efficient in terms of throughput and nanoparticles' size homogeneity. The mixing of PLGA and water within the microfluidic channels causes a fast nanoprecipitation phenomenon leading to the formation of a remarkable number of NPs. The influence of flow rates and polymer concentration on the nanoprecipitation process has been deeply studied to find the optimal condition for the production of these nanovectors. In particular, the τ_{mix} is extremely important in the determination of NPs size: the shorter the mixing time, the smaller the particles. The explanation lays in the diffusion process within the microfluidic channels. In fact, a small τ_{mix} means that extraction of solvent and its diffusion into non-solvent phase is faster, determining the formation of small nanoparticles that are kinetically locked and more homogeneous in size since the mixing occurs faster than the aggregation phenomenon ($\tau_{mix} < \tau_{agg}$). By changing the flow rate conditions, the hydrodynamic flow focusing width can be modulated consequently affecting the diffusional path of solvent molecules toward the non-solvent phase. In fact, moving to higher side flow rate values, the flow focusing becomes narrower, the diffusional path decreases and a shorter τ_{mix} is reached, resulting in smaller NPs. An additional proof is represented by the introduction of the small amount of water in the solvent composition before the introduction of Iodixanol in the process. In fact, the co-solvent improves the affinity with the non-solvent phase affecting the diffusivity parameter of the τ_{mix}. The result is a faster mixing that leads, comparing the same flow rates conditions, to smaller NPs. Moreover, from the fluidodynamic point of view, the polymer concentration is another parameter influencing the final NPs size. In fact, the slightly higher viscosity of the polymer solution affects the τ_{mix} and consequently promotes the formation of bigger nuclei. Obviously, the local polymer concentration

is dependent on the flow rate conditions confirming the strong versatility of the microfluidic platform in modulating the nanoprecipitation process and, consequently, the NPs size. In addition, different contrast agents have been encapsulated within the polymer matrix to confirm the PLGA well-known encapsulation efficiency and loading capability and study the influence of the polymer matrix on the imaging signal. Firstly, ATTO633 dye, suitable for Optical Imaging, has been encapsulated alone or in combination with Gd-DTPA showing a negative influence on the imaging signal. In fact, despite the high encapsulation efficiency for both contrast agents, the polymer matrix has revealed to reduce the fluorescence signal while in the case of Gd-DTPA longitudinal relaxation rate, the *Hydrodenticity* has not been observed probably due to the prevalent hydrophobic nature of the PLGA. Successively, the widely used CTA contrast agent Iodixanol, sold with the trade name of VISIPAQUE, has been successfully encapsulated in clinically relevant amount within nanoparticles. In particular, even in this case, the polymer matrix seems to partially reduce the attenuation power of Iodixanol compared to the free contrast agent, result confirmed by the in vitro analysis performed on the empty nanocarrier. Moreover, preliminary data on the cytotoxicity and rheological *in vitro* behaviour of the loaded-nanocarrier, together with a first attempt of a micellization process of a PLGA-PEG copolymer to confer to the nanovector long circulation properties, have been presented. In the last Chapter, machine learning has been proposed as method to explore multivariate processes where there is no linear relation between the operational parameters and the final outcome. In particular, Artificial Neural Networks (ANNs) has been used to analyze the influence of process parameters on the nanoparticles and microparticles' size as result of a microfluidic production. In fact, despite the several advantages offered by microfluidics to finely tune and precisely control particles morphological, structural, and functional properties, the number of involved variables increases. Initially, ANN models have been built up for the two processes described in the previous Chapters starting from the data collected during the experimental campaign. The trained networks have allowed us to quantify the influence of polymer concentrations and microfluidic flow rates on the nanoparticles size and predict the trend of this latter for no explored process parameters conditions. However, in particular in the case of chitosan-hyaluronic acid nanoparticles, the correlation coefficient has brought to light a lack in the variability of process parameters and relative experimentally obtained size that affects the predictability of the neural network. Successively, a different ANN has been used to classify the dripping regimes obtained during the droplet generation of hyaluronic acid microparticles of two different polymer molecular weights. The model has highlighted the presence of not well observed regimes in particular at high flow rates of the

polymer flow rates due to deposition in the microfluidic channels that have altered the correct fluidodynamics. Finally, a regression analysis has been also performed on data taken from a previous published work of our group regarding the influence of a hyaluronic acid matrix, crosslinked by DVS reaction, on the longitudinal relaxation rate of Gd-DTPA in a bulk system. Results obtained about the influence of input parameters on the outcome has demonstrated to find a clear explanation through the Solomon-Bloembergen-Morgan theory and the *Hydrodenticity* concept.

In summary, the interaction between clinically used contrast agents and polymer nanostructures has been studied with the aim to take advantage of the physicochemical properties of this latter to obtain an improvement of the performances of contrast agents. In fact, it has been noted that the choice of the suitable polymer is essential to obtain the desired effect on the imaging ability of the contrast agent. For example, comparing the simultaneous encapsulation of Gd-DTPA and a dye for both CS-HA and PLGA nanosystems, a different behaviour has been observed for the MRI contrast agent. In particular, the PLGA allows to reach a remarkable encapsulation efficiency while the hydrophilic property of CS and HA plays a key role in the enhancement of the longitudinal relaxivity acting on the characteristic correlation times. In this way, despite a different Gd-DTPA loaded amount has been loaded within the two nanosystems, they show comparable results in terms of relaxation times. In addition, the tunability of the morphological and structural properties of the nanoparticles offers a further advantage. In particular, microfluidics has been demonstrated, in both cases, to be the optimal choice to finely handle the physicochemical features of the nanovectors. Indeed, thanks to the modulation of process parameters, it has been possible to control the interaction between compounds, affecting the τ_{mix} at the chip junction and, consequently, the nanoparticles formation phenomena at molecular level. The tuning of the morphological and structural features of the nanovector allows to influence and modulate the fundamental parameters that are at the base of the imaging signal generation leading to an enhancement of the contrast ability without chemically modify the contrast agent itself. As support to the performed experimental campaigns, the used machine learning approach has allowed us to get important information about the influence of process parameters on the final outcome in order to understand how rightly modulate the operational conditions and quickly achieve the optimal design of the nanovector avoiding time and material waste.

In conclusion, the present work has demonstrated the possibility to tune the performances of clinically used contrast agents without involving any chemical modifications but simply acting on

the physicochemical properties of a polymer nanovector. In addition, the presence of the surrounding polymer matrix could be used to decorate its surface with ligands of different type to overcome several biological barriers and reach the molecular target to obtain functional and morphological information. In fact, as demonstrated for both nanocarriers, these nanovectors could also pave the wave for the development of new probes as support to multimodal imaging techniques such as PET/CT or PET/MRI that actually require the administration of a contrast agent for each diagnostic modality. However, to finely tune the physicochemical properties of the nanovectors and obtain the desired imaging boost, I believe that an in-depth study of the interaction mechanisms between several polymer and imaging agents at molecular level has to be faced. In fact, only through a better comprehension of the thermodynamic phenomena that arising from the interplay of contrast agents and polymer chains, it could be possible to handle the functional properties of the nanovectors. The developed microfluidic approach represents the perfect strategy to explore and tune the morphological and structural properties of the polymer nanovectors when one or more contrast agents are encapsulated thanks to its high efficiency and scalability. Starting from the study of bulk systems and then moving towards nanostructured ones, I suppose that some parameters may be found to build one or more mathematical expression able to predict the imaging ability of the nanovector. Obviously, this requires a wide experimental campaign involving as many polymers and contrast agents as possible trying to generalize the relation. From this point of view, the use of machine learning could help to accelerate the process allowing to reduce the number of required trials and extract hidden and nonlinear relation between the specific contrast agent and the polymer network features. Moreover, a further step could be also addressed to the study of the interactions in a biological environment since this latter influence the imaging ability of the contrast agent and the fate of the nanovector.

APPENDIX

A. CHAPTER 1 SUPPLEMENTARY MATERIAL

Identification of the optimal flow rate ratio condition

The best conditions of the flow rate ratio have been selected as those allowing reproducibility of the results, high nanoparticles throughput and stability of the flow focusing. In the following Figure I-S1, representative images of the different conditions tested are shown.

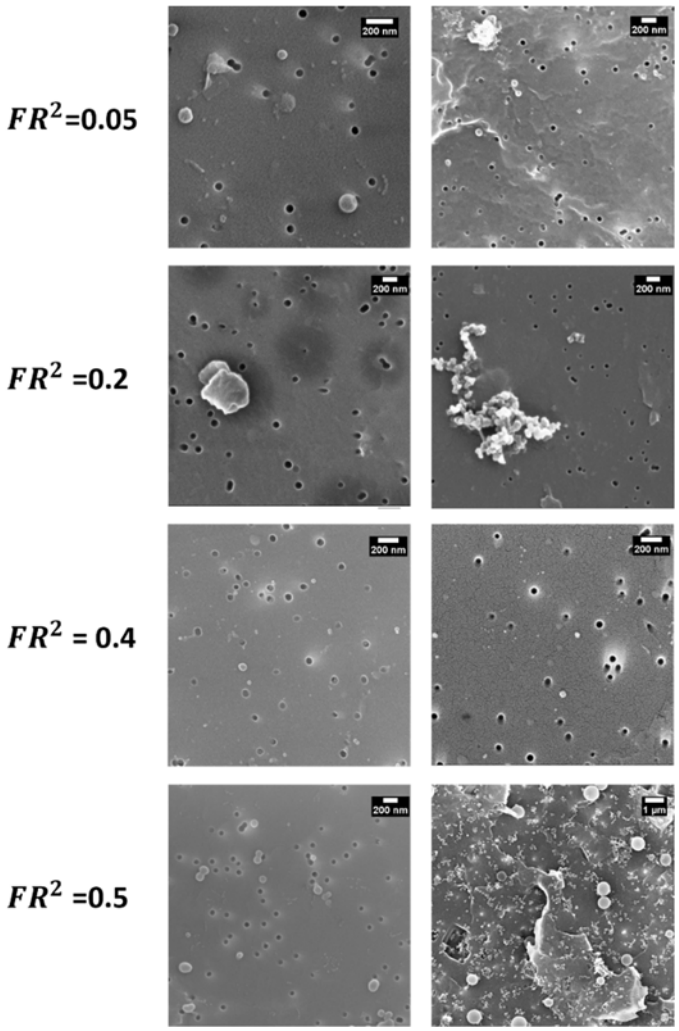

Figure I-S1. Representative SEM images of flow rate ratio conditions tested.

As from Figure I-S1, FR^2 = 0.5 is selected as the optimal condition leading to numerous and reproducible nanoparticles.

Effect of the concentration of the polymers at $FR^2 = 0.5$ and constant polymer ratio

Experiment carried out at CS=0.2 %w/v , CS:HA=6.25 and FR^2=0.5 is showed in the following figure.

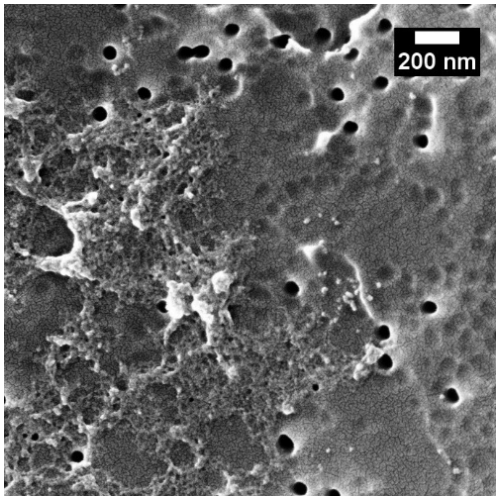

Figure I-S2. Representative SEM image of CS 0.2 %w/v at CS:HA=6.25 and $FR^2 = 0.5$.

Macroaggregates and unreacted materials are obtained in this case instead of nanoparticles, therefore the size was not measurable.

Effect of the polymer ratio at $FR^2 = 0.5$

The following figure displays SEM images related to different CS:HA ratios at *High* and *Low flow rate regimes* at constant $FR^2 = 0.5$.

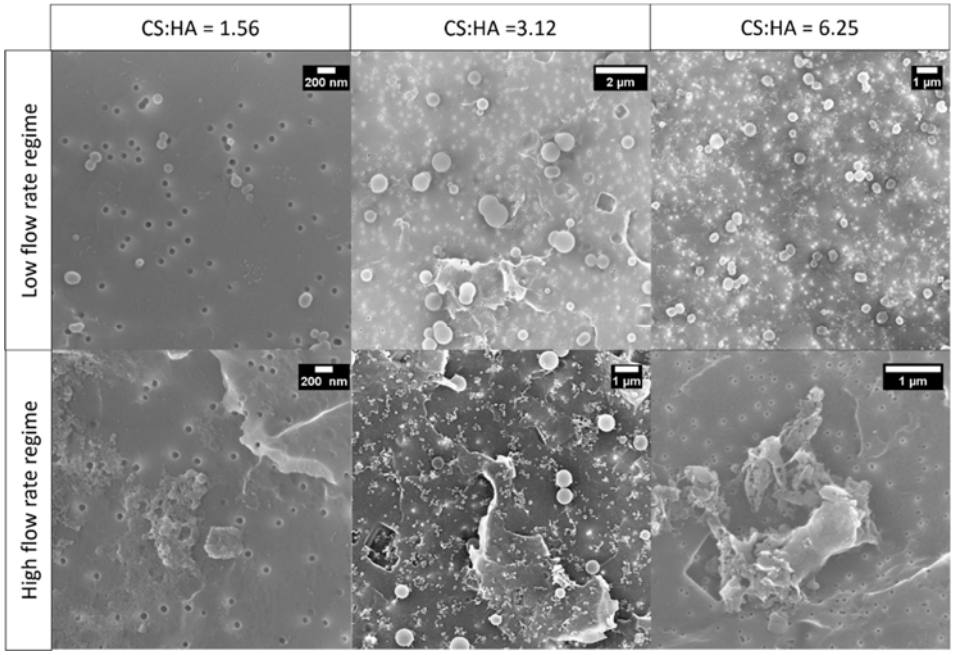

Figure I-S3. Representative SEM images of different CS:HA ratios at $FR^2 = 0.5$.

All the conditions have proved to be suitable to produce NPs except for the conditions related to the lower right SEM image where no NPs are obtained.

Effect of Flow rate ratio at TPP = 0.003% and 0.012%

To understand the influence of the crosslinker, two TPP concentrations (0.003 and 0.012 % w/v) have been compared keeping fixed the concentrations of the two polymers (HA = 0.002 % w/v and CS = 0.00625 % w/v). The size of the obtained NPs has been plotted (Figure I-S4a) as a function of the flow rate ratio (from 0.05 to 0.4) and corresponding representative SEM images have been provided (Figure I-S4b)

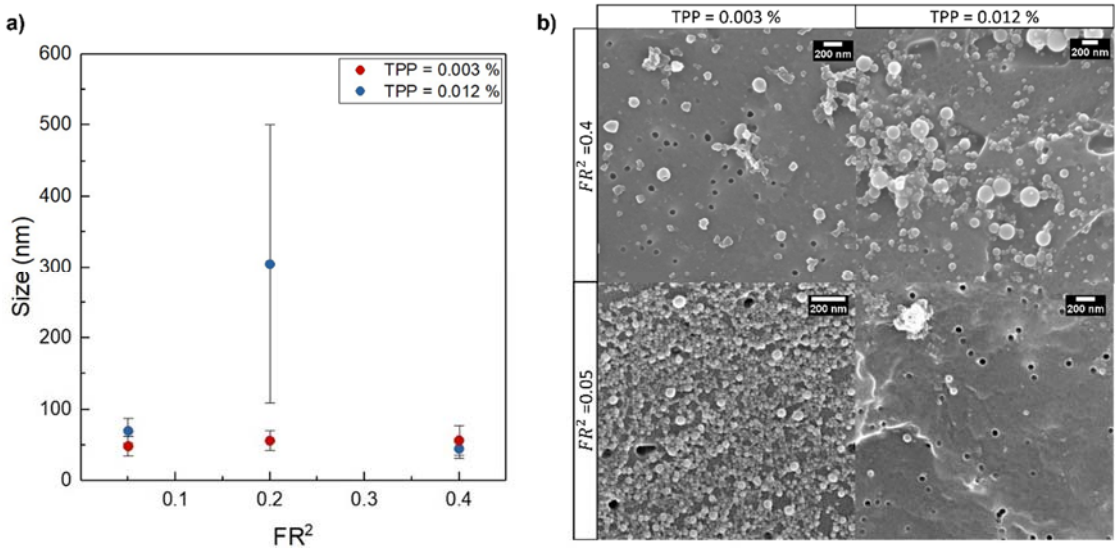

Figure I-S4. (a) NPs size as a function of FR^2 (0.05, 0.2 and 0.4) at two TPP concentration (0.012 or 0.003% w/v); **(b)** SEM images of NPs at two TPP concentrations and two different flow rates.

Figure I-S4a shows that TPP concentration interferes in coprecipitation process. At TPP = 0.003%, size and polydispersity are very similar regardless the flow rate ratio. On the contrary, at TPP = 0.012% and FR^2 = 0.2, NPs are more polydisperse, while, at FR^2 = 0.4 and 0.05, they lead to coprecipitates with size and polydispersity comparable to the one obtained at TPP = 0.003%. SEM images in Figure I-S4b confirm that morphologies are influenced by the flow rates, with size and polydispersity growing proportionally with FR^2 and TPP.

Operational Regimes and obtained morphologies

Representative architectures at different FR^2 and CS/HA polymer ratio.

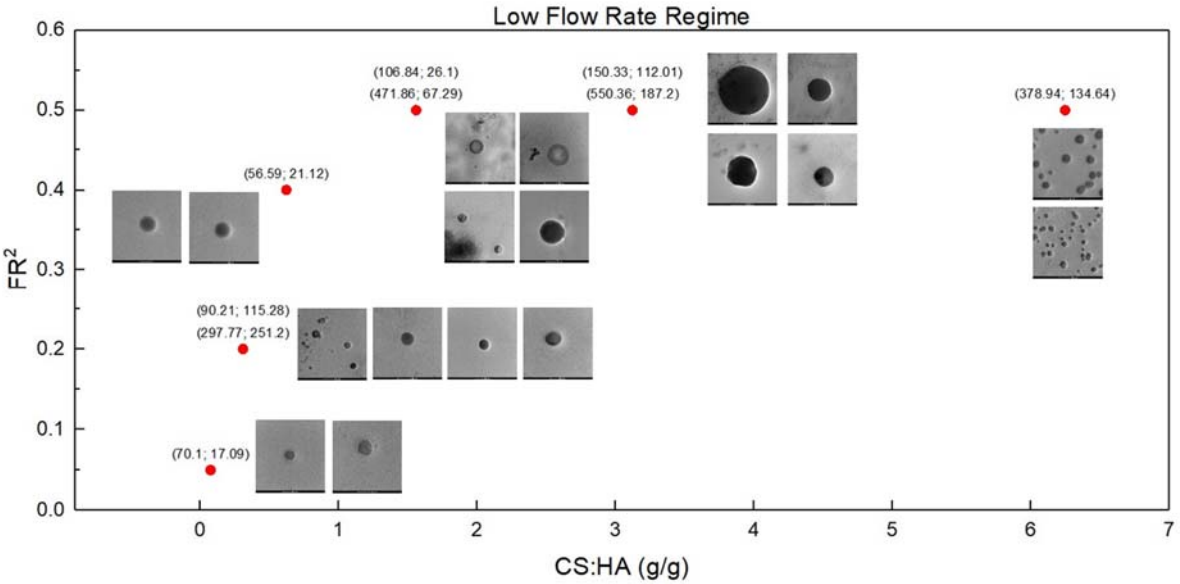

Figure I-S5. Visual plot displaying morphology of NPs at *Low flow rate regime* as a function of FR^2 and CS:HA ratio. Average diameter and its standard deviation are given in brackets for each trial displayed.

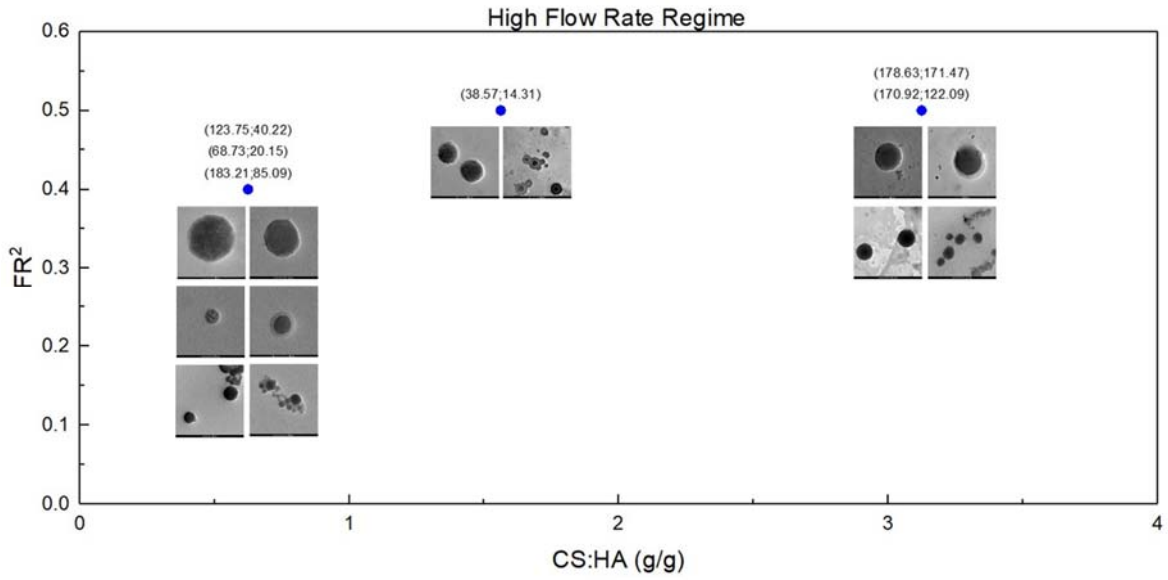

Figure I-S6. Visual plot displaying morphology of NPs at *High flow rate regime* as a function of FR^2 and CS:HA ratio. Average diameter and its standard deviation are given in brackets for each trial displayed.

B. CHAPTER 2 SUPPLEMENTARY MATERIAL

Effect of flow rates and polymer concentration on PLGA nanoprecipitation process

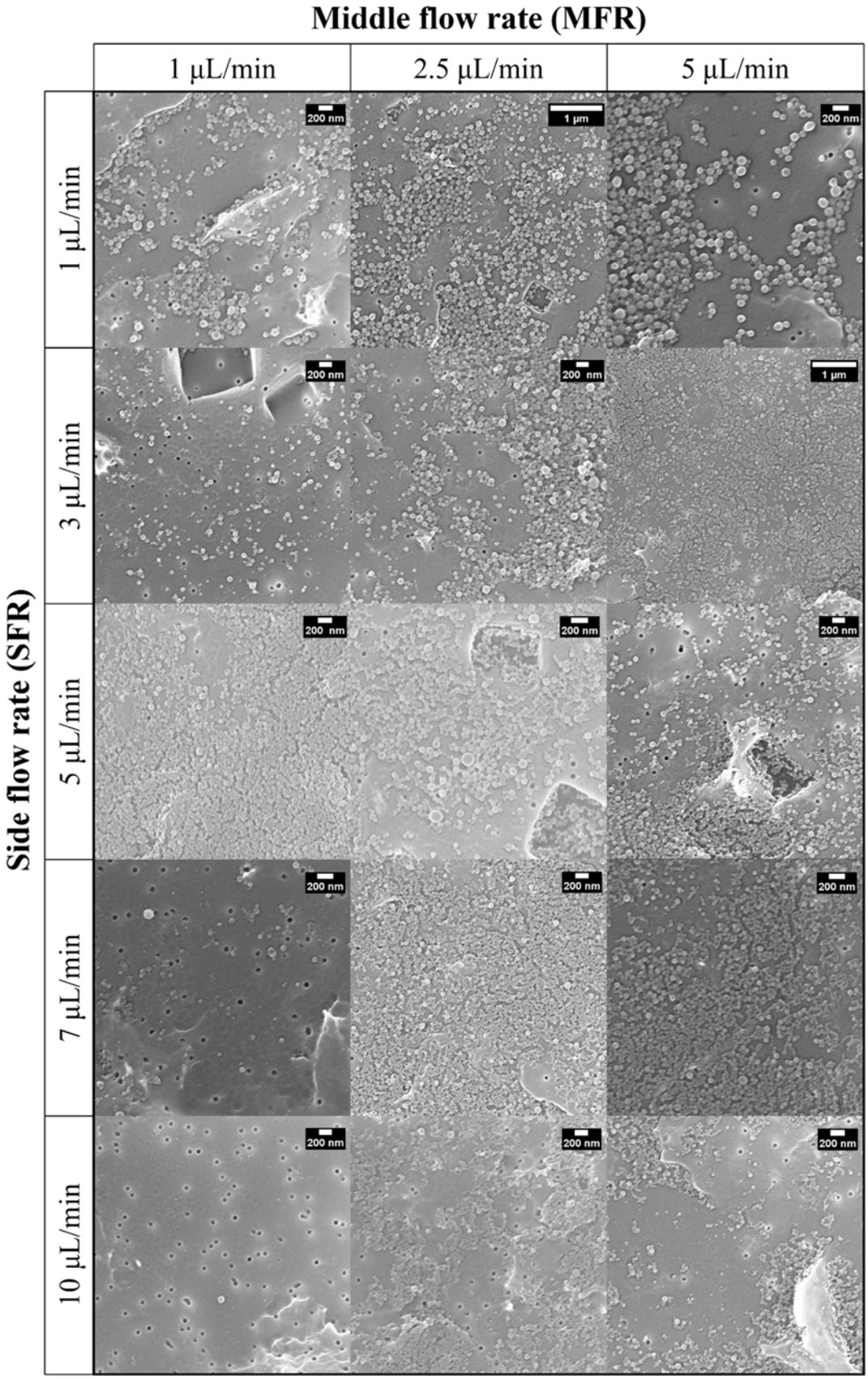

Figure II-S1. SEM representative images of each tested SFR-MFR combination at [PLGA] = 1 mg/mL.

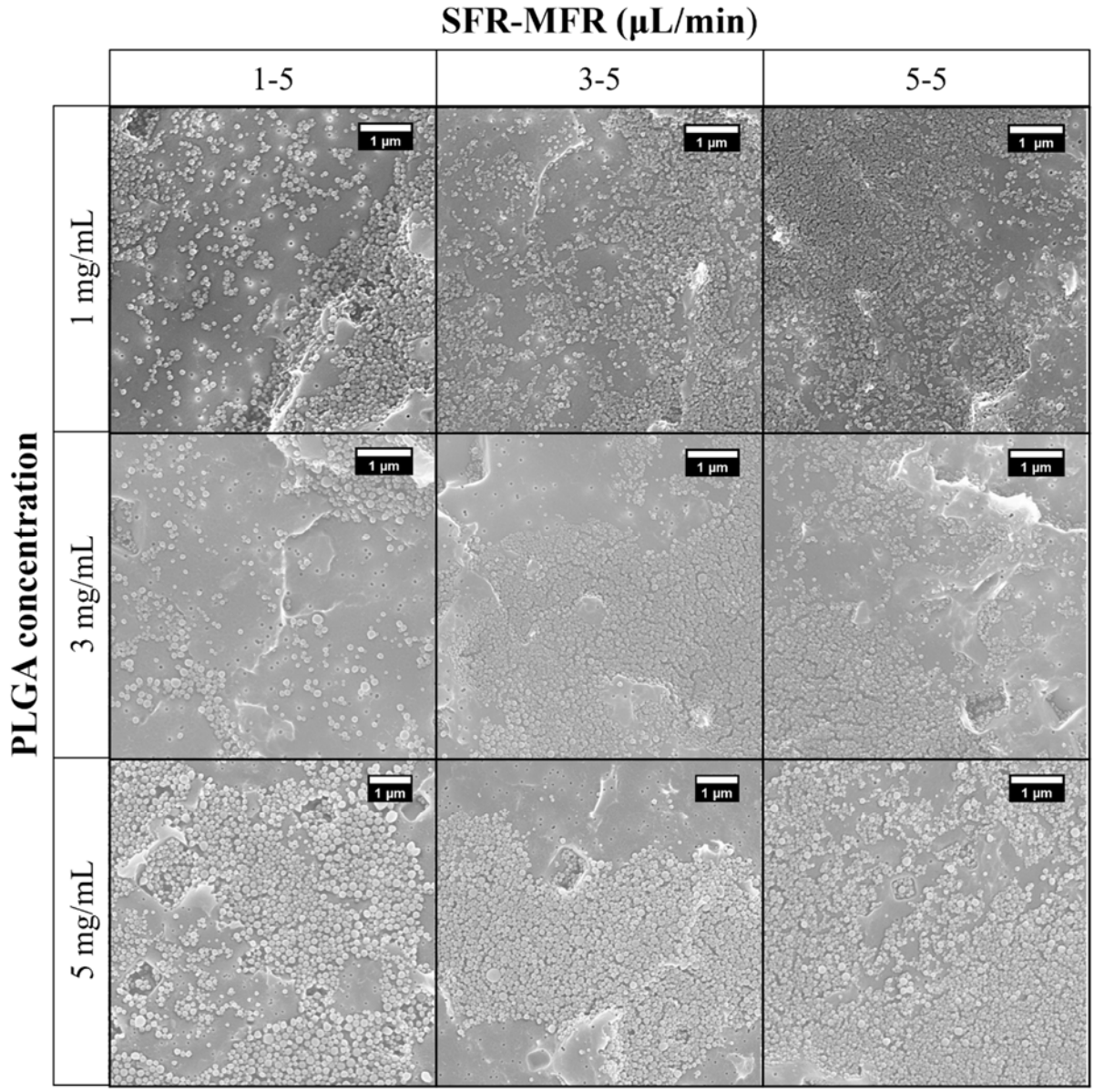

Figure II-S2. Representative SEM images for the three optimal conditions identified at [PLGA]= 1 mg/mL and replicated for higher polymer concentrations, 3 and 5 mg/mL.

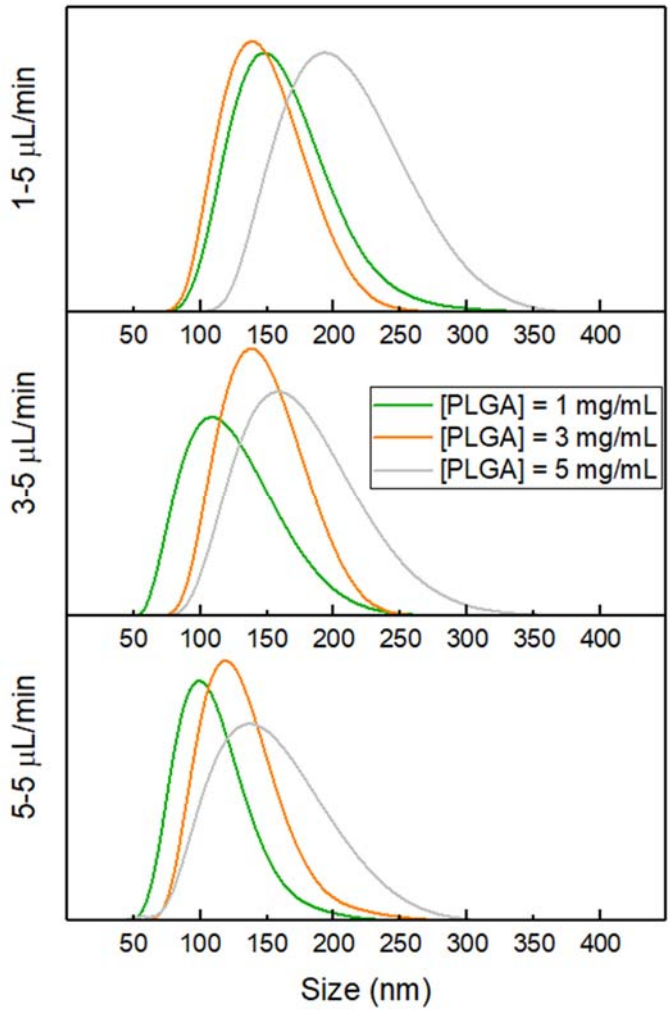

Figure II-S3. NPs size distribution curves obtained by DLS measurements for the three optimal SFR-MFR process conditions carried out at three different PLGA concentration.

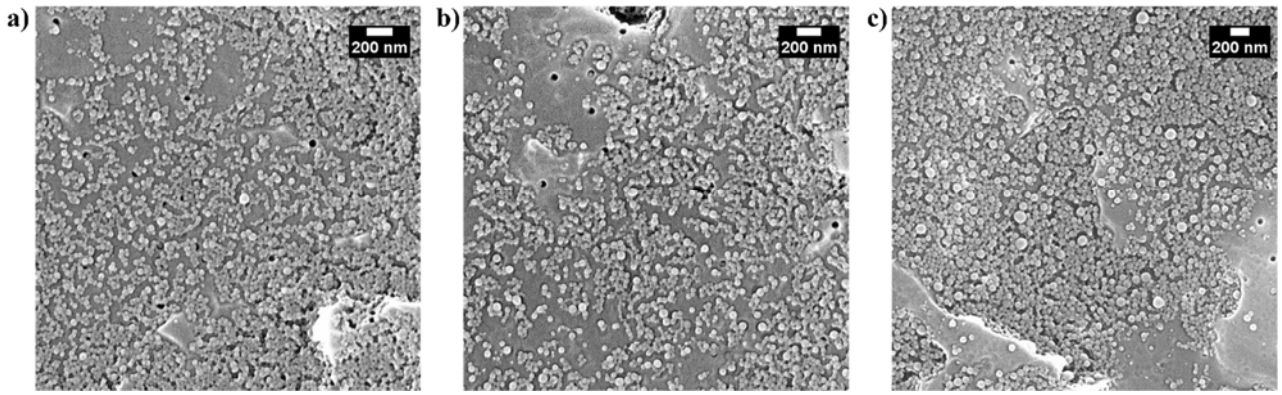

Figure II-S4. SEM representative image of Iodixanol-loaded NPs at the three optimal flow rate conditions: **(a)** 5-5 µL/min; **(b)** 3-5 µL/min; **(c)** 1-5 µL/min.

Effect of iodine concentration on cells metabolic activity

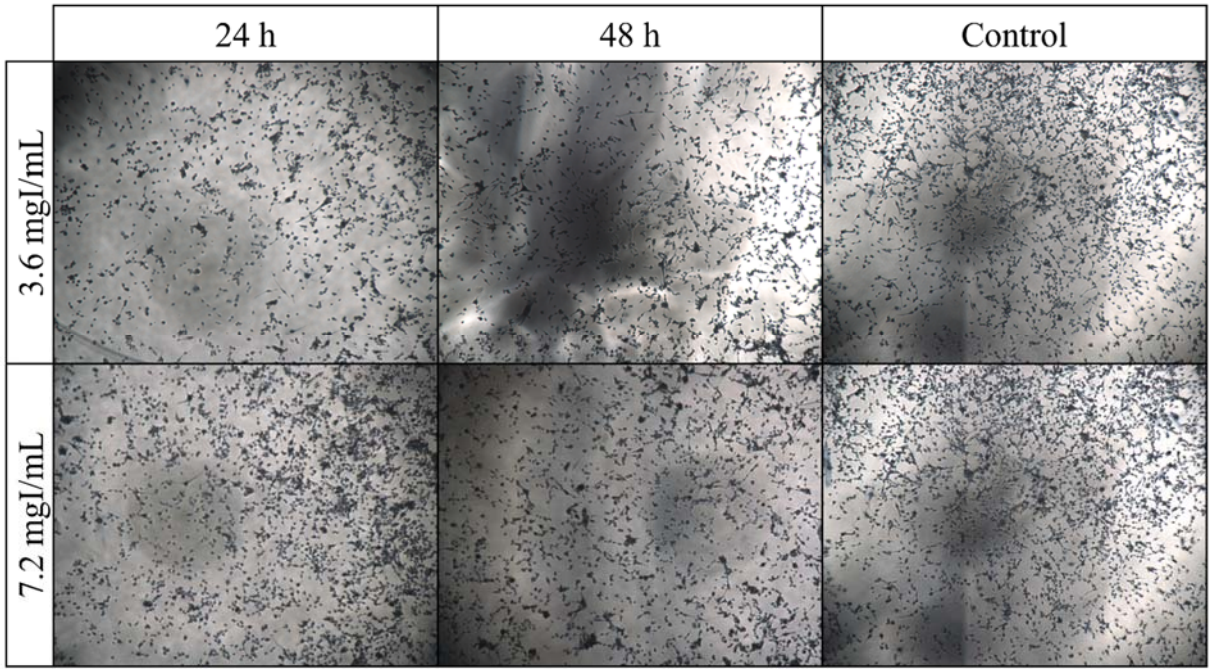

Figure II-S5. Microscope images of cells put in contact with two different Iodixanol-loaded NPs concentrations at 24 and 48h taking in consideration the iodine content.

C. CHAPTER 3 SUPPLEMENTARY MATERIAL

Table III-S1. Experimental and predicted size data in training, test, and validation subset for PLGA NPs.

Experimental PLGA NPs size (nm)	Predicted PLGA NPs size (nm)	Error (nm)
Training data		
132	132.4083	-0.40828
129.4	130.4638	-1.0638
137.9	116.2921	21.60789
96.2	116.2921	-20.0921
105.1	107.7716	-2.67158
113.6	107.7716	5.828423
92.43	86.0245	6.405499
81.48	89.63775	-8.15775
90.31	91.98817	-1.67817
128	127.9849	0.015148
74	71.72674	2.273258
81	87.63342	-6.63342
136	139.2777	-3.27766
135	128.9081	6.091873
157	154.2642	2.735828
133	136.4615	-3.46154
113.2	117.7725	-4.57248
105.1	107.7716	-2.67158
114.8	104.841	9.958976
99.99	99.76157	0.228431
Test data		
145.7	132.4083	13.29172
120	114.6103	5.389738
148	125.1517	22.84833
104	109.4754	-5.47537
108.9	112.3989	-3.49895
Validation data		
160.3	130.4638	29.8362
116.9	113.6086	3.291375
80.77	86.89906	-6.12906
124	119.6255	4.374537
114.4	114.7253	-0.32527

Table III-S2. Experimental and predicted size data in training, test, and validation subset for CS-HA NPs.

Experimental CS-HA NPs size (nm)	Predicted CS-HA NPs size (nm)	Error (nm)
Training data		
109.3552	162.6477	-53.2926
103.4298	162.6477	-59.2179
143.6529	162.6477	-18.9948
338.7194	162.6477	176.0717
48.62738	119.4828	-70.8554
198.8089	119.4828	79.32608
87.20773	119.4828	-32.275
99.28705	119.4828	-20.1957
152.7837	119.4828	33.3009
228.2035	162.6477	65.55576
235.2309	162.6477	72.58312
56.21853	162.6477	-106.429
187.4289	119.0948	68.33411
70.1	59.16127	10.93873
44.95	118.5357	-73.5857
56.59	119.0948	-62.5048
90.21	162.6477	-72.4377
183.21	118.5357	64.67426
471.8588	465.7601	6.09863
106.8366	98.91078	7.925786
170.9188	181.5029	-10.5841
Test data		
191.1187	157.7094	33.40927
45.87	118.5357	-72.6657
123.75	119.0948	4.655232
68.73385	118.5357	-49.8019
157.8832	130.7818	27.10141
Validation data		
138.0404	162.6477	-24.6073
53.99061	131.7375	-77.7469
38.5681	98.91078	-60.3427
178.6345	181.5029	-2.86832
150.3314	181.5029	-31.1714

Table III-S3. Experimental and predicted relaxation rate in training, test, and validation subset for DVS-crosslinked HA Hydrogel.

Experimental Relaxation Rate (s^{-1})	Predicted Relaxation Rate (s^{-1})	Error (s^{-1})	Experimental Relaxation Rate (s^{-1})	Predicted Relaxation Rate (s^{-1})	Error (s^{-1})	Experimental Relaxation Rate (s^{-1})	Predicted Relaxation Rate (s^{-1})	Error (s^{-1})
Training data								
0.88	0.886791	-0.00679	0.265	0.301747	-0.03675	0.3165	0.322562	-0.00606
0.264	0.306105	-0.04211	0.309	0.324844	-0.01584	0.32375	0.326565	-0.00282
0.372	0.374631	-0.00263	0.345	0.34808	-0.00308	0.33825	0.334269	0.003981
0.434	0.429339	0.004661	0.373	0.371427	0.001573	0.35275	0.341731	0.011019
0.463	0.459452	0.003548	0.398	0.394964	0.003036	0.465	0.454892	0.010108
0.496	0.491191	0.004809	0.445	0.418835	0.026165	0.4725	0.462575	0.009925
0.588	0.592288	-0.00429	0.548	0.494147	0.053853	0.48	0.469598	0.010402
0.685	0.692261	-0.00726	0.594	0.548826	0.045174	0.495	0.482142	0.012858
0.754	0.754374	-0.00037	0.755	0.703814	0.051186	0.5025	0.487849	0.014651
0.909	0.896036	0.012964	1.071	1.043905	0.027095	0.51	0.493277	0.016723
0.342	0.369471	-0.02747	0.301	0.337801	-0.0368	0.525	0.503511	0.021489
0.348	0.397363	-0.04936	0.313	0.361944	-0.04894	0.5325	0.508399	0.024101
0.381	0.427553	-0.04655	0.342	0.386347	-0.04435	0.9525	0.968255	-0.01576
0.449	0.46013	-0.01113	0.403	0.411134	-0.00813	0.97675	0.994693	-0.01794
0.436	0.495101	-0.0591	0.549	0.489668	0.059332	1.001	1.018384	-0.01738
0.599	0.612431	-0.01343	0.547	0.547344	-0.00034	1.02525	1.039465	-0.01421
0.702	0.696649	0.005351	0.595	0.610526	-0.01553	1.0495	1.058148	-0.00865
0.722	0.821477	-0.09948	0.699	0.716568	-0.01757	1.07375	1.074687	-0.00094
0.805	0.899707	-0.09471	0.786	0.7946	-0.0086	1.098	1.089353	0.008647
0.315	0.318873	-0.00387	1.043	0.920957	0.122043	1.12225	1.102408	0.019842
0.339	0.346187	-0.00719	1.126	1.235289	-0.10929	1.1465	1.114101	0.032399
0.384	0.375238	0.008762	0.6355	0.642839	-0.00734	0.89612	0.888106	0.008014
0.392	0.390294	0.001706	0.65925	0.664145	-0.0049	0.91884	0.904666	0.014174
0.4	0.405631	-0.00563	0.683	0.683064	-6.40E-05	0.94156	0.898356	0.043204
0.45	0.43693	0.01307	0.70675	0.699848	0.006902	0.46312	0.449315	0.013805
0.505	0.500745	0.004255	0.7305	0.714768	0.015732	0.47964	0.467131	0.012509
0.503	0.532766	-0.02977	0.75425	0.728086	0.026164	0.36642	0.323439	0.042981
0.599	0.596585	0.002415	0.80175	0.750878	0.050872	0.36864	0.320414	0.048226
0.757	0.755026	0.001974	0.8255	0.760768	0.064732	0.37308	0.304146	0.068934
0.904	0.907204	-0.0032	0.84925	0.769887	0.079363	0.37752	0.304105	0.073415
0.331	0.330458	0.000542	1.0128	1.008157	0.004643	0.33537	0.3217	0.01367
0.382	0.423844	-0.04184	1.082	1.076507	0.005493	0.34422	0.301561	0.042659
0.445	0.458089	-0.01309	1.1512	1.134942	0.016258	0.30338	0.319969	-0.01659
0.51	0.493277	0.016723	1.1858	1.160004	0.025796	0.30506	0.316596	-0.01154
0.485	0.529146	-0.04415	1.2204	1.182364	0.038036	0.30842	0.299635	0.008785
0.59	0.677942	-0.08794	1.2896	1.219758	0.069842			
0.797	0.8786	-0.0816	0.30925	0.318415	-0.00916			
Test data								
0.528	0.463498	0.064502	1.098	1.089353	0.008647	0.4875	0.476086	0.011414
0.309	0.327263	-0.01826	0.675	0.638817	0.036183	0.5175	0.498483	0.019017
0.347	0.350067	-0.00307	0.468	0.462598	0.005402	1.17075	1.124652	0.046098
0.351	0.412164	-0.06116	0.9782	0.971361	0.006839	0.88476	0.885069	-0.00031
0.493	0.468737	0.024263	1.1166	1.107094	0.009506	0.45486	0.436056	0.018804
0.301	0.359656	-0.05866	1.255	1.202203	0.052797	0.33714	0.3185	0.01864
0.36	0.390902	-0.0309	0.302	0.314079	-0.01208	0.34068	0.30188	0.0388
0.61	0.602455	0.007545	0.3455	0.338021	0.007479			
Validation data								
0.485	0.440536	0.044464	0.273	0.293585	-0.02059	0.778	0.740048	0.037952
0.388	0.387603	0.000397	0.678	0.691865	-0.01386	1.0474	1.043396	0.004004
0.398	0.401045	-0.00304	0.701	0.796279	-0.09528	0.2875	0.304617	-0.01712
0.562	0.524224	0.037776	0.452	0.443212	0.008788	0.29475	0.309502	-0.01475
0.273	0.34374	-0.07074	0.845	0.806638	0.038362	0.331	0.330458	0.000542
0.51	0.532348	-0.02235	0.971	0.876669	0.094331	0.49616	0.460387	0.035773
0.512	0.571599	-0.0596	0.402	0.436485	-0.03448	0.31178	0.29903	0.01275
1.075	1.070077	0.004923	0.896	1.009682	-0.11368			

Publications Along Three Years

- Smeraldo A., Netti P.A., Torino E., "New Strategies in the Design of Paramagnetic CAs. *Contrast Media Mol Imaging"* **2020**, *2020*, 4327479. doi:10.1155/2020/4327479
- Smeraldo A., Ponsiglione A.M., Netti P.A., Torino E., "Tuning of Hydrogel Architectures by Ionotropic Gelation in Microfluidics: Beyond Batch Processing to Multimodal Diagnostics. *Biomedicines"* **2021**, *9*, 1551. doi: 10.3390/biomedicines9111551
- Smeraldo A., Ponsiglione A.M., Russo M., Netti P.A., Torino E., "Artificial Neural Networks (ANN) to impact on the design of nanostructures obtained through microfluidics" – *Under preparation*
- Smeraldo A., Ponsiglione A.M., Bevilacqua P., Netti P.A., Torino E., "A systematic review on advances in brain PET-MRI diagnostics" – *Under preparation*
- Smeraldo A., Bortone O., Netti P.A., Torino E., "A new microfluidic approach to design iodinated-PLGA nanosystems"- *Under preparation*

Collaborations

- Institute of Clinical Physiology (CNR-IFC) and University Hospital of Pisa

Phd Schools and Programs

- Training School "NMR relaxometry data analysis: theory and software", Department of Physics, University of Pavia from 18/02/2019 - 22/02/2019 (*Awarded grant*)

Aim of the school: Discussion about the state of the art of current software to use for data elaboration and analysis and possibilities to improve the available software. The training school included some teaching and hands-on sessions on use of some relaxometry software and how to apply these to get the most out of relaxometry data.

- Summer School "Innovation in chronic disease intervention" (euVENTION), Marsilius Arkaden, Ruprecht Karl University of Heidelberg, Heidelberg, 21/07/2019 – 02/08/2019 (*Awarded grant*)

Aim of the school: euVENTION's overall goal is to provide graduates, PhD students and young professionals the opportunity to improve prevention and treatment options for people who are at risk or suffer from chronic disease. euVENTION guides you through the whole process of product or service from the theoretical challenge to business development and creating the prototype.

- XL Annual School of Bioengineering: "Biofabrication: an integrated bioengineering approach for the automated fabrication of biological structures for clinical and research applications", 13/09/2021 – 16/09/2021, Aula Magna, Casa della Gioventù universitaria, Università di Padova, Bressanone (*Virtual Attendance*)

Aim of the school: the XL Annual GNB School aims at providing Ph.D students with interdisciplinary knowledge and hand-on-training from experts belonging to the Italian bioengineering community, as well as international scientists and industrial leaders. New knowledge and critical discussion with eminent scientists and industrial leaders will contribute to inspire the new generation of young researchers in committing towards continuous advances in biofabrication technologies.

Communications to Congress and Conferences

Oral presentation at the "Applied Nanotechnology and Nanoscience International Conference 2021" with the article title "Tunable hydrogel nanostructures by microfluidics to control *Hydrodenticity* effect for multimodal imaging applications" held online from 24/03/2021 to 26/03/2021.

Other Activities

HydroBlink is a spin-off project of the CRIB – Interdepartmental Research Center on Biomaterials of the University of Naples "Federico II", and the company LIGI Tecnologie Medicali from Taranto (Italy), specialized in refractive surgery products. The aim is the production of a new microparticles-based collyrium that supports the natural corneal re-epithelialization process and allows a better recovery of vision for patients undergoing refractive and ocular surgery.

European Accelerator Programs

EIT Jumpstarter: Naples, 17-18th May 2019 organized by EIT Health

EIT Slim Project: 4-month course including workshops in Naples, Delft and Madrid

National Accelerator Programs

BioInItaly Investment Forum & Intesa Sanpaolo Start-up Initiative (awarded as best presentation in Naples during the national roadshow)

EnkiMed Enkimed is a spin-off project of the Scuola Medica Ospedaliera della Campania, Azienda Ospedaliera "A. Cardarelli" of Naples and University of Naples "Federico II". The offered product consists in a cannulation device for extracorporeal circulation to achieve antegrade flow in aortic arch and thoraco-abdominal aorta by femoral cannulation to avoid Deep Hypothermic Circulatory Arrest during cardio-pulmonary bypass operations thus reducing the occurrence of possible side effects.

National Accelerator Programs

Start Cup Campania 2021 (awarded with the 3rd place and participation to the following national phase – Premio Nazionale dell'Innovazione (PNI))